

# MICROSTRUCTURAL CONTROLS ON MACRO-SCALE PROPERTIES OF ROCK

by

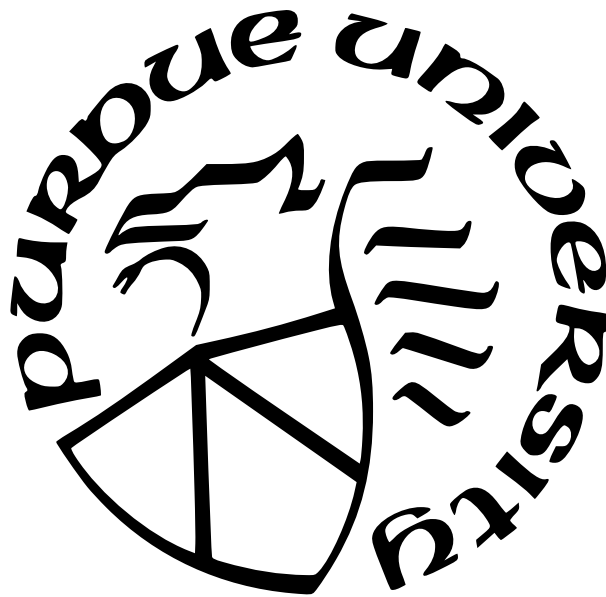
Liyang Jiang

A Dissertation

*Submitted to the Faculty of Purdue University*

*In Partial Fulfillment of the Requirements for the degree of*

Doctor of Philosophy



Department of Physics and Astronomy

West Lafayette, Indiana

May 2022

**THE PURDUE UNIVERSITY GRADUATE SCHOOL  
STATEMENT OF COMMITTEE APPROVAL**

**Dr. Laura J. Pyrak-Nolte, Chair**

Department of Physics and Astronomy

**Dr. Antonio Bobet**

Lyles School of Civil Engineering

**Dr. David D. Nolte**

Department of Physics and Astronomy

**Dr. Douglas Schmitt**

Department of Earth, Atmospheric, and Planetary Sciences

**Dr. Paul F. Muzikar**

Department of Physics and Astronomy

**Approved by:**

Dr. Gabor Csathy



## ACKNOWLEDGMENTS

This material is based upon work performed by graduate students supported by the U.S. Department of Energy, Office of Science, Office of Basic Energy Sciences, Geosciences Research Program under Award Number (DE-FG02-09ER16022). Sandia National Laboratories is a multi-mission laboratory managed and operated by National Technology and Engineering Solutions of Sandia, LLC, a wholly owned subsidiary of Honeywell International, Inc., for the U.S. Department of Energy's National Nuclear Security Administration under contract DE-NA0003525. We also acknowledge the 3D X-Ray Microscope Facility in the Department of Physics for the images shown in this presentation, which were acquired on a Zeiss Xradia 510 Versa 3D X-ray Microscope that was supported by the EVPRP Major Multi-User Equipment Program 2017 at Purdue University. This material is also based upon work supported by the National Science Foundation (1932312-CMMI).

# TABLE OF CONTENTS

LIST OF TABLES . . . . .	8
LIST OF FIGURES . . . . .	9
LIST OF SYMBOLS . . . . .	14
ABBREVIATIONS . . . . .	15
ABSTRACT . . . . .	16
1 INTRODUCTION . . . . .	19
1.1 Rock Fracturing . . . . .	19
1.1.1 Behavior of Anisotropic Rocks . . . . .	19
1.1.2 Loading Modes . . . . .	22
1.1.3 Linear elastic fracture mechanics(LEFM) . . . . .	23
1.2 AE Monitoring . . . . .	25
1.3 Cross Coupling . . . . .	25
1.4 Problem Statement . . . . .	27
1.5 Research Objectives . . . . .	27
1.5.1 Mineral Texture Orientation . . . . .	27
1.5.2 Remote Probing of Fracturing of Anisotropic Materials . . . . .	28
1.5.3 Oriented Fracture Voids . . . . .	28
1.6 Document Organization . . . . .	28
2 EXPERIMENTAL METHODS FOR MECHANICAL PROPERTY STUDY . . . .	31
2.1 Sample Fabrication . . . . .	31
2.1.1 3D Printing . . . . .	31
2.1.2 3D Printed Gypsum Sample Design for 3PB Tests . . . . .	32
2.1.3 3D Printed Gypsum Sample Design for UCS and Brazilian Tests . . . .	33
2.2 Loading Configurations . . . . .	34
2.2.1 UCS and Brazilian Tests Experimental Setup . . . . .	34

2.2.2	Three Point Bending (3PB) Tests . . . . .	35
2.2.3	UCS Test in Xray Machine with Deben . . . . .	35
2.3	Material Properties Measurements . . . . .	36
2.3.1	XRD of Bassanite Powder and Printed Samples . . . . .	36
2.3.2	Seismic Measurements of Sound Speed Through Printed Samples . .	37
2.3.3	Mechanical Properties Studied by UCS and Brazilian Tests . . . . .	38
2.4	Fracture Characteristic Measurements . . . . .	39
2.4.1	Xray CT . . . . .	39
2.4.2	Laser Profilometry . . . . .	39
2.4.3	Surface Roughness Analysis . . . . .	40
3	EFFECT OF MINERAL TEXTURE ORIENTATION RELATIVE TO LAYER- ING ON TENSILE FRACTURES (MODE I) . . . . .	53
3.1	Influence of Mineral Texture on Failure Load . . . . .	53
3.2	Influence of Mineral Texture on Fracture Surface Roughness . . . . .	54
3.3	Mineral Texture Controls on Fracture Fluid Flow . . . . .	60
3.4	Conclusions . . . . .	61
4	EFFECT OF MINERAL TEXTURE ORIENTATION RELATIVE TO LAYER- ING ON FRACTURES INDUCED BY MIXED MODE LOADING . . . . .	62
4.1	Mixed Mode I and II . . . . .	62
4.1.1	Peak Load . . . . .	62
4.1.2	Fracture Path . . . . .	63
4.1.3	Fracture Roughness . . . . .	65
4.1.4	Conclusion . . . . .	66
4.2	Mixed Mode I and III . . . . .	67
4.2.1	Fracture Path . . . . .	67
4.2.2	Fracture Roughness . . . . .	67
4.2.3	Conclusion . . . . .	68

5	ACOUSTIC EMISSION FROM LAYERED MEDIA DURING UNIAXIAL COMPRESSION TESTING . . . . .	78
5.1	Sample Fabrication . . . . .	78
5.2	Experimental Setup and Procedure . . . . .	79
5.3	Results . . . . .	80
5.4	Deben Results . . . . .	82
5.5	Conclusion . . . . .	83
6	CONVERTED WAVES FROM ORIENTED VOIDS IN FRACTURES . . . . .	86
6.1	Numerical Modeling . . . . .	86
6.2	Experimental Approach . . . . .	87
6.2.1	Samples . . . . .	88
6.2.2	Ultrasonic Measurements . . . . .	90
6.2.3	Calibration . . . . .	91
6.3	Results . . . . .	91
6.3.1	Simulate Shearing Along Fracture with Oriented Voids . . . . .	91
6.3.2	Fixed Void Spacing and Fixed Void Geometry but Variable Angle . . . . .	92
6.3.3	Fixed Void Spacing and Fixed Void Angle but Different Void Geometry . . . . .	94
6.3.4	Fixed Void Angle and Fixed Void Geometry but Different Spacing . . . . .	95
6.4	Wave Propagation Through Oriented Voids Filled with Viscous Fluids . . . . .	96
6.5	Conclusions . . . . .	98
7	SUMMARY . . . . .	105
	REFERENCES . . . . .	109
A	MATLAB CODE . . . . .	115
A.1	Load and displacement reading . . . . .	115
A.2	Load and displacement plotting . . . . .	116
A.3	Fracture surface 3D plot . . . . .	117
A.4	Fracture surface micro slope distribution . . . . .	120
A.5	Fracture surface auto correction . . . . .	125

A.6	For Figure 3.5 . . . . .	128
A.7	Fracture surface micro slope full width at half maximum . . . . .	130
A.8	For Figure 3.3 . . . . .	133
A.9	Digital image correlation (DIC) information extraction from analyzed data .	137
A.10	DIC of single image . . . . .	138
A.11	DIC synced with load displacement data and seismic waves . . . . .	141
A.12	Monitor honey coupling of transducers for 24 hours . . . . .	145
A.13	Experimental seismic waves (chapter 6) . . . . .	145
A.14	Stimulated seismic waves (chapter 6) . . . . .	147
A.15	Wavelet transformation of seismic waves . . . . .	158
A.16	For Figures 6.17,6.18,6.19 . . . . .	163
VITA	. . . . .	168

## LIST OF TABLES

2.1	Xray-CT Settings . . . . .	51
4.1	Full width half maximum (FWHM) values of the micro slope distributions in both X and Y directions from the fracture surfaces formed with different bedding layer and mineral growth directions and different notch locations (samples type A, B, C). . . . .	66

## LIST OF FIGURES

1.1	(a) Sketch of corrugated fracture surfaces. (b) Corrugated fracture in volcanic rock in Hawaii, USA. (c) Corrugated fracture surfaces in sedimentary rock in Lederderg Park, Australia. ( <i>Photographs courtesy of Pyrak-Nolte</i> ) . . . . .	20
1.2	Sketch of layering relative to the 3PB notch[12] . . . . .	21
1.3	Three basic modes of loading and it's crack surface displacements[19] . . . . .	23
1.4	Mode I fracture stiffness for 3PB testing[16] . . . . .	24
1.5	Transmission and Reflection of plane waves on a fracture with coupling fracture stiffnesses. . . . .	30
2.1	Scanning Electron Microscopy (SEM) images of (left) bassanite powder, (center) gypsum crystals formed from the binder application, and (right) clusters of gypsum crystals. . . . .	32
2.2	Depiction of 3D printing process of gypsum samples: (a) deposition of 0.1 mm thick layer of bassanite powder ( $2CaSO_4 \cdot H_2O$ ) on printing area in the blue arrow direction; (b) printer head spreading water-based binder in the direction of the red arrow . . . . .	33
2.3	Nomenclature of layered samples for tensile fractureing (a,b) Arrestor, (c,d) Short Traverse, and (e,f) Divider. Solid blue lines represent layering. Red dashed lines represent binder direction during 3D printing. . . . .	34
2.4	Moving Notch away from the center to introduce Mode II component . . . . .	35
2.5	Sample design for mixed Mode I and III tests . . . . .	36
2.6	Sample design for mixed Mode I and III tests with notches tilted at angles of $60^\circ$ , $45^\circ$ , $30^\circ$ , and $20^\circ$ . . . . .	37
2.7	Sample design for UCS and Brazilian tests . . . . .	38
2.8	Experimental setup of UCS test . . . . .	42
2.9	Experimental setup of Brazilian test . . . . .	43
2.10	(a) Sketch of Brazilian test top jaw (unit: inch); (b) Sketch of Brazilian test bottom jaw (unit: inch) . . . . .	44
2.11	Experimental setup for 3 point bending (3PB) test . . . . .	45
2.12	Sketch of location and dimension of the rods and sample for 3PB tests . . . . .	45
2.13	Figures of Deben stress equipment: (a) the top and bottom pieces to be confined by screws to make a fixed frame; (b) the jaw for 3PB test; (c) the jaw for compressional test. . . . .	46
2.14	Scales of the 3PB tests in Xray by Deben tool . . . . .	46

2.15	XRD analysis of printing powder . . . . .	47
2.16	XRD analysis of printed samples . . . . .	47
2.17	(a) Sketch of the printed structure of a cube and notation of faces and SV and SH polarizations; (b) Compression wave (P) speed;(c) Shear wave (SV) speed;(d) Shear wave (SH) speed measured by seismic transmissions in three directions . .	48
2.18	Load and displacement curves of UCS tests of type H cylinders . . . . .	49
2.19	Load and displacement curves of UCS tests of type V cylinders . . . . .	49
2.20	Load and displacement curves of UCS tests of type T cylinders . . . . .	50
2.21	Load and displacement curves of Brazilian tests of cylinders with layers perpendicular to the loading direction . . . . .	50
2.22	Surface roughness measurement setup: (a) failed sample and coordinates for the asperity data; (b) laser profilometer setup with a piece of the fracture surface facing up . . . . .	52
3.1	(a) Load-displacement graph for cast gypsum and representative 3D printed samples. (b) Average relative peak load from 4 cohorts of samples for the cast and geo-architected samples. The samples are color-coded to match the colors in load-displacement curves (values are relative to H samples). . . . .	54
3.2	2D x-ray radiographs of the small geo-architected samples at 5% of peak load and just prior to complete failure. The direction of fracture propagation from the notch (at the bottom of each image) is in the y-direction. The x-direction is into the page. . . . .	55
3.3	(a) Average full width - half maximum of the microslope distribution for the cast gypsum and geo-architected samples which are color-coded to match the load-displacement curves in Figure 3.1. (b) Simulated fluid permeability based on surface roughness data from the cast gypsum and geo-architected samples (Figures 3.4 & 3.5). Solid color: in the direction of fracture propagation ( <i>y-direction</i> ); Hatched/shaded Color: in the direction perpendicular to fracture propagation ( <i>x-direction</i> ) . . . . .	56
3.4	(a) 3D surface and 2D contour of surface roughness for the cast gypsum sample (y direction is the direction of fracture propagation). (b) Normalized autocorrelation function for the cast gypsum sample. . . . .	58
3.5	3D surface and 2D contour of surface roughness and the normalized 2D autocorrelation function for the geo-architected samples grouped. Note: All axes are the same as those shown in Figure 3.4. . . . .	59



3.6	Image from 3D X-ray tomographic reconstruction of small sample H post-peak showing the fracture trace in the (a) Side view showing the fracture trace in the direction of fracture propagation from notch to top of sample (y-direction) with layer direction indicated by the small yellow arrows. (b) Top view showing the fracture trace in the x-direction and gypsum mineral banding. Scale bars in each image represent 1 mm. . . . .	60
4.1	3D printed samples for three-point bending tests. The blue lines in the figure show the orientation of the basanite layers (BL) and the red lines, the orientation of in-plane mineral growth (MG). The location of the notches are denoted by the black, purple or green marks. . . . .	63
4.2	(a) Load and displacement curves of 3PB tests among 6 sample geometries when the notch is located at the center (type C);(b) when the notch is located 9.53 mm away from the center (type B);(c) when the notch is located 19.05 mm away from the center (type A) . . . . .	64
4.3	(a) Fracture paths for a group of samples under Mixed Mode I and II loading (type B);(b) Fracture paths for a group of samples under Mixed Mode I and II loading (type B). . . . .	64
4.4	(a) Fracture paths for a group of samples under Mixed Mode I and II loading (type A);(b) Fracture paths for another group of samples under Mixed Mode I and II loading (type A). . . . .	65
4.5	Fracture paths for a group of samples under Mixed Mode I and II loading (type B) in Deben with 2D Xray projection shown similar results as the Figure 4.3 . .	70
4.6	(a)Micro-slope angle distributions in the loading direction (Y) and sample thickness direction (X) of H samples' fractures under loading type C; (b)type B; (c)type A . . . . .	71
4.7	(a)Micro-slope angle distributions in the loading direction (Y) and sample thickness direction (X) of Halt samples' fractures under loading type C; (b)type B; (c)type A . . . . .	71
4.8	(a)Micro-slope angle distributions in the loading direction (Y) and sample thickness direction (X) of V samples' fractures under loading type C; (b)type B; (c)type A . . . . .	71
4.9	(a)Micro-slope angle distributions in the loading direction (Y) and sample thickness direction (X) of Valt samples' fractures under loading type C; (b)type B; (c)type A . . . . .	72
4.10	(a)Micro-slope angle distributions in the loading direction (Y) and sample thickness direction (X) of VV samples' fractures under loading type C; (b)type B; (c)type A . . . . .	72

4.11	(a)Micro-slope angle distributions in the loading direction (Y) and sample thickness direction (X) of VValt samples' fractures under loading type C; (b)type B; (c)type A . . . . .	72
4.12	Photos of front and back faces of cast gypsum samples with notches tilted at angles of 60°, 45°, 30°, and 20° . . . . .	73
4.13	Photos of front and back faces of 3D printed gypsum samples (type H) with notches tilted at angles of 60°, 45°, 30°, and 20° . . . . .	73
4.14	3D view of the segmented reconstructed Xray CT tomography of sample fractures with different bedding layers and mineral growth orientation directions (Mixed Mode I and III notch angle 60°); bedding layer and mineral growth orientation directions regarding each sample type name are shown next to the fractures. . .	74
4.15	3D view of the segmented reconstructed Xray CT tomography of sample fractures with different bedding layers and mineral growth orientation directions (Mixed Mode I and III notch angle 45°); obvious thick chunk inside the fracture scan was the result of a missing piece after failure. . . . .	75
4.16	3D view of the segmented reconstructed Xray CT tomography of sample fractures with different bedding layers and mineral growth orientation directions (Mixed Mode I and III notch angle 30°); Some samples had fractures initiated not form the tip of the notch. . . . .	76
4.17	3D view of the segmented reconstructed Xray CT tomography of sample fractures with different bedding layers and mineral growth orientation directions (Mixed Mode I and III notch angle 20°); Some samples had fractures initiated not form the tip of the notch; some samples had more than one single fracture surfaces. .	77
5.1	Sketch of 3D printed samples showing orientation of the bassanite layers (blue lines) and oriented mineral feature (red dashed lines) and the load displacement curves of each type. . . . .	80
5.2	Test repeatability of UCS . . . . .	81
5.3	Estimated fracture location from AE and the reconstructed X-ray computed tomography images. . . . .	82
5.4	Micro slope and autocorrelation of induced surfaces for CG, H, and H45 samples	83
5.5	(a) The CG sample failed almost instantly and had the narrowest AE amplitude distribution in time; (b) The H45 sample had smoother fracture surfaces and a relatively narrower AE amplitude distribution compared to other 3DP samples; (c) The H sample exhibited the most significant ductile post-peak behavior, produced relatively rougher surfaces and a longer period of AE events. . . . .	84
5.6	AE Amplitude Distribution in Time with cross section view of 3D reconstructed Xray CT tomography indicates the fracturing started after the peak load was reached (UCS-T type sample as Figure 2.7). . . . .	85

6.1	Structure of the modeling . . . . .	86
6.2	Simulated transmitted (upper left) P-P, (lower left) S-S, (upper right) P-S and (lower right) S-P for fracture void orientations of $\theta = 0^\circ, 15^\circ, 30^\circ, 45^\circ, 60^\circ, 75^\circ$ , and $90^\circ$ . . . . .	88
6.3	X-ray CT reconstructed 3D image of 8 mm portion of the $45^\circ$ sample. . . . .	89
6.4	Actual dimensions of voids in the 3D printed sample for $\theta = 45^\circ$ . On average, the crack length was 1.7 mm and the width was 0.8 mm. . . . .	90
6.5	Simulate no shear along fracture with void orientations of $\theta = \pm 30^\circ, \pm 45^\circ, \pm 60^\circ$ (left); No P-S converted mode observed when there is no shearing (right). . . . .	92
6.6	Simulate small shear in two different directions along fracture with void orientations of $\theta = +45^\circ, -45^\circ, -45^\circ, \theta = +45^\circ, +45^\circ, -45^\circ$ (left); P-S converted mode observed when there is shearing (right). . . . .	93
6.7	Measured P to S converted modes of the same oriented microcrack inclination from $15^\circ$ to $75^\circ$ for both negative and positive orientations. . . . .	94
6.8	Simulated P-S conversion signals on positive and negative $45^\circ$ -oriented cracks. . . . .	95
6.9	P-S wave conversions emerged and increased in amplitude as the crack inclination increased from $0^\circ$ to $45^\circ$ . . . . .	96
6.10	P-wave amplitude increased, as the micro-crack orientation increased from $0^\circ$ to $90^\circ$ . . . . .	97
6.11	Transmission coefficients from normal incidence by experiments. . . . .	98
6.12	Transmission coefficients from normal incidence by simulation. . . . .	99
6.13	Experimentally measured S-S and P-P transmitted wave signals for voids with the same oriented angle ( $0^\circ$ ) and same spacing (3 mm) on samples with different void geometries. . . . .	100
6.14	Simulation results of S-P and P-S converted modes for voids with the same oriented angle ( $0^\circ$ ) and same spacing (3 mm) on samples with different void geometries. . . . .	100
6.15	Experimentally measured P-P and P-S wave signals for elliptical voids with the same oriented angle ( $45^\circ$ ) but different void spacing. . . . .	101
6.16	Simulation results of S-S and S-P wave signals for elliptical voids with the same oriented angle ( $45^\circ$ ) but different void spacing. . . . .	101
6.17	P-P transmission mode to fluid viscosity . . . . .	102
6.18	S-S transmission mode to fluid viscosity . . . . .	103
6.19	P-S converted mode to fluid viscosity . . . . .	104

## LIST OF SYMBOLS

2a	the crack length
B	thickness of the specimen
G	elastic energy release rate
H	arrester sample
Halt	arrester sample
K	stress intensity factor
$K_{Ic}$	fracture toughness
$K_x$	shear fracture stiffness
$K_{xz}$	cross-coupling stiffness
$K_z$	normal fracture stiffness
$K_{zx}$	cross-coupling stiffness
$N_W$	notch width
P	applied load
R	relative magnitude of the coupling compliance
$S_x$	x directional local slope
$S_y$	y directional local slope
V	short traverse sample
Valt	short traverse sample
VV	divider sample
VValt	divider sample
W	width of the specimen
X	position or direction
Y	position or direction
$\lambda$	wavelength
$\theta$	angle
$\theta_{save}$	average microslope angle
$\theta_{sx}$	x directional microslope angle
$\theta_{sy}$	y directional microslope angle

## ABBREVIATIONS

2D	2 dimensions
3D	3 dimensions
3PB	Three point bending
3DP	3D printed
AE	Acoustic emission
AST	Acoustic sensor transmission tests
BL	Basanite layers
CAD	Computer-aided design
CG	Cast gypsum
CTOA	Crack tip opening angle
CTOD	Crack tip opening displacement
DG	Discontinuous Galerkin
FT	Fourier transform
FWHM	Full width half maximum
LEFM	Linear elastic fracture mechanics
LVDT	Linear variable differential transformer
MG	Mineral growth
NDT	Non-Destructive Testing
ORS	Object research systems
P-waves	Compressional waves
P-P	Compressional to compressional
P-S	Compressional to shear
SEM	Scanning Electron Microscopy
S-waves	Shear waves
S-S	Shear to shear
UCS	Unconfined compressive strength
Xray-CT	Xray computed tomography
XRD	Xray diffraction

## ABSTRACT

Two longstanding goals in subsurface science are to induce fractures with a desired geometry to adaptively control the interstitial geometry of existing fractures in response to changing subsurface conditions. Many energy and water-related engineering applications that use induced fractures to withdraw and inject fluids from subsurface reservoirs occur in some sedimentary rock. Sedimentary rock such as shales often exhibit anisotropic mechanical properties because of bedding, layering and mineral texture. These structural and textural features also affect fracture formation and in turn the resulting fracture geometry. Understanding the interplay between the microscopic mineral fabric and structure and how it affects fracture geometry is important for the prediction of the geometry of induced fractures and to the determination of the most ideal conditions for maximizing energy production and minimizing leaks from sequestration sites in the subsurface.

This Ph.D. thesis research focuses on the formation and geometry of fractures in anisotropic rock and the identification of geophysical signatures of fracture formation using additively manufactured gypsum rock analogs. Specifically, the work is grouped into three topics: (1) material controls on fracture geometry, toughness and roughness in additively manufactured rocks; (2) acoustic emissions (AE) during fracture formation in anisotropic additively manufactured rocks; and (3) determination of the effect of fluid-filled oriented voids in fractures on compressional to shear wave conversions.

For topic (1), unconfined compressive strength (UCS), Brazilian and 3-point bending (3PB) tests under pure and mixed mode mechanical tests were performed on cast and 3D printed gypsum samples that were characterized using 3D Xray microscopy, Xray Diffraction and SEM to examine the micro-structure of the samples. Research on topic 1 discovered microstructural controls on fracture surface roughness and the failure behavior of anisotropic rock and that the failure mode (tensile, mixed mode I and II, mixed mode I and III) affects the fracture propagation path and the surface roughness which is controls to the flow paths through a fracture. The results suggest that detailed mineralogical studies of mineral texture/fabric in laboratory or core samples is important to unravel failure strength, surface roughness, and how fractures propagate in layered geological media.

For topic (2), UCS tests were performed with concurrent measurements of acoustic emissions (AE) on cylindrical specimens: cast gypsum (CG) samples, and 3D printed (3DP) samples with five different orientations of bassanite layer and gypsum texture relative to the loading direction. Mechanical properties and induced fracture surface information were compared with the collected the AE signals to study if there is a way to tell the differences between the induced fracture surfaces with the AE signals patterns together with loading data. Examination of the AE signal amplitude from post-peak loading revealed that more ductile behavior was associated with more AE events that occurred over a longer period of time, and the resultant fracture surfaces were rougher than for narrow time distributions of events.

For topic (3), a detail study of fracture void orientation was performed using ultrasonic compressional, P, and shear, S, waves to determine how energy is partitioned when P-to-S or S-to-P conversions occur for waves normally incident on an air-filled or fluid-filled fracture. In this study, experiments and computer simulations were performed to demonstrate the link among cross-coupling stiffness, micro-crack orientation and energy partitioning into P, S, and P-S/S-P wave. The cross-coupling stiffness was created by 3D printing samples with linear arrays of micro-cracks oriented at  $0^\circ$ ,  $\pm 15^\circ$ ,  $\pm 30^\circ$ ,  $\pm 45^\circ$ ,  $\pm 60^\circ$ ,  $\pm 75^\circ$ , and  $90^\circ$ . For  $45^\circ$  orientation, measurements were made on air-filled and fluid-filled (silicon oil). For the air-filled fractures, the observed energy partitioning matched the simulated behavior obtained from discontinuous Galerkin simulations. Information on local fracture geometry is contained in the far-field waves. When filled with a viscous fluid, the P- and S- waves amplitude exhibited slight increases and decreases, respectively. The P-to-S converted mode amplitude decreased 30% with an increase in fluid viscosity from 1–300kcSt. This suggests that P-S converted mode provides a potential method to remotely probe changes in fluid viscosity in fractures.

The work from the 3 research topics demonstrated that micro-scale structure impacts macroscale behavior and signals used for monitoring the condition of a rock. Additively manufactured samples enabled the exploration and determination of (1) the impact of mineral fabric orientation in layered media on failure load, fracture propagation path, and fracture surface roughness, (2) the sensitivity of P-to-S conversions to fluid viscosity, and (3) how

oriented voids within a fracture effect energy partitioning. These research findings advances our current understanding of role microscopic properties and structure on the generation, propagation and geometry of induced fractures in anisotropic rock, and help to identify the best imaging modalities to use to identify the seismic signatures of the viscosity of fluids in fractures with oriented voids. These contributions will help unravel the complex behavior often observed in natural rock that is structurally and compositionally complex with features and heterogeneity.



# 1. INTRODUCTION

Portions of the introduction chapter are from the paper Jiang, L., Yoon, H., Bobet, A. et al. Mineral Fabric as a Hidden Variable in Fracture Formation in Layered Media. Sci Rep 10, 2260 (2020). <https://doi.org/10.1038/s41598-020-58793-y>, an open access article under the terms of Creative Commons and with permission from the American Rock Mechanics Association (ARMA) to use material from Liyang Jiang’s ARMA conference proceedings.

## 1.1 Rock Fracturing

### 1.1.1 Behavior of Anisotropic Rocks

The hydraulic integrity of any subsurface site will be affected by the presence of induced or pre-existing fractures that form highly conductive preferential flow paths. Subsurface flow affects the long-term sequestration of anthropogenic waste, determines the production potential of hydrocarbon reservoir and geothermal energy, and maintains the safety of exploitable aquifers. The conductivity of flow paths is controlled by fracture geometry that can be altered over time from physical and chemical processes [1]–[4]. When a fracture is generated in rock, two rough surfaces define the void space through which fluids will flow. When corrugated surfaces emerge (e.g Figure 1.1), flow parallel to ridges and valleys is mostly unobstructed compared to the more tortuous path for flow orthogonal to the ridges. Thus knowledge of the presence and orientation of corrugated surfaces enables design strategies for maximizing flow potential.

This raises the fundamental question in fracture mechanics of what gives rise to corrugated surfaces. The roughness of fracture surfaces is known to be affected by mineralogy (mineral fabric, bond strength, spatial distributions), structural features (layers, microcracks, etc.), stress orientation, failure mode, and geochemical interactions that can alter mineral bond strength. However, the inherent heterogeneity in mineral phases and composition among rock samples causes a difficulty in identifying the contributions to surface roughness from each of these rock properties and processes, even when extracted from the same rock mass. The spatial variability in compositional and structural features prevents

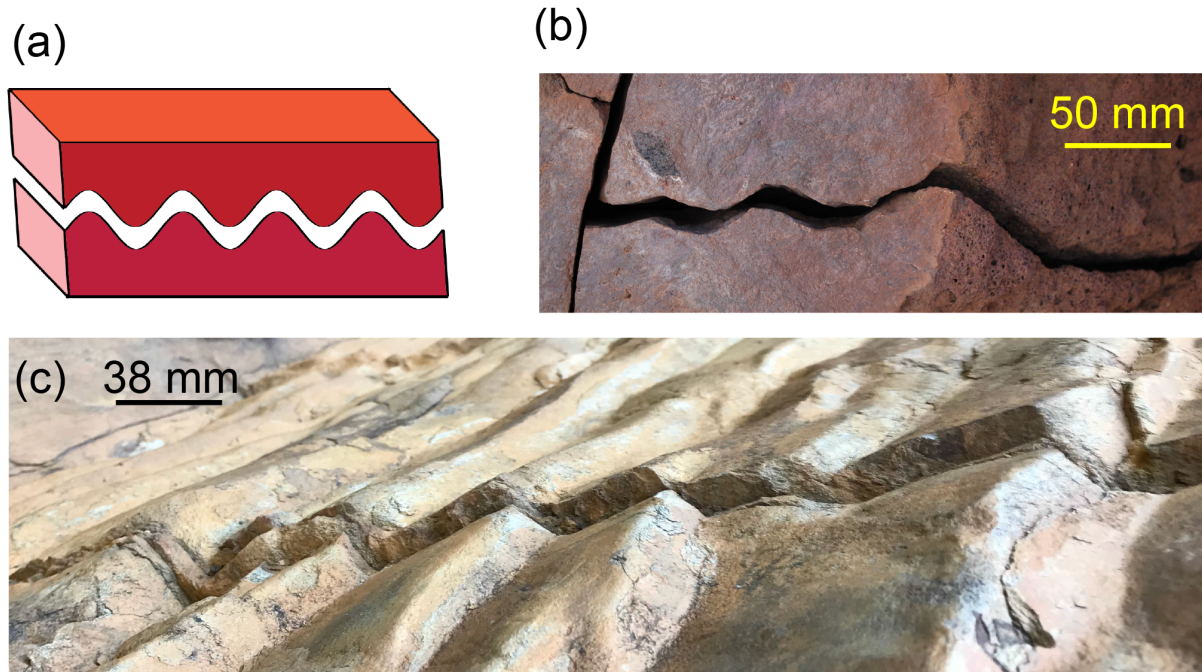


**Figure 1.1.** (a) Sketch of corrugated fracture surfaces. (b) Corrugated fracture in volcanic rock in Hawaii, USA. (c) Corrugated fracture surfaces in sedimentary rock in Lederberg Park, Australia. (*Photographs courtesy of Pyrak-Nolte*)

reproducible measurements of fracture formation, deformation, and other physical and chemical properties.

In nature, rock forms through different geological processes that generate compositional, textural, and structural features. A primary structural feature of sedimentary rocks is layering that arises from depositional, compactional and diagenetic processes. In addition, within a layer, a rock also contains textural features related to the arrangement of mineral components that can range from interlocking crystals, to foliations, or to fragments with either preferred mineral orientation or amorphously distributed. Past research has shown that layers or preferred mineral orientations are known to affect the mechanical properties of rock leading to direction dependent or anisotropic elastic moduli. As examples, the anisotropy in elastic properties of shale is attributed to preferred orientation of clay minerals [5]–[8], and the preferred orientation of minerals is assumed to explain the seismic anisotropy of the Earth’s inner core [9].

A key question is how do compositional, textural, and structural features affect fracture formation and the resulting fracture geometry through which fluids flow. Past and current research has shown that fracture toughness, i.e., the ability of a material to resist fracturing, is affected by layer orientation (Figure 1.2), with the geometry of the layers referred to as arrester, divider, and short traverse (Figure 1.2). For shale, many studies have observed that fracture toughness is ranked by the orientation of the layers with divider > arrester > short traverse [10], [11]. However, other studies have observed cases where fracture toughness is comparable between arrester  $\approx$  divider or between arrester  $\approx$  short traverse or values of fracture toughness for the short traverse specimens exhibit both the highest and lowest values [12]. These differences from the expected ranking of fracture toughness have been attributed to percent kerogen, inelasticity, clay, variable elastic properties among layers in shale, and microfractures [12]–[14].

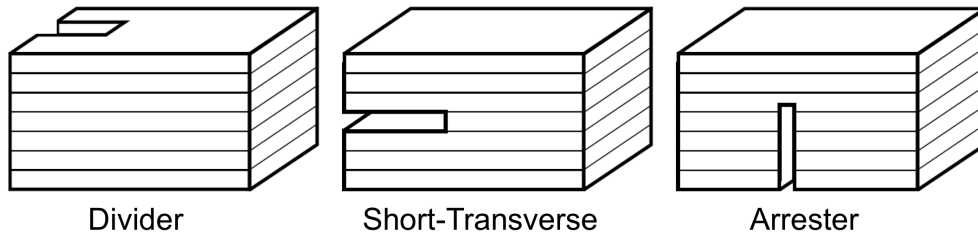


**Figure 1.2.** Sketch of layering relative to the 3PB notch[12]

In this study, we examine the role of mineral texture orientation in layered rock on tensile fracture formation and geometry, and on fracture flow properties. Little is known as to whether mineral orientation within the layers affects tensile fracture formation and fracture toughness, especially when layering and minerals are not aligned. To investigate the role of mineral orientation on tensile fracture formation and geometry, we performed three point bending experiments (3PB) on "geo-architected rock" with controlled directions of layering and mineral texture orientation to identify the contribution from each on tensile failure, surface roughness and permeability.

The "geo-architected" layered rock samples with preferred mineral fabrics were created using a 3D printing process. Layers of bassanite were bonded with a proprietary water-

based binder that produced gypsum as a reaction product. The gypsum mineral fabric direction is oriented by the direction of the binder spreading. When one layer of bassanite is deposited on a previous layer, gypsum crystals form bonds within the layer as well as between bassanite layers after application of the binder. Mineral fabric arises because the gypsum forms stronger bonds between gypsum crystals than between the gypsum crystals and bassanite powder.

The geo-architected rock exhibits anisotropic mechanical properties as determined from ultrasonic measurements of compressional and shear wave velocities. Anisotropy in these samples arises from two sources: (1) the formation of bassanite layers from the successive deposition of bassanite powder during manufacturing; and (2) the direction of mineral fabric which is controlled by the binder application direction. The samples exhibit orthorhombic anisotropy, similar to behavior observed in rock with preferred crystallographic or shape orientation [8].

### 1.1.2 Loading Modes

Griffith developed an energy balance theory to solve fracture initiation and propagation problems based on linear and elastic assumptions. Fracture toughness testing has been recognized a key method to provide accurate toughness values that are needed for linear elastic fracture mechanics and elastic/plastic fracture mechanics. Three point bending (3PB) tests on analogy rocks shown an obvious ductile post peak behavior [15]. How to estimate the fracture toughness of this material is a question. Here a short review is given on previous approaches to determine fracture toughness when linear elastic fracture mechanics is not sufficient to interpret the fracturing process. The stress intensity factor  $K$  (or the elastic energy release rate  $G$ ), the J-integral, the crack tip opening displacement (CTOD), and the crack tip opening angle (CTOA) are the most important parameters used in fracture mechanics. Material deformation can be classified as being linear elastic, nonlinear elastic, or elastic plastic. The deformation behavior of a material determines which fracture parameter to use to describe fracture toughness and which fracture test method to perform to measure the toughness value for the material [16]. For brittle fracture, linear elastic deformation zone

dominates the crack tip and the initiation toughness dominates the material fracture resistance. Thus, the toughness is often measured as a point value and characterized by the stress intensity factor  $K$  or the energy release rate  $G$  at crack initiation. For tougher materials, the tearing resistance to crack growth can be significant. Measuring the  $K$  vs  $R$  curve of a relatively tough thin sheet of material was developed to interpret the fracturing process. For ductile fracture, plastic deformation dominates at the crack tip and the toughness is often described in a resistance curve format using the J-integral or CTOD ( $\delta$ ) [16].

### 1.1.3 Linear elastic fracture mechanics(LEFM)

The fundamental mechanism of failure in rock or other materials can be established from a simplified ideal model that represents a material as continuous, homogeneous, isotropic and linearly elastic. In general, the crack tip in an ideal linear elastic brittle material can be subject to three different type of stress (Figure 1.3). For each loading mode, the stress distribution is proportional to a respective constant which is independent of location. The constant is only related to the size of the crack and the loading. The parameter is called fracture stiffness with different forms for each stress mode (Figure 1.3) and taken to be proportional to the square root of strain energy release rate of each mode [17], [18].

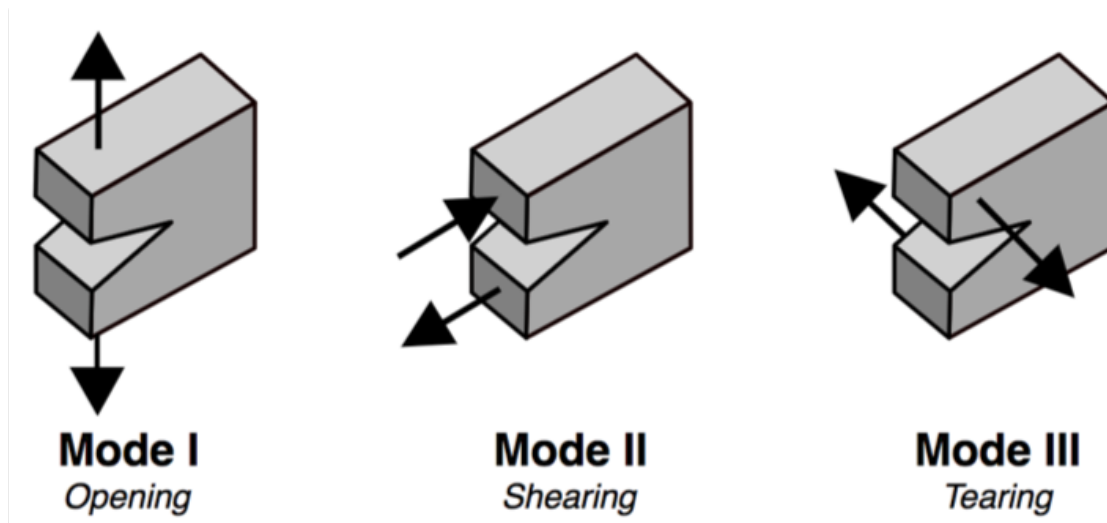
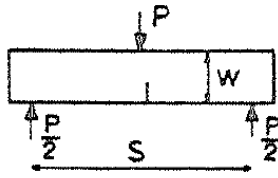


**Figure 1.3.** Three basic modes of loading and it's crack surface displacements[19]

3PB test is one type of common test to evaluate fracture toughness because minimal alignment is required compared to other measurement techniques. The quality of the results from 3PB tests are affected by the specified test fixture and details of the test preparation, conditioning, and conduct of the test. The sample is placed on two supporting pins (i.e. rods or rollers) and also loaded with a pin on the top surface. Fracture stiffness is purely related to the sample geometry and load. When the failure occurs, the fracture stiffness reached the value of fracture toughness. Therefore, sample size, fracture toughness or crack size can be calculated if the other two values are known. By picking a certain sample size, and reading the peak load, the fracture toughness can be predicted.



Thickness B

$$K_I = \frac{PS}{BW^{3/2}} \left[ 2.9 \left( \frac{a}{W} \right)^{1/2} - 4.6 \left( \frac{a}{W} \right)^{3/2} + 21.8 \left( \frac{a}{W} \right)^{5/2} - 37.6 \left( \frac{a}{W} \right)^{7/2} + 38.7 \left( \frac{a}{W} \right)^{9/2} \right]$$

**Figure 1.4.** Mode I fracture stiffness for 3PB testing[16]

The equation for fracture toughness,  $K$ , is shown in Figure 1.4. In the equation,  $P$  is the applied load,  $B$  is the thickness of the specimen,  $2a$  is the crack length, and  $W$  is the width of the specimen. In 3PB, a fatigue crack can be created at the tip of by cyclic loading prior to loading to create a notch. From the load - crack opening displacement data, the load at which a crack starts to grow can be determined. This load is substituted into the formula above to find the fracture toughness  $K_{Ic}$ . Thus, the fracture toughness can be taken to be proportional to the peak load. For the research presented in this thesis, notch was printed instead of being created by cyclic loading to improve the repeatability of the tests. However, this will lead to an over estimation of the fracture toughness because the printed notch does not have constraint stress at the tip as assumed in theory.

## 1.2 AE Monitoring

Acoustic emission (AE) uses sensors to capture events that take place inside a solid material. Conjoint with other Non-Destructive Testing (NDT) techniques it can be used to assess structural integrity. For the study of fracture mechanics of the geo-architected rocks, acoustic emission signals are generated during fracture processes as flaws are developing in materials under stress. The AE sensor (typically piezoelectric) transforms a local material displacement due to stress to an electrical signal. There are other types of sensors like capacitive transducers or laser interferometers can be used in other circumstances. Typical frequency range in AE applications varies between 20 kHz and 1 MHz. Preamplifiers are also often used to amplify initial signal. Typical amplification gains are 20, 40 or 60 dB. Then, a data acquisition device will do conversion of analog-to-digital signals, with filtration, hits (useful signals) detection. The system also does signal parameters evaluation, data analysis and graphing. Detection of AE signals is usually based on threshold, which means a hit is triggered when wave amplitude exceeds a fixed threshold. Locationing can be done by AE monitoring with time difference between signal arrivals to different sensors. Another application is material inspection for environmental cracking including corrosion cracking, hydrogen embrittlement, fatigue and creep crack growth[20]. In this thesis work, it was used to study of fracture developing.

## 1.3 Cross Coupling

Fractures in rock are potential pathways for fluids to flow through a rock mass and planes of mechanical instability that can lead to failure. Micro-seismicity and time-lapse geophysical surveys are often used to locate and delineate fractures [21]–[25], but there is a need to extract physically measurable parameters that are directly linked to hydraulic and mechanical properties of fractures. Recently, a scaling relationship between fluid flow and fracture specific stiffness for a fracture has been demonstrated to exist that accounts for spatial correlations in the fracture aperture distribution [2], [26]–[28]. Fracture specific stiffness, also known as unit joint stiffness, was introduced by [29] to describe the behavior of a fracture because it could be measured in the laboratory without detailed analysis of



the fracture geometry. Fracture specific stiffness is also used in theoretical models for elastic waves propagation across a fracture to capture the complexity of the fracture void geometry (i.e., spatial and probability distribution of aperture and contact area) [30]–[37]. These studies have shown that a fracture behaves as a low pass filter resulting in transmission, reflection coefficients that are frequency-dependent and depend on fracture stiffness. A key question is there information in a transmitted/reflected signal that would provide additional information on the fracture void geometry.

Nakagawa et al. [38] showed experimentally, theoretically, and numerically that information on the fracture void geometry is contained in P-S or S-P converted modes (P-compressional waves, S-shear waves). They demonstrated that even at normal incidence, a fracture plane composed of oriented voids (or micro-cracks) will generate S-P/P-S wave conversions. The conversions arise from a cross coupling stiffness that can occur along rough surfaces (Figure 1.5). In their study, the micro-cracks in the array were oriented at  $\pm 45^\circ$ , and the cross-coupling stiffness was controlled through the application of shear and normal stress. In this thesis work, laboratory measurements and numerical simulations of P-S/S-P conversions were compared to present the link among cross-coupling stiffness, normal and shear stiffness, micro-crack orientation and energy partitioning into P, S, and P-S/S-P wave and to determine the effect of oriented micro-cracks on the interpretation of fracture geometry.

In the displacement discontinuity theory for wave propagation across a fracture, the fracture is represented by a set of boundary conditions between two elastic half spaces [30]–[37]. The boundary conditions are continuity of stress, and a discontinuity in displacement that is inversely proportional to the fracture stiffness (either normal,  $K_z$ , or shear,  $K_x$ , in Figure 1.5). Nakagawa et al. [38] extended this theory to include cross-coupling stiffnesses,  $K_{zx}$  and  $K_{xz}$ . They showed that cross-coupling can occur from a periodic array of inclined cracks that leads to P-S and S-P conversions. The amplitude of the P-S/S-P conversions depend on the frequency of the signal and  $R$  which is defined as  $R = \sqrt{\frac{K_{zx} \cdot K_{xz}}{K_{xx} \cdot K_{zz}}}$ . The P-S/S-P transmitted and reflected wave amplitudes increase with increasing  $R$ . In their study, the contact area between the voids was maintained constant yielding a variation in void volume of the fracture.



From their simulations, the stiffness becomes infinitely large for  $R=1$  which for their geometry occurred for cracks inclined at angles larger than  $63^\circ$ . Here, the focus of the research is on the effect of void inclination angle on P-S and S-P conversions for a fixed void volume but variable contact length.

## **1.4 Problem Statement**

There is a need to extract physically measurable parameters that are directly linked to the hydraulic and mechanical properties of fractures from geophysical or other measurements. One difficulty is that rock is a complicated material because of the inherent heterogeneity in mineral phases and composition, even when extracted from the same rock mass. The spatial variability in compositional and structural features prevent reproducible measurements of deformation, fracture formation and other physical and chemical properties. One way to overcome this difficulty is to 3D print synthetic rock to enable control of the matrix properties and structural features. This research takes advantage of 3D printed rock to (1) determine the link between micro-scale mineral orientation in layered medium and the formation and properties of induced fractures; (2) study whether acoustic emission measurements during failure will provide information on the geometry of an induced fracture; and (3) understand the link between fracture specific stiffness and oriented fracture void geometry.

## **1.5 Research Objectives**

### **1.5.1 Mineral Texture Orientation**

Data from experiments of induced tensile failure in layered rock have shown that peak strength or failure load is affected by the relative orientation between the direction of loading and the layers. Often conflicting results arise about the relative strengths of layered rock based on layer orientation. Here, the objective is to use geo-architected 3D printed synthetic gypsum rock to produce reproducible samples to determine the effect of mineral texture orientation on fracture formation, fracture surface roughness, acoustic emission generation, and volumetric flow rate through tensile fractures.

### 1.5.2 Remote Probing of Fracturing of Anisotropic Materials

Here the objective is to determine if there is link between AE signals during failure of rock and fracture roughness for different the mineral and layering orientations. Examination of acoustic emission (AE) signal amplitude from post-peak loading reveals that more ductile behavior is associated with more AE events that occur over a longer period of time, and that the resultant fracture surfaces are rougher than for samples where AE events that occur over a narrow time distribution.

### 1.5.3 Oriented Fracture Voids

The theory for cross-coupling stiffness [38] shows that partitioning of energy among transmitted, reflected and converted waves modes is linked to the fracture specific stiffness (normal, shear and cross-coupling) and orientation of the voids in the fracture. Here, laboratory measurements are performed on 3D printed fractures with controlled void orientations to enable an improved understanding of the link between cross-coupling stiffness and fracture void geometry; and to determine the effect of fluid-filled oriented microcracks on energy partitioning.

## 1.6 Document Organization

This document includes 6 chapters that present the outcomes of the study of microstructural controls on macro-scale properties of rock.

Chapter 1 is the introduction while chapter 2 is the experimental methods.

Chapter 3 is adapted from a paper “The Influence of Mineral Texture on Fracture Geometry in Layered Geo-Architected Rock” published in Scientific Reports [15], [39]. The chapter describes the experimental and simulation work performed on geo-architected 3D printed synthetic gypsum rock to show that mineral texture orientation governs the isotropy or anisotropy in fracture surface roughness and volumetric flow rate through tensile fractures.

Chapter 4 presents a study related to work on to the contribution to failure from both shear and tensile stresses in anisotropic synthetic rock [40]. Failure loads, fracture path,

fracture roughness have been studied by using 3 point testing on samples with off-center notchese for mixed Mode I and II cases and rotated notcsh for mixed Mode I and III cases.

Chapter 5 is adapted from the paper “Monitoring Fracture Formation in Additively Manufactured Anisotropic Rocks” published in 2019 Acoustic Emission Working Group Proceedings[41]. It describes the experimental work that explores the effects of oriented layers and texture (oriented minerals) on fracture evolution in 3D printed gypsum samples by using acoustic emission measurements.

Chapter 6 is adapted from a proceeding paper entitled “Elastics wave conversion from fractures with oriented void” on 53rd US Rock Mechanics/Geomechanics Symposium[42]. This chapter also includes additional results related to the effect of fluid viscosity in transmission and conversion waves.

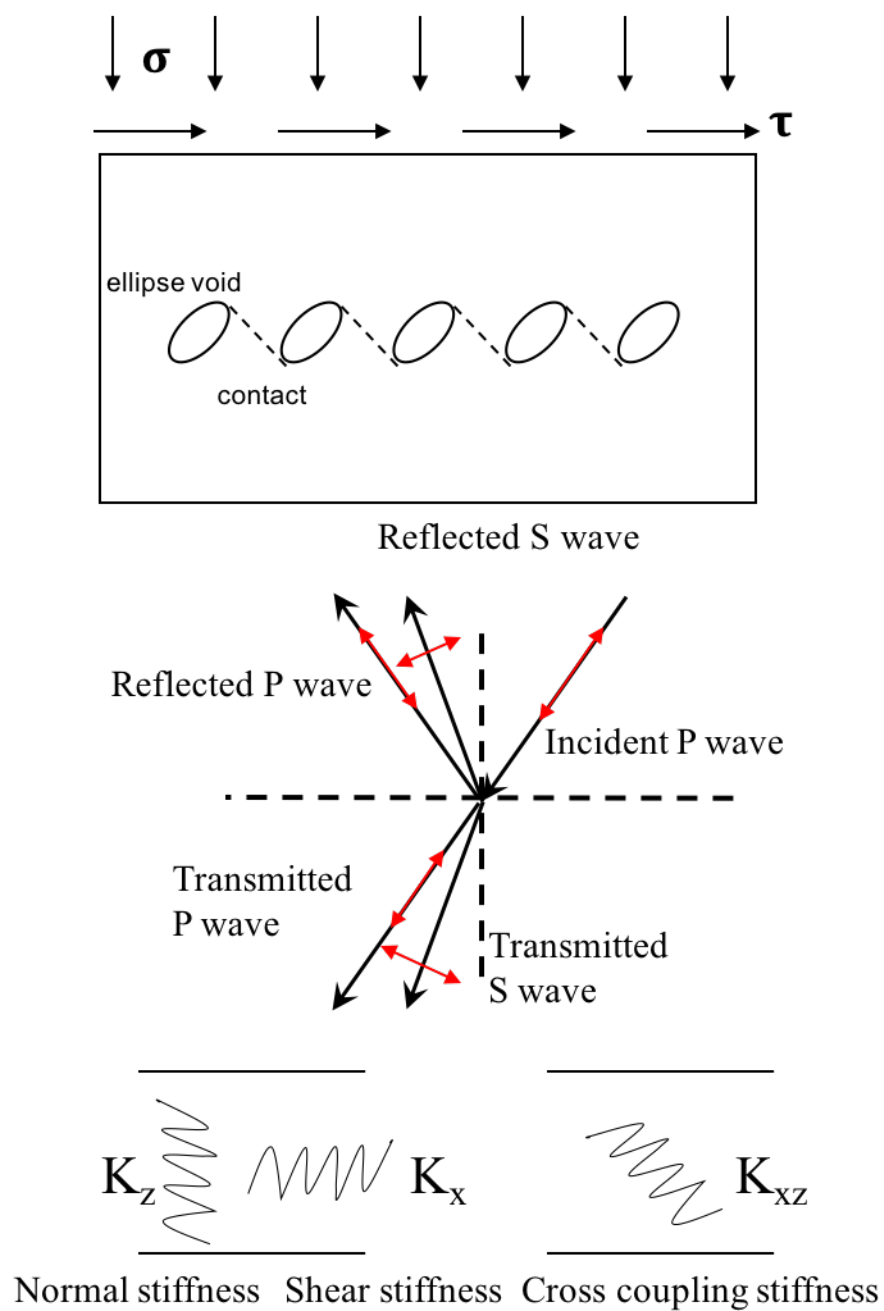


**Figure 1.5.** Transmission and Reflection of plane waves on a fracture with coupling fracture stiffnesses.

## 2. EXPERIMENTAL METHODS FOR MECHANICAL PROPERTY STUDY

In this chapter, the experimental methods used to study the the mechanical properties and behavior of anisotropic rock are presented. The subsequent 2 chapters contain the experimental results for different loading conditions, namely purely tensile (Mode I), and mixed tensile-shear conditions (Mode I-II and Mode I-III). Portions of the method chapter are from the paper Jiang, L., Yoon, H., Bobet, A. et al. Mineral Fabric as a Hidden Variable in Fracture Formation in Layered Media. Sci Rep 10, 2260 (2020). <https://doi.org/10.1038/s41598-020-58793-y>, an open access article under the terms of Creative Commons and with permission from the American Rock Mechanics Association (ARMA) to use material from Liyang Jiang’s ARMA conference proceedings. Images from the data set (Jiang, L., Pyrak-Nolte, L., Yoon, H., Bobet, A., Morris, J. (2021). Digital Image, X-ray CT , XRD and Ultrasonic Data Sets for Damage Mechanics Challenge on Brittle-Ductile Material. Purdue University Research Repository. 10.4231/2E8M-W085 [43]) published online was also used here.

### 2.1 Sample Fabrication

#### 2.1.1 3D Printing

Additively manufactured gypsum samples were fabricated using a ProJet CJP 360 3D printer. Layers (deposition layer thickness  $\approx 100\mu m$ ) of calcium sulfate hemi-hydrate (Figure 2.1 left) were bonded with a proprietary water-based binder (ProJet X60 VisiJet PXL) that produced gypsum as a reaction product (Figure 2.1 center). The orientation of the mineral fabric was controlled by the direction of the application of the binder (red arrow in Figure 2.2b). The binder produced gypsum crystals that bound successive layers of bassanite together. An oriented mineral fabric formed because the gypsum-gypsum bonds between crystals were stronger than the bonds between the gypsum crystals and bassanite powder. The direction of the binder spray head is an input parameter to the 3D printer. The sample geometry was designed in CAD software (i.e. STL format) and then is imported into 3D printer software. Samples with different orientations of bassanite layers relative to gypsum

mineral fabric were 3D printed to examine the effect of fabric direction relative to the bedding layer direction on crack growth under mixed mode loading conditions, and on the geometric properties of the induced fractures. 3D printed samples have been shown to represent natural rocks based on their physical properties (Kong et al., 2018).

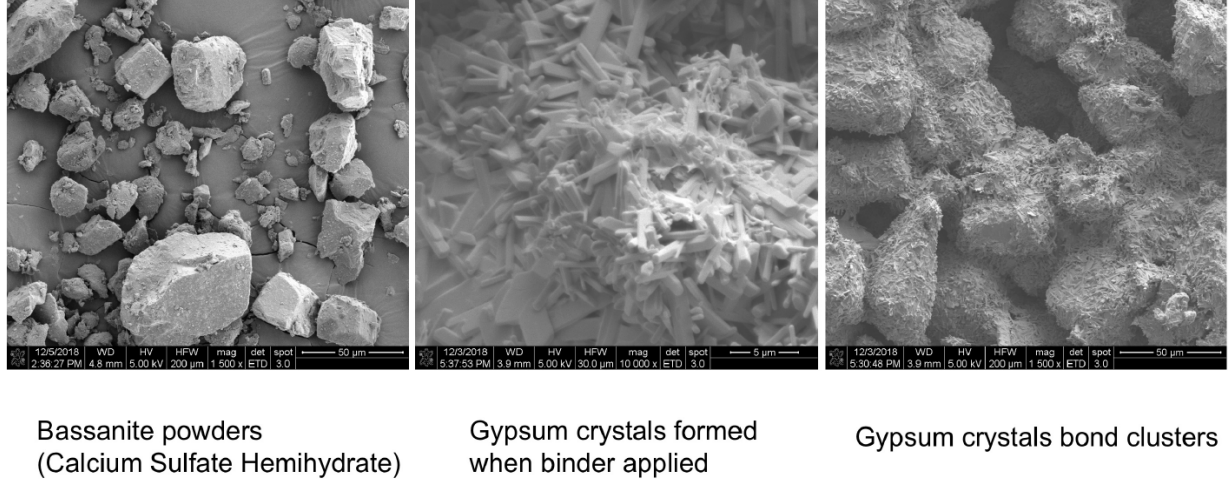


**Figure 2.1.** Scanning Electron Microscopy (SEM) images of (left) bassanite powder, (center) gypsum crystals formed from the binder application, and (right) clusters of gypsum crystals.

### 2.1.2 3D Printed Gypsum Sample Design for 3PB Tests

The dimensions of the samples were  $25.4 \times 76.2 \times 12.7 \text{ mm}^3$ . Figure 2.3 shows a sketch of the samples with the layer orientation given by the blue lines and the orientation of the mineral fabric given by the red lines. Here the samples are referred to as H and Halt for the arrester, VV and VValt for the divider, and Valt and V for the short traverse geometries. In addition to the orientation of the bedding layers and mineral fabric, three different notch locations were tested to compare pure Mode I induced fractures with Mixed Mode I-II induced fractures. The notch was located at either 0 (center of the specimen), or 9.53 mm, or 19.05 mm away from the center of the sample for mixed mode I-II, with the name of the samples given by notch location C, B, or A, respectively (Figure 2.4).

To complete the study of the influences on fracturing from bedding and in-layer mineral fabric orientations of rocks, examination of cases where there is an off-plane shear component,

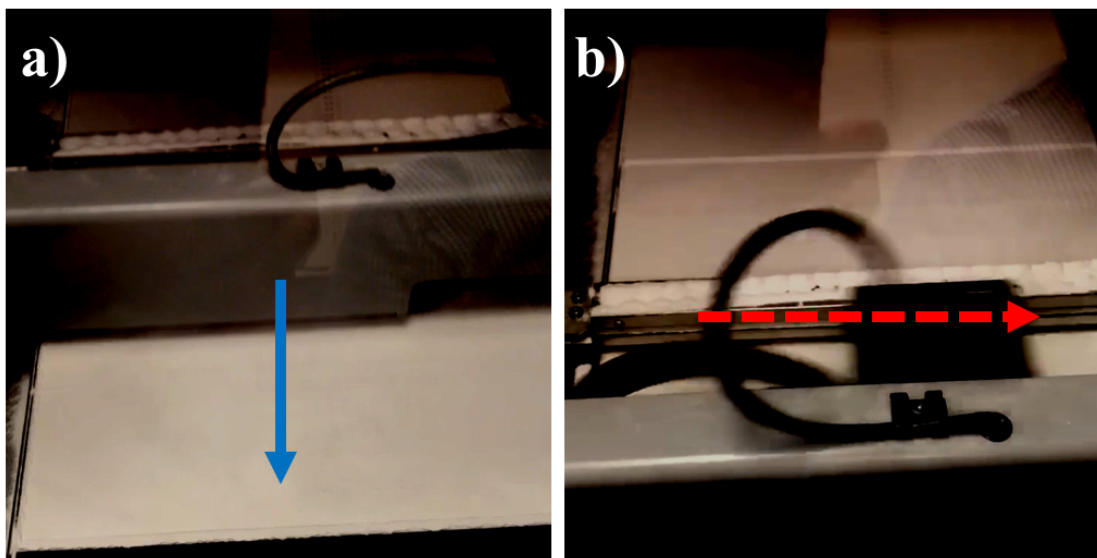


**Figure 2.2.** Depiction of 3D printing process of gypsum samples: (a) deposition of 0.1 mm thick layer of bassanite powder ( $2CaSO_4 \cdot H_2O$ ) on printing area in the blue arrow direction; (b) printer head spreading water-based binder in the direction of the red arrow

which leads to twisting was also examined (Figure 2.5). Here, samples were printed with a notch geometry to promote mixed Mode I and III failure of 3D printed gypsum samples. Mixed Mode I-III loading was achieved by rotating the notch about the the center of the sample (Figure 2.6). For six different sample types with four different notch tilting angles (Figure 2.6), measurements were performed to determine if the failure load, fracture path, and surface roughness differ significantly for anisotropic rock samples when there is only tensile failure versus contributions from both tensile and shear components.

### 2.1.3 3D Printed Gypsum Sample Design for UCS and Brazilian Tests

UCS and Brazilian (split cylinder) tests were conducted to aid quantification of the material properties of the 3D printed samples. To study the compressional and tensile strength of the printed samples,. Figure 2.7 is a sketch of the different sample types that were tested. The 3D printed samples differed in the orientation of the layering and the orientation of the mineral fabric with the layers.

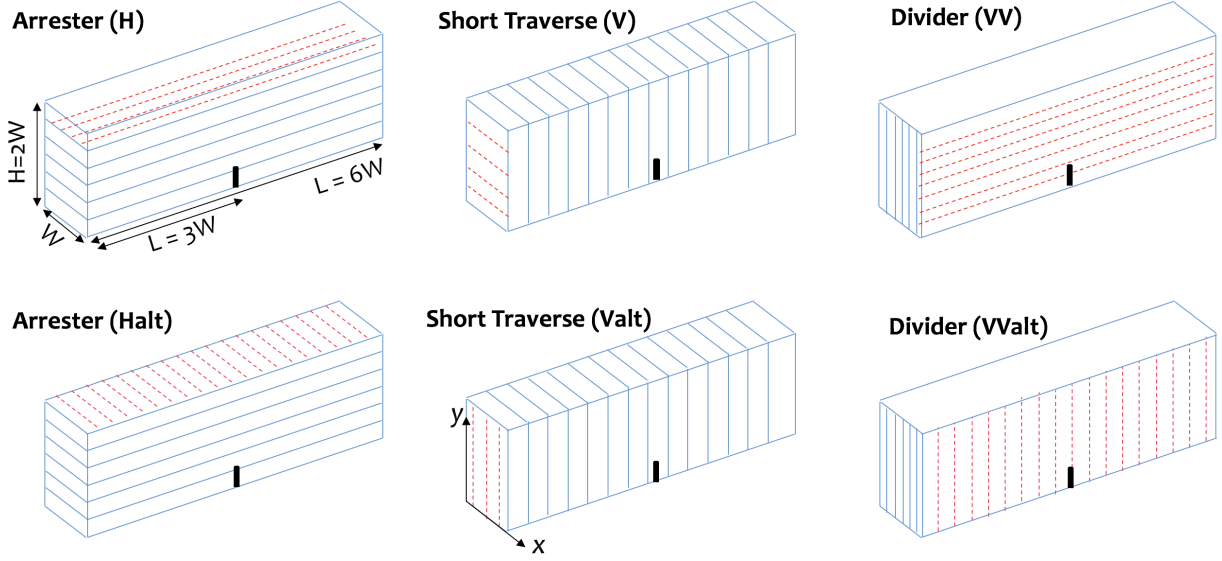


**Figure 2.3.** Nomenclature of layered samples for tensile fracturing (a,b) Arrestor, (c,d) Short Traverse, and (e,f) Divider. Solid blue lines represent layering. Red dashed lines represent binder direction during 3D printing.

## 2.2 Loading Configurations

### 2.2.1 UCS and Brazilian Tests Experimental Setup

Figure 2.8 and Figure 2.9 are the experimental settings for the UCS and Brazilian tests respectively. For the UCS test, a 0.75 inch (19.05 mm) diameter ball was used as a spherical seat. Cylindrical samples were printed that were 25.4 mm in diameter and 50.8 mm in height. For the Brazilian test, the same spherical seat setting was used. A pair of custom-made Brazilian jaws were used for disc-shaped samples (50.8 mm in diameter and 25.4 mm in thickness). The Brazilian jaws (Figure 2.10) are 1.1 inch (27.94 mm) in thickness and 6 inches (152.4 mm) in length. There is a 2 inch (50.8 mm) by 3 inch (76.2 mm) elliptical hole where a 2 inches (50.8 mm) sample is placed during testing. The top of the upper piece (Figure 2.10 a) has a dent in the center for the 0.75 inch (19.05 mm) ball. There are two pins (0.25 inch, 6.35 mm in diameter) on the left and right side that act as guiding pins to ensure that the sample is properly aligned within the system without sliding and torquing from the components. There is a 10 mm gap for vertical displacement. The S-shaped load



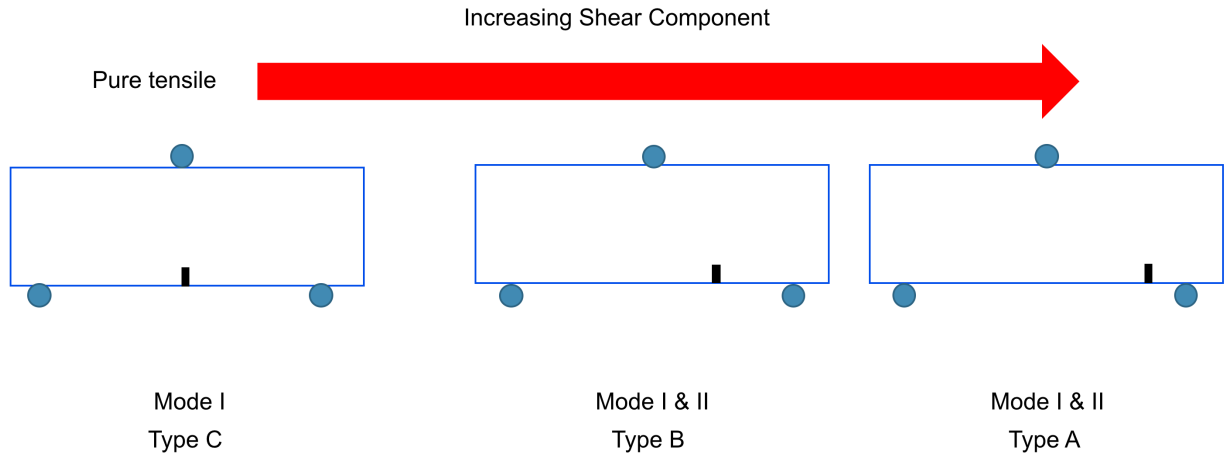


**Figure 2.4.** Moving Notch away from the center to introduce Mode II component

cell has a 2000 lbs (8896 N) load limit. The LVDT is a Omega DG 5mm type LVDT with a linearity of 0.21%. Sampling rate was 10 Hz.

### 2.2.2 Three Point Bending (3PB) Tests

Tensile and shear fractures (Mixed Mode I-II) were induced in the samples using a 3PB test setup (Figures 2.11,2.12). A rod (4.76 mm in radius, 19.05 mm in length) was placed on the top surface at the center of the sample and two rods (same sizes) were placed symmetrically on the bottom surface at a distance of 10% of the sample length (7.6 mm from the ends of the sample). Load was applied to a sample using an ELE International Soil Testing load frame with an OMEGA 1112 N capacity S-shaped load cell. The loading rate was 0.03 mm/min. Load and displacement (from a LVDT) data were recorded at a 10 Hz sampling rate.

### 2.2.3 UCS Test in Xray Machine with Deben

Deben CT5000 microtest stage is a small stress test rig produced by Deben company to perform 3PB, 4PB, tensile or UCS tests inside a 3D Xray microscope. Figure 2.13 shows how applying different jaws on deben stage can be used to perform different type mechanical tests. There are two top pieces, one has the loading length of 0-10 mm while the other one

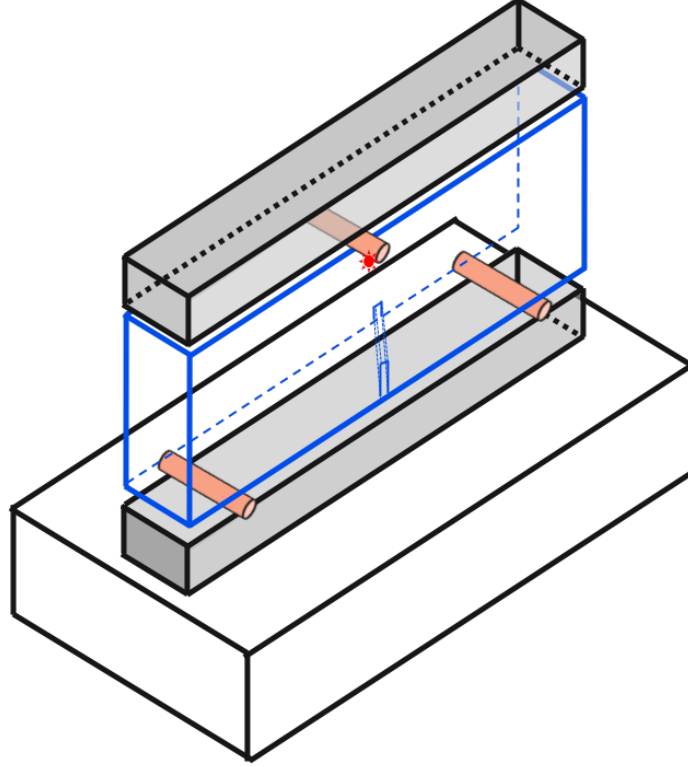


**Figure 2.5.** Sample design for mixed Mode I and III tests

has a 10-20 mm loading length. Figure 2.14 is a projection image of a sample under 3PB tests inside the Xray microscope. A displacement rate of 0.1 mm/min was used and load and displacement data were acquired at 100 millisecond sampling rate. Load cell limit is 5000 N.

## 2.3 Material Properties Measurements

### 2.3.1 XRD of Bassanite Powder and Printed Samples

Samples composed of powder made by crushing a portion of several 3D printed samples were packed in metal sample cups with a sample area 27 mm in width by 2 mm in depth. Powder diffraction (XRD) data were collected on a Panalytical Empyrean X-ray diffractometer equipped with Bragg-Brentano HD optics, a sealed tube copper X-ray source ( $\lambda = 1.54178 \text{ \AA}$ ), soller slits on both the incident and receiving optics sides, and a PixCel3D Medipix detector. The anti-scatter slit ( $1/2^\circ$ ) and divergence slit ( $1/8^\circ$ ) as well as the mask (4mm) were chosen based on sample area and starting  $\theta$  angle. Data were collected between

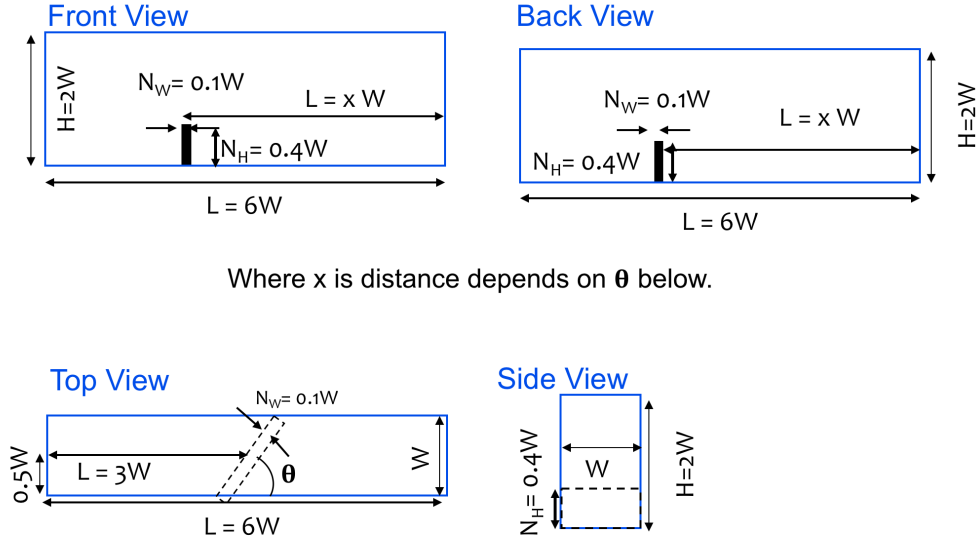


**Figure 2.6.** Sample design for mixed Mode I and III tests with notches tilted at angles of  $60^\circ$ ,  $45^\circ$ ,  $30^\circ$ , and  $20^\circ$

$5^\circ$  and  $90^\circ$  in  $2\theta$  using the Panalytical Data Collector software.1) Search/Match phase identification was performed using the HighScore2) software of Panalytical against the ICDD PDF4+ data base3). Rietveld refinements were performed against the models of the single crystal structure data sets using the *HighScore*<sup>2</sup>) software of Panalytical. Refinement of preferred orientation was included using a spherical harmonics model. The printing powder is mostly bassanite (Figure 2.15) and the printed samples are 51% bassanite and 48% gypsum (Figure 2.16).

### 2.3.2 Seismic Measurements of Sound Speed Through Printed Samples

The average density of the 3D printed geo-architected samples was  $1190 \pm 5.5 \text{ kg/m}^3$ . This was determined from gravimetric measurements and measurements of the sample size. This was performed on 3D printed cubes measuring 50.8 mm x 50.8 mm x 50.8 mm.

Olympus Panametric piezoelectric contact transducers (V-103 and V-153) were used to send and receive ultrasonic (central frequency of 1 MHz) signals through a sample. An Olympus 5077PR pulse generator excited the source with 400V with  $0.4 \mu\text{s}$  width at 100Hz

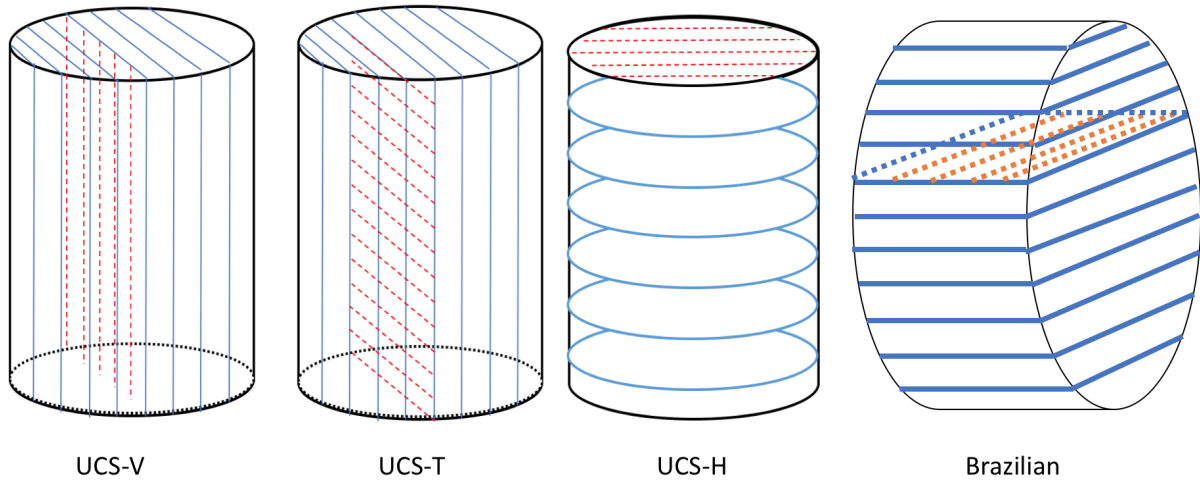


**Figure 2.7.** Sample design for UCS and Brazilian tests

repetition rate. The received signals were digitized using a National Instruments USB-5133 digitizer and stored on a computer for analysis. A sampling rate of 100 MSamples/sec was used to get a bin size of 0.01 microseconds. Tests were conducted on three 2-inch (50.8 mm) 3D printed cubes. The velocities of compression wave P and shear wave polarization SV and SH are shown in Figure 2.17.

### 2.3.3 Mechanical Properties Studied by UCS and Brazilian Tests

3 Brazilian testing and 5 UCS tests were performed. Results shown in Figures 2.21, 2.18, 2.19 and 2.20 demonstrates the relative repeatability of the load-displacement behavior. The H samples produced load-displacement curves that exhibited the ductility of the sample (i.e. flat post peak curves). The V samples (Figure 2.7) exhibited the largest failure load and less ductility after peak load compared to T (Figure 2.7) samples. The data from the Brazilian tests had smaller errors between each test compared to UCS tests. The fractures induced by Brazilian tests were developed very fast and plateaued due to the compression on the top and bottom area contacting the jaws.

## 2.4 Fracture Characteristic Measurements

### 2.4.1 Xray CT

3D X-ray computed microscopy was performed to examine internal structures of the sample. It was conducted on all projects included in the thesis to exam the fracture pattern, study the cracking process, and check the printing conditions. The 3D X-Ray Microscope (Zeiss Xradia 510 Versa) was also used to acquire 2D radiographs for the small geo-architected samples during in-situ 3PB loading test. The small samples were placed in a Deben CT5000 in-situ uniaxial loading device in the 3D X-ray microscope. The loading rate was 0.1 mm/min with load and displacement information recorded at 100 milisecond sampling rate. For Figure 3.2, the settings for both the 2D scans were 80 kV and 7W Xrays, at 4X magnification, with a source and detector distances of 70 mm and 200 mm, respectively, and 4s exposure time for each image with binning setting of 2. The voxel and pixel edge length was 1.75  $\mu\text{m}$ . Figure 4.5 are 2D scans for 3PB tests done under mixed modes. These tests were done with a much bigger field view with lens changed from 4X to 0.4X and explosion time from 4s to 1s, resulting in a resolution of 18  $\mu\text{m}$ . Data reconstructions for 3D structure and anlaysis were performed using Object Research Systems (ORS) Dragonfly Pro 4.0 software. Table 2.1 shows the machine settings for the experiments done to produce those figures of the computed 3D tomography in the thesis.

### 2.4.2 Laser Profilometry

After a sample failed, one of the induced fracture surfaces was scanned using laser profilometry to measure the surface roughness. A Keyence LK-G152 Laser (650 nm wavelength, 120  $\mu\text{m}$  spot size) was fixed to a rail. The sample was mounted on coupled orthogonal translation stages (Newport MTM250PP1) and controlled by a motion controller (Newport Universal Motion Controller ESP 300) to enable measurements of asperity height over a 2D area (10 mm by 20 mm), in increments of 0.1 mm. Figure 2.22 is the view of the setup.

### 2.4.3 Surface Roughness Analysis

The surface roughness maps were corrected for arbitrary rotations associated with mounting the sample in the laser profilometer system. The gradients were determined by fitting a 2D plane to the surface and then subtracting the gradients from the asperity arrays. Next, the minimum asperity height was subtracted from all points to yield asperity heights,  $z(x, y)$  that ranged from zero to the maximum for a given surface.

The isotropy or anisotropy of a surface asperity height distribution was determined from a 2D auto-correlation analysis. In this approach, a 2D Fourier Transform,  $FT$ , of the asperity heights from a surface,  $Z = FT(z(x, y))$ , was multiplied by the complex conjugate,  $\tilde{Z}$ , and then an inverse Fourier transform,  $FT^{-1}$ , was performed on this product:

$$S(x, y) = \frac{FT^{-1}(Z * \tilde{Z})}{\langle z(x, y) * z(x, y) \rangle} \quad (2.1)$$

and divided by the mean of the square of  $z(x, y)$  to obtain  $S(x, y)$ , the 2D auto-correlation function. The 2D asperity map was rectangular in shape which could bias or generate artifacts in  $S(x, y)$ . For each surface roughness map, the auto-correlation function,  $S(x, y)$ , was calculated for 2 circular subregions (10 mm diameter). For each sample type (i.e. 3D printed samples), the presented 2D auto-correlation functions represent an average  $\langle S(x, y) \rangle$ . The auto-correlation function indicates the probability that an asperity at a distance  $r(x, y)$  will have a similar height. The maximum probability is 1 when  $r(x, y) = 0$  when a comparison is made between a point and itself.

Micro-slope angle analysis was also performed on the asperity height map,  $z(x, y)$ , to serve as a measure of the relative smoothness or roughness. Park & Song [44] defined the microslope angle as the dip of the slope between neighboring asperities. A microslope analysis was performed by finding the local slope,  $s$ , where

$$s_x = \frac{dz(x, y)}{dx} \quad (2.2)$$

and

$$s_y = \frac{dz(x, y)}{dy} \quad (2.3)$$

which is the derivative of the surface roughness profile in the x-direction (horizontal and perpendicular to the direction of fracture propagation) and y-direction (vertical direction and parallel to the direction of fracture propagation). The microslope angle is taken relative to the horizontal and is found by

$$\theta_{sx} = \arctan(s_x) \quad (2.4)$$

and

$$\theta_{sy} = \arctan(s_y). \quad (2.5)$$

A surface was defined as relatively smooth if the average microslope angle ( $\theta_{save}$ ) distribution full-width at half the maximum was  $\theta_{save} < 15^\circ$ .

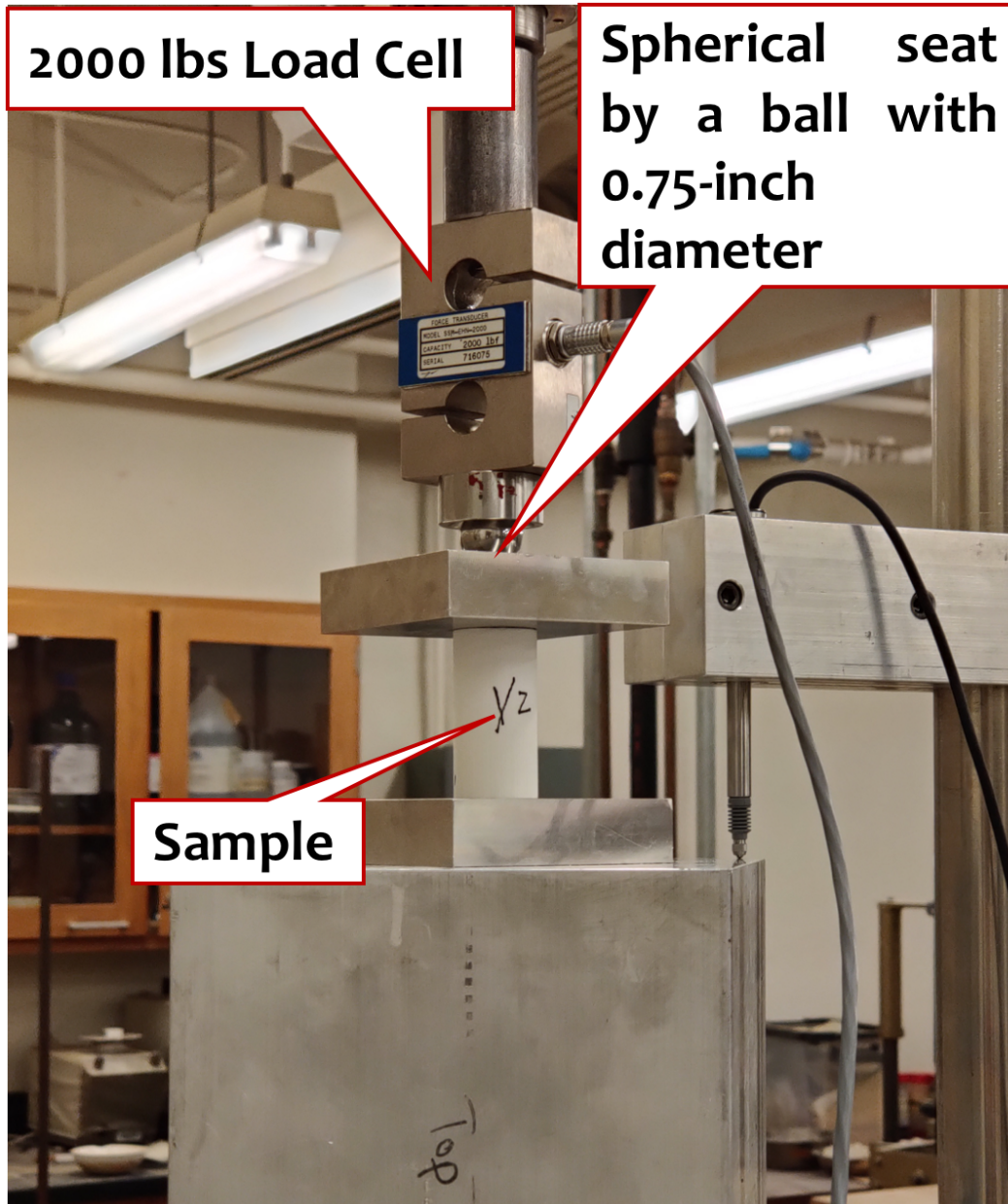
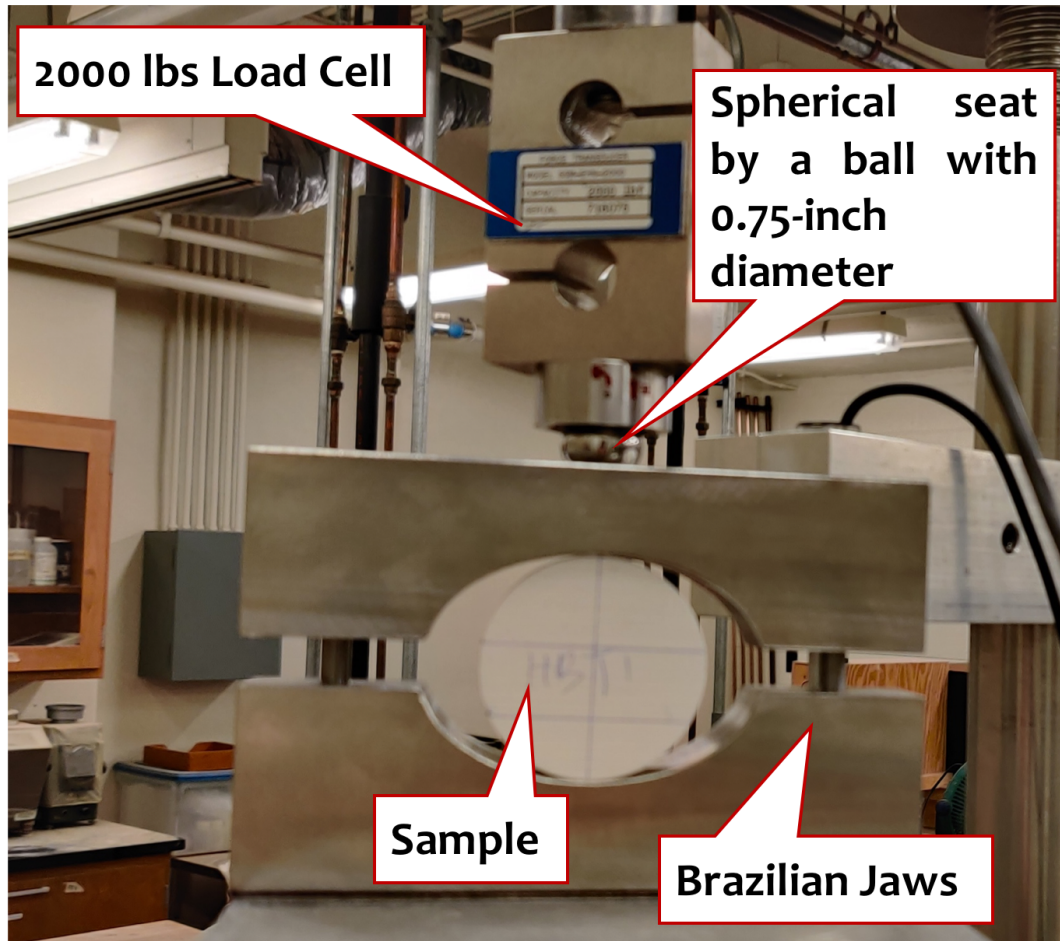
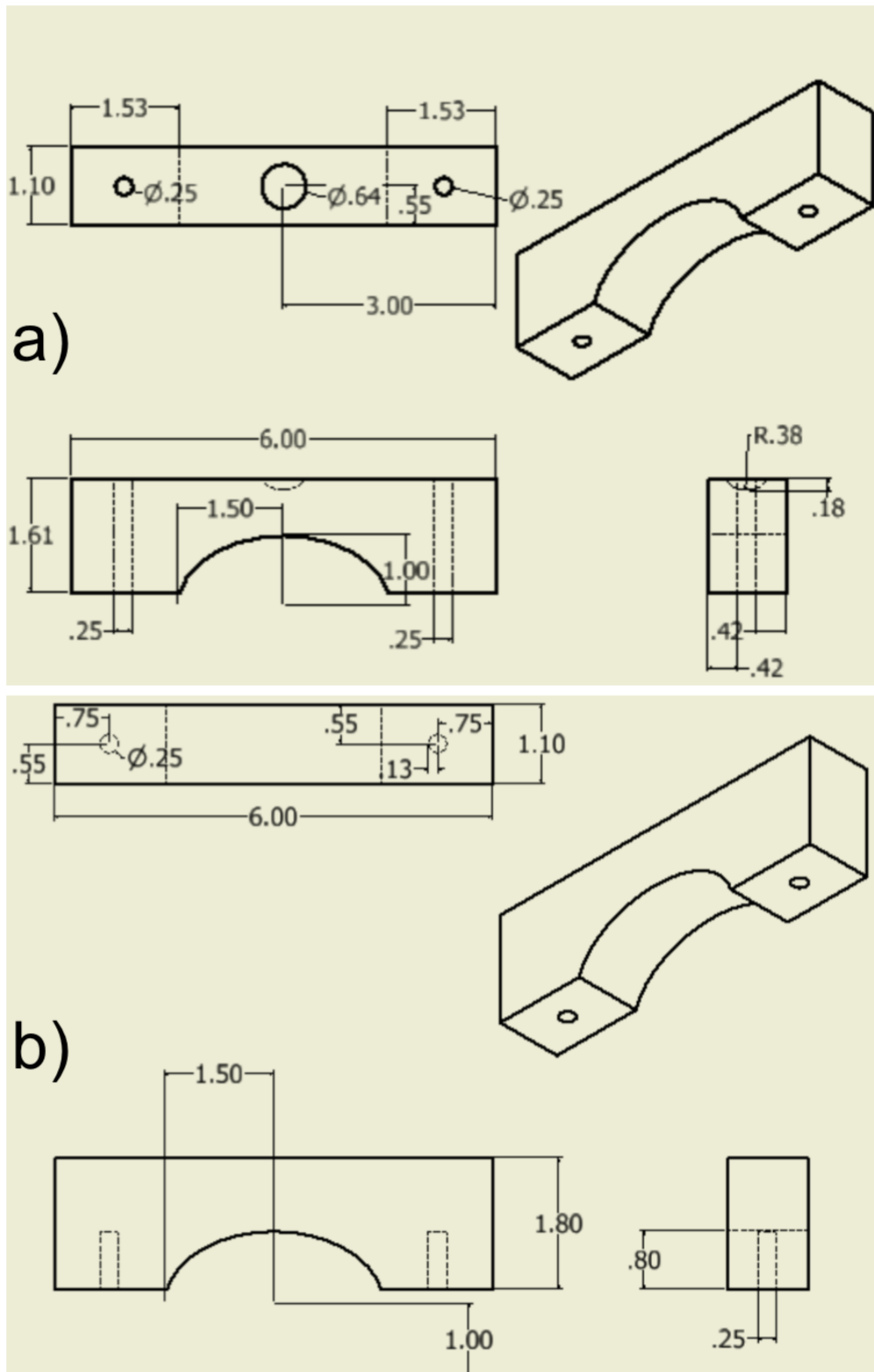


Figure 2.8. Experimental setup of UCS test





**Figure 2.9.** Experimental setup of Brazilian test



**Figure 2.10.** (a) Sketch of Brazilian test top jaw (unit: inch); (b) Sketch of Brazilian test bottom jaw (unit: inch)

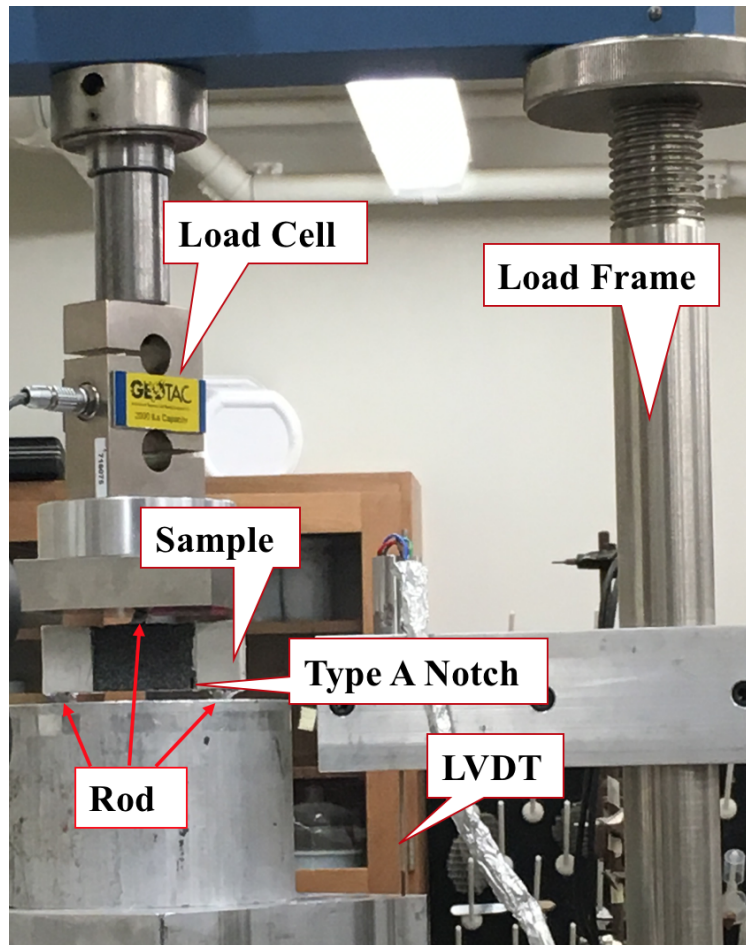


**Figure 2.11.** Experimental setup for 3 point bending (3PB) test

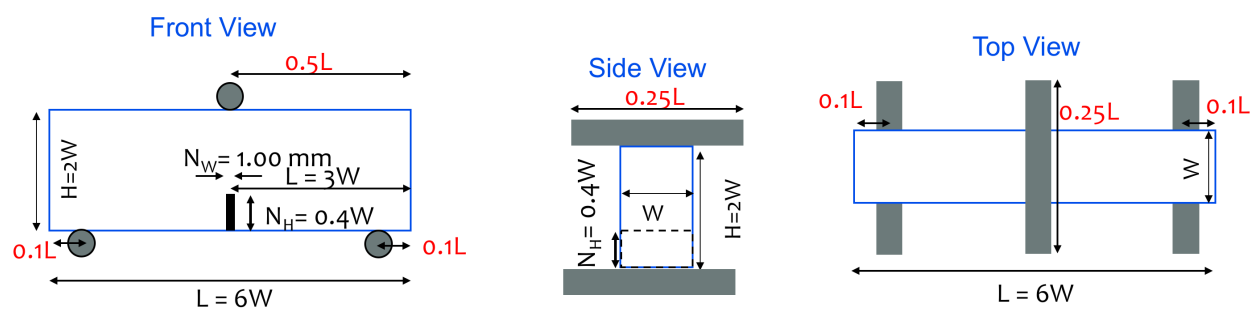


**Figure 2.12.** Sketch of location and dimension of the rods and sample for 3PB tests

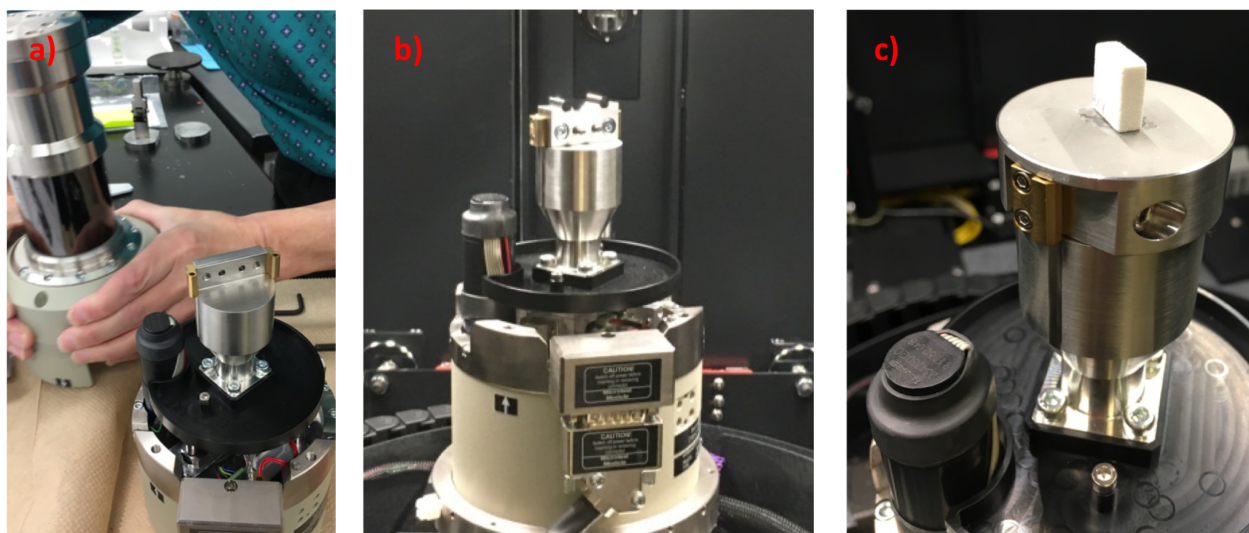


**Figure 2.13.** Figures of Deben stress equipment: (a) the top and bottom pieces to be confined by screws to make a fixed frame; (b) the jaw for 3PB test; (c) the jaw for compressional test.

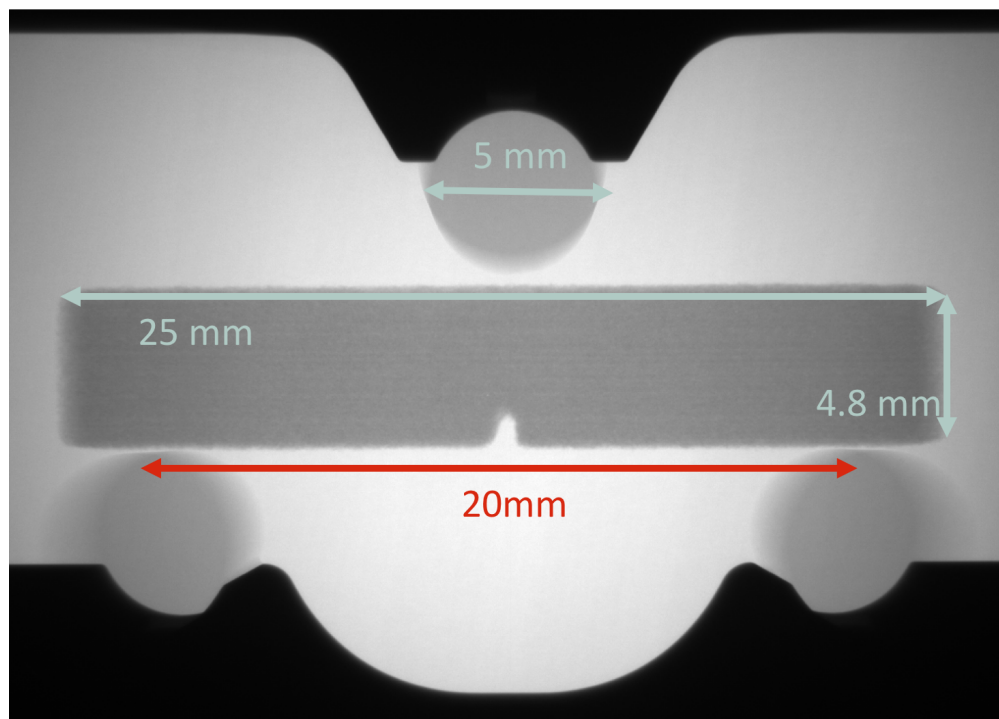


**Figure 2.14.** Scales of the 3PB tests in Xray by Deben tool

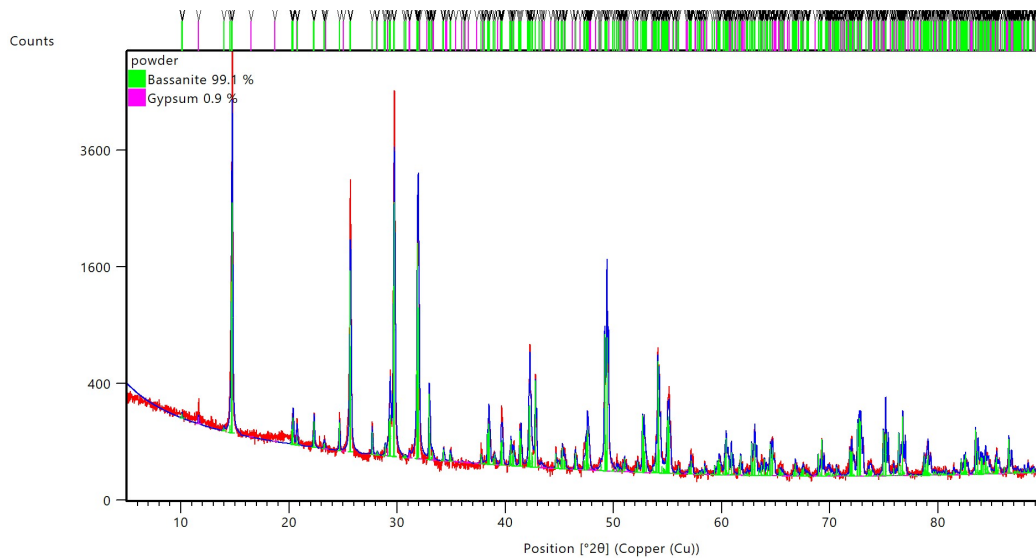


**Figure 2.15.** XRD analysis of printing powder

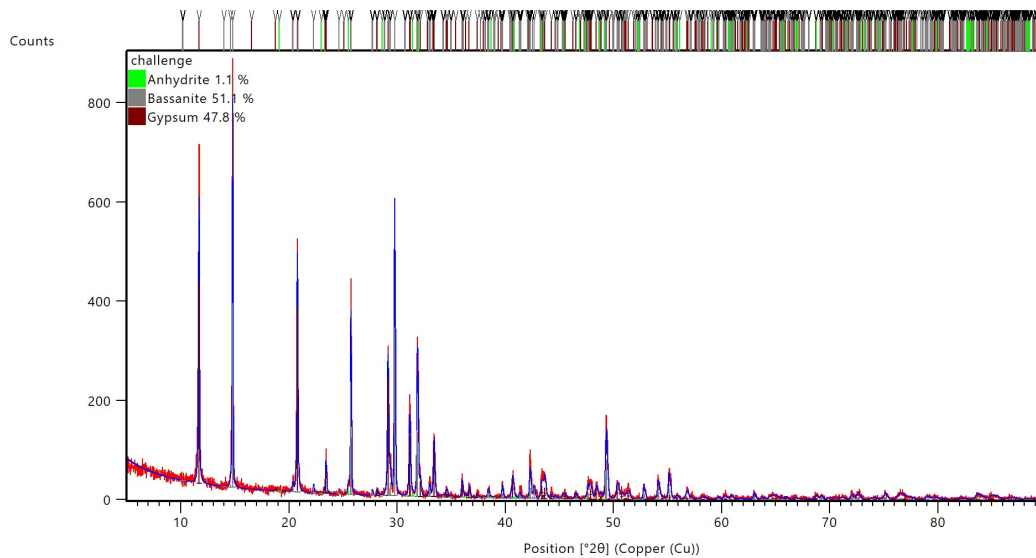


**Figure 2.16.** XRD analysis of printed samples

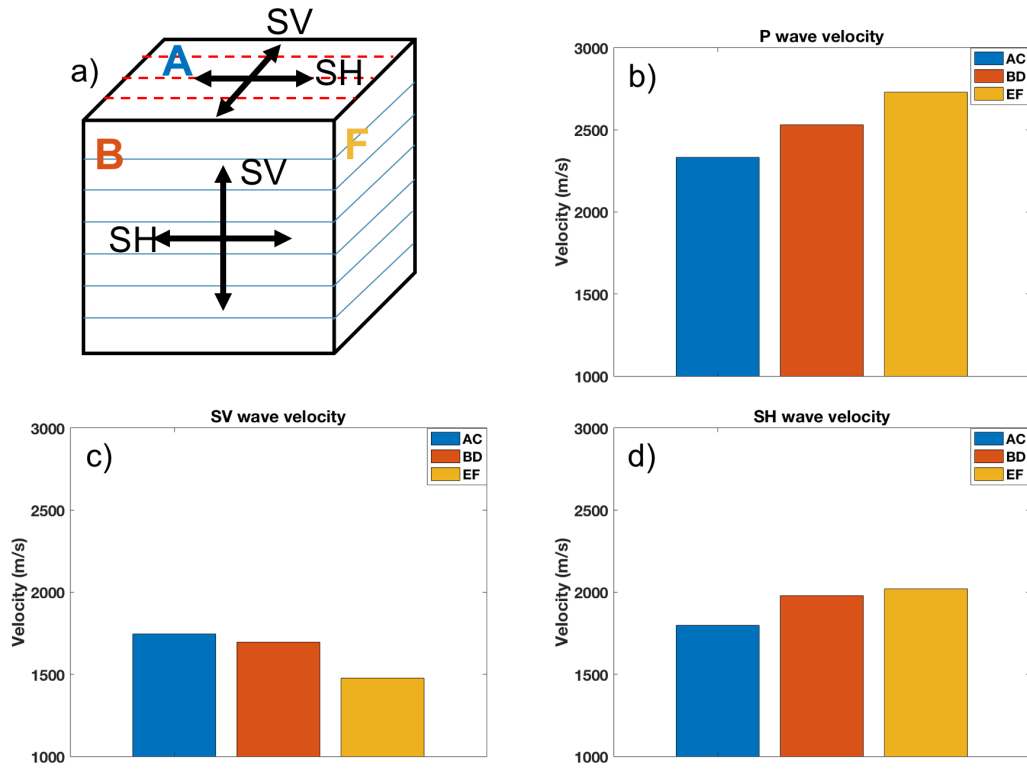


**Figure 2.17.** (a) Sketch of the printed structure of a cube and notation of faces and SV and SH polarizations; (b) Compression wave (P) speed; (c) Shear wave (SV) speed; (d) Shear wave (SH) speed measured by seismic transmissions in three directions

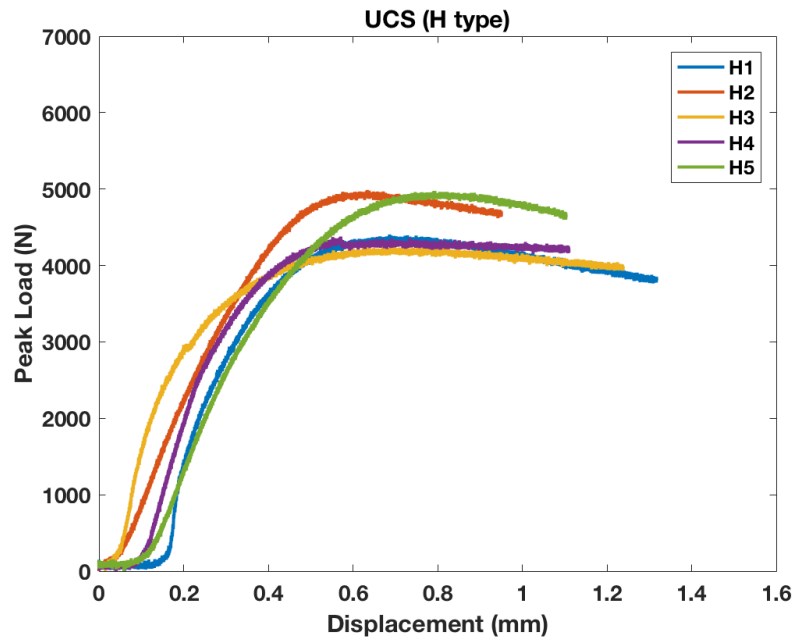


Figure 2.18. Load and displacement curves of UCS tests of type H cylinders

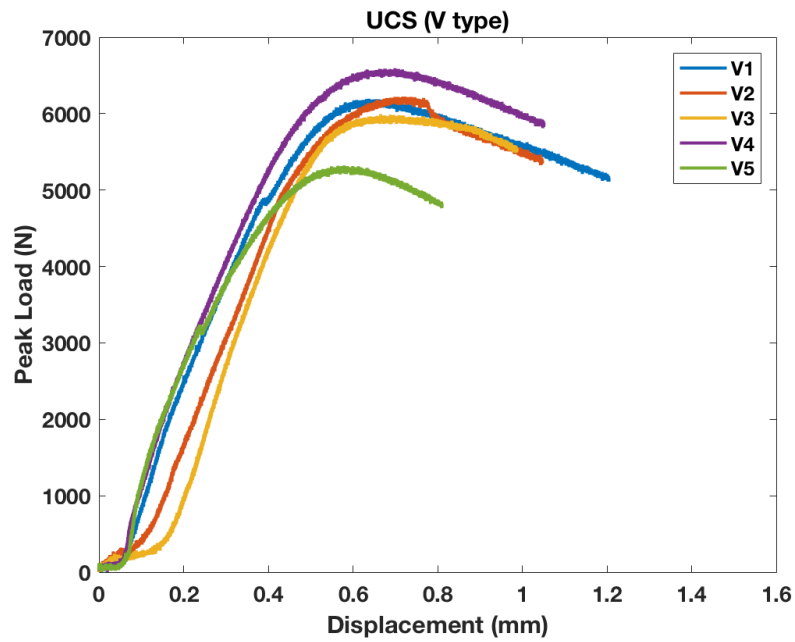
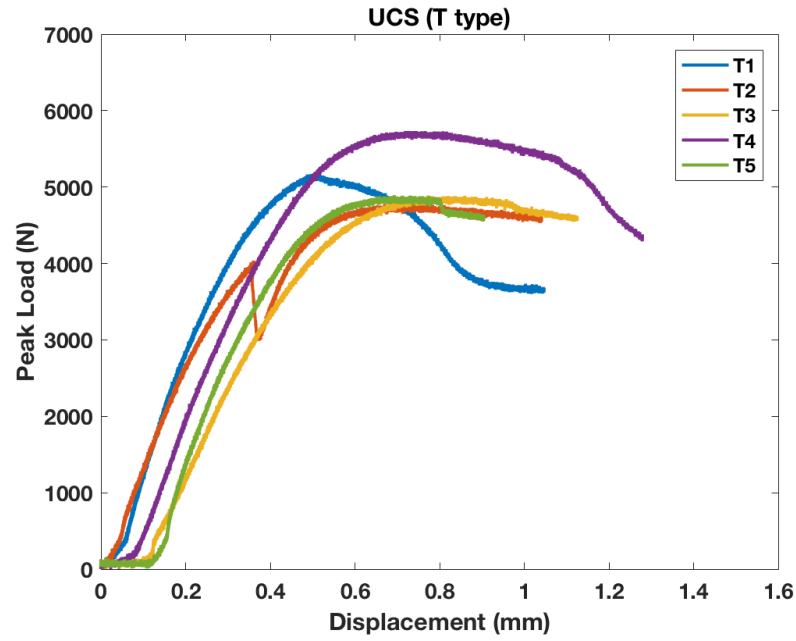
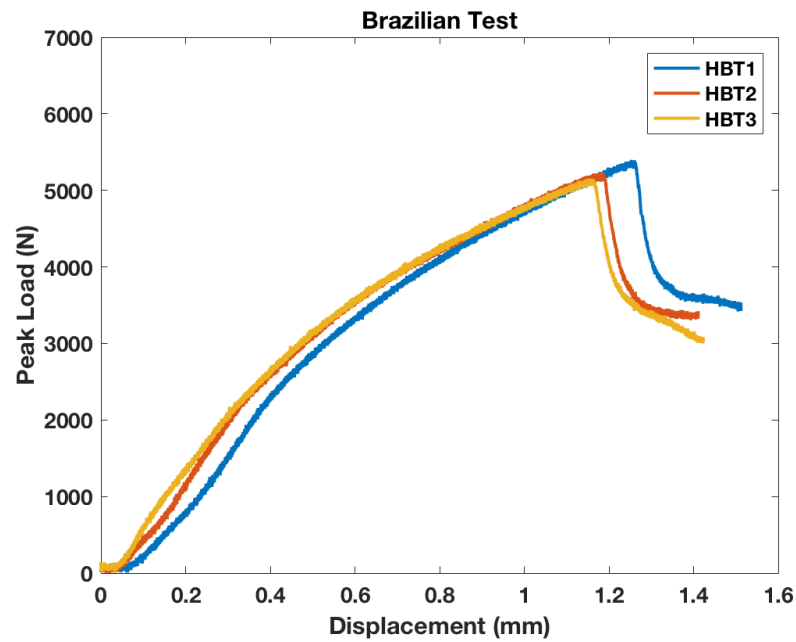


Figure 2.19. Load and displacement curves of UCS tests of type V cylinders





**Figure 2.20.** Load and displacement curves of UCS tests of type T cylinders



**Figure 2.21.** Load and displacement curves of Brazilian tests of cylinders with layers perpendicular to the loading direction



Table 2.1. Xray-CT Settings

Figure	Voltage	Source	Receiver	Lens	Bin	Exposition	Projection	Resolution
Figure 3.6	80 kV	70 mm	300 mm	0.4X	2	1 s	1601	13 $\mu\text{m}$
Figure 4.14, 4.15, 4.16, 4.17	150 kV	200 mm	75 mm	0.4X	1	4 s	3201	25 $\mu\text{m}$
Figure 5.3	160 kV	95 mm	35 mm	0.4X	1	2 s	3201	25 $\mu\text{m}$
Figure 5.6	80 kV	70 mm	300 mm	0.4X	2	1 s	1601	13 $\mu\text{m}$
Figure 6.3, 6.4	80 kV	50 mm	130 mm	0.4X	1	8 s	3201	10 $\mu\text{m}$

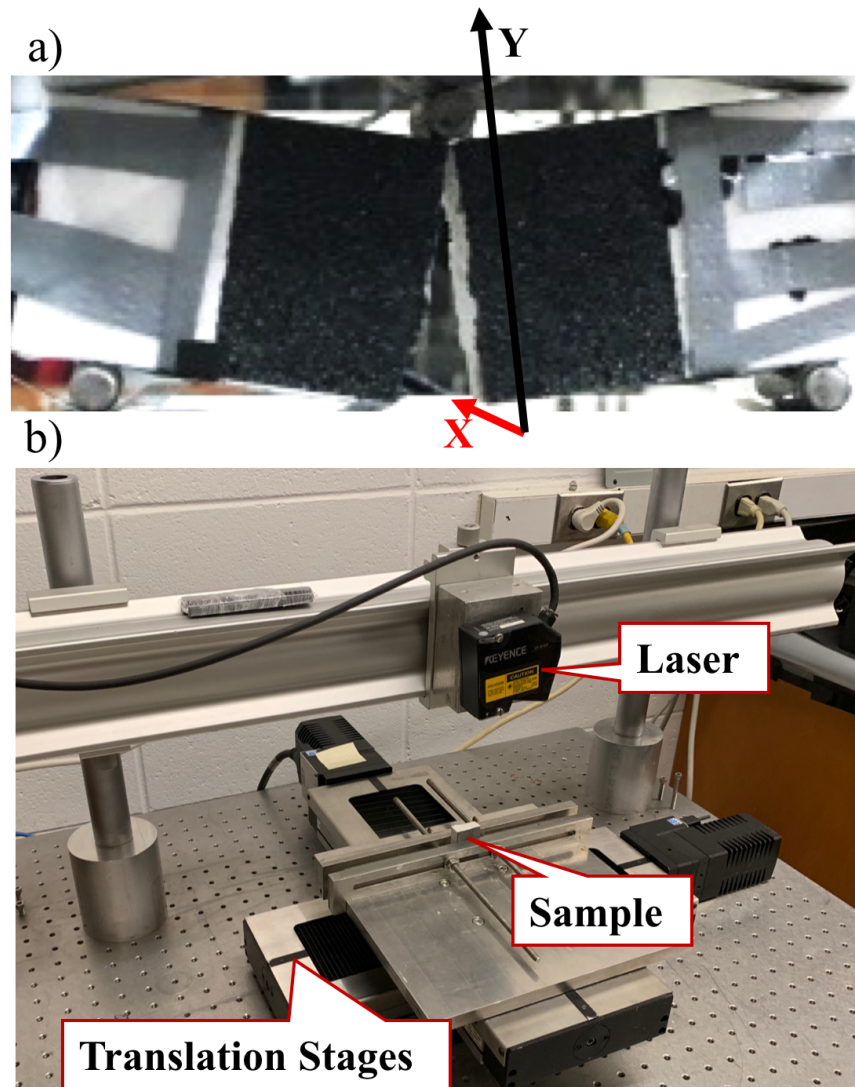


**Figure 2.22.** Surface roughness measurement setup: (a) failed sample and coordinates for the asperity data; (b) laser profilometer setup with a piece of the fracture surface facing up

### 3. EFFECT OF MINERAL TEXTURE ORIENTATION RELATIVE TO LAYERING ON TENSILE FRACTURES (MODE I)

Portions of this chapter are from the paper Jiang, L., Yoon, H., Bobet, A. et al. Mineral Fabric as a Hidden Variable in Fracture Formation in Layered Media. Sci Rep 10, 2260 (2020). <https://doi.org/10.1038/s41598-020-58793-y>, an open access article under the terms of Creative Commons.

#### 3.1 Influence of Mineral Texture on Failure Load

The co-existence of both layers and oriented mineral texture can affect the interpretation of fracturing if the resistance to failure from both or aligned or provide resistance in different directions. Load-displacement curves from a cast gypsum standard sample and geo-architected rock are shown in Figure 3.1a. From the load-displacement data acquired using the methods described in Chapter 2, the peak failure load differed among the geo-architected samples even for samples with the same layer orientation. For example, the peak failure load for arrester samples, H and Halt, differed though both contained layers that were oriented perpendicular to the loading.  $H > Halt$  because the fracture in H had to break across the gypsum crystals in order to propagate. The bonds between gypsum crystals (located between sequential bassanite layers) were stronger than the bonds between the gypsum and bassanite. The weakest geo-architected samples were the short traverse samples, V and Valt (Figure 3.1), both of which contained layers parallel to the direction of fracture propagation.

To confirm that the observed differences in strength arise from mineral texture orientation and are not from variations in the samples, tests were conducted on multiple cohorts of samples. For cast samples, variation in material behavior can arise from impurities, pores and micro cracks [45] while variation in the 3D printed samples usually arises from equipment, printer settings and printer aging factors [46]. To compare the sample strength for the different mineral texture orientations, 3PB tests were performed on samples cohorts that were printed together. The normalized average peak load (Figure 3.1b) was calculated

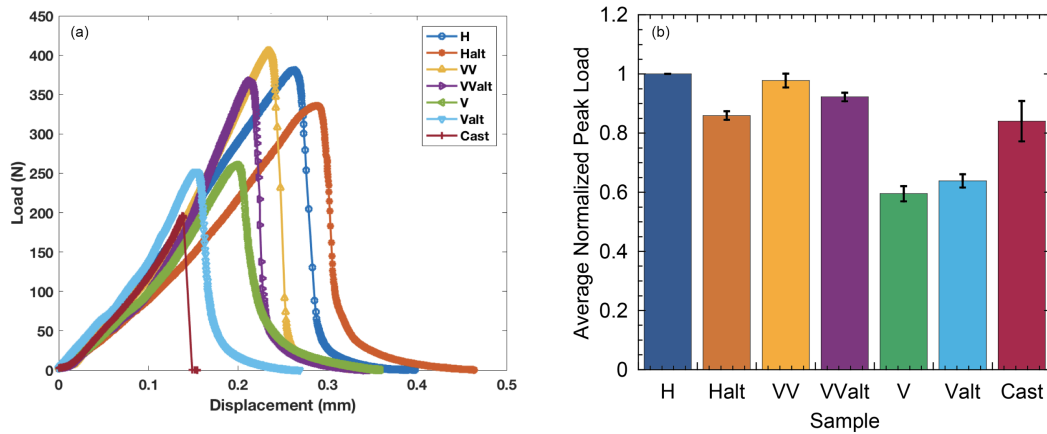


**Figure 3.1.** (a) Load-displacement graph for cast gypsum and representative 3D printed samples. (b) Average relative peak load from 4 cohorts of samples for the cast and geo-architected samples. The samples are color-coded to match the colors in load-displacement curves (values are relative to H samples).

based on data from four separate cohorts each containing the 6 tested geometries (Figure 1) for the 3D printed rocks. For each cohort, the peak load was normalized by the peak load from arrester H, then the average of the 4 cohorts was taken. For cast samples, the average peak strength relative to the arrester H sample is based on data from 12 samples. These results indicate that layer orientation plays a dominant role in sample strength, but layer orientation alone is not sufficient to predict relative resistance to fracturing in layered geologic materials. Prediction requires knowledge of mineral texture orientation, especially in cases where layering and mineral texture may not be aligned. A key question is how the competing anisotropy between layering and mineral texture affects fracture propagation and surface roughness which strongly influences fluid flow through a fracture.

### 3.2 Influence of Mineral Texture on Fracture Surface Roughness

The factors that determine whether an induced tensile fracture is smooth or rough, or whether it exhibits direction-dependent roughness, depends on the relative resistance to failure among the rock constituents and structural features. Both the layering and the mineral texture can cause a fracture to wander or deviate from a straight path, creating a

roughness along the fracture surfaces. For the induced tensile fractures in this study, the fracture propagation path was imaged using 3D X-ray microscopy and laser profilometry (see Methods). The X-ray microscopy provides 2D radiographs and 3D reconstruction of specimens during and post-failure. Comparison of the radiographs (Figure 3.2) for the geo-architected samples indicates that, in general, the fracture trace is relatively straight when fractures are propagated parallel to the layering (e.g. Valt in Figure 3.2f) and deviate from a straight path when propagating across layering (e.g. H and Halt in Figures 3.2a&c). However, the fracture trace for the short traverse sample V is not as straight as that observed for short traverse sample Valt even though they have the same layer orientation. Therefore, the difference in mineral orientation between these two samples affects the propagation path and indicates that mineral texture alters fracture propagation paths.

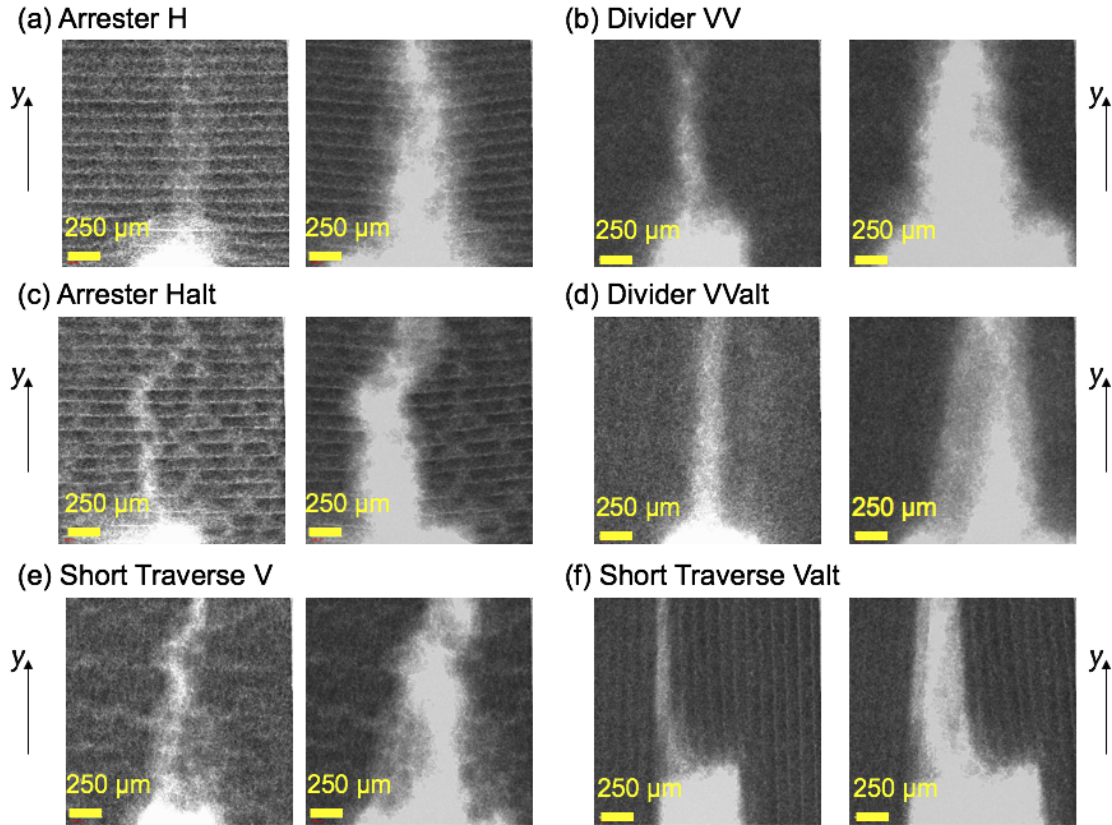


**Figure 3.2.** 2D x-ray radiographs of the small geo-architected samples at 5% of peak load and just prior to complete failure. The direction of fracture propagation from the notch (at the bottom of each image) is in the y-direction. The x-direction is into the page.

Asperity height measurements along the induced tensile fracture surfaces were made to quantify the effect of mineral texture orientation on surface roughness. Microslope (Figure 3.3a) and autocorrelation analyses were applied to data acquired from laser profilometry of the cast gypsum (Figure 3.4) and geo-architected rock (Figure 3.5). Microslope analysis provides a method to quantify relative roughness (smooth:  $\theta_{save} < 15^\circ$ , rough  $\theta_{save} > 15^\circ$ , see Methods), and auto-correlation analysis provides a measure of isotropy or anisotropy in the spatial distribution of asperity heights. Details of the surface analysis approaches are given in the Methods section in Chapter 2.

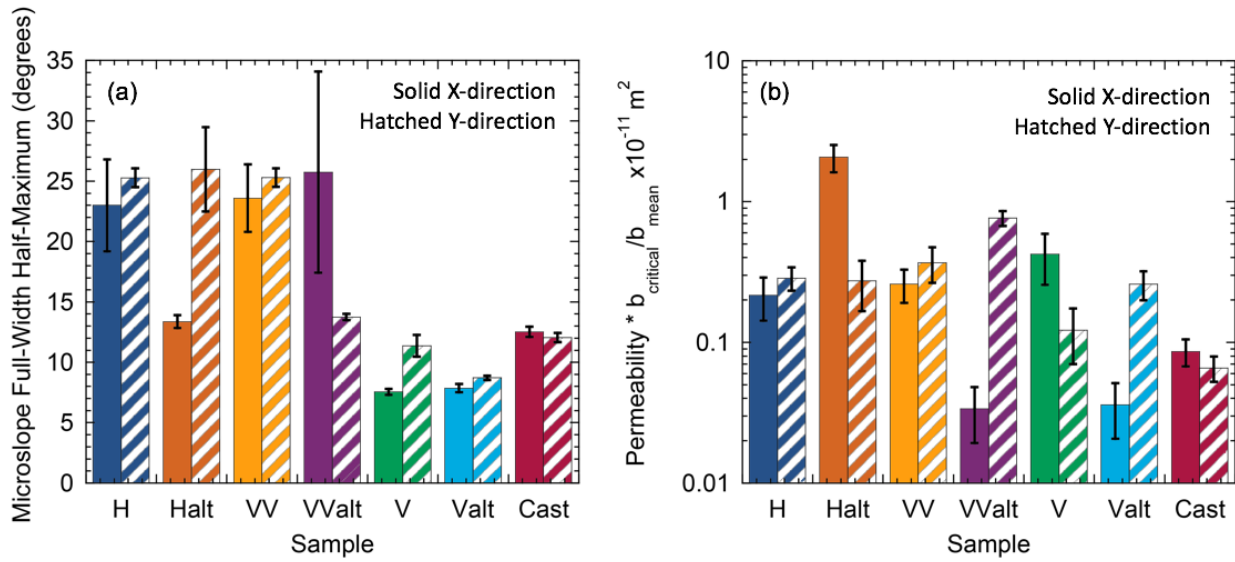


**Figure 3.3.** (a) Average full width - half maximum of the microslope distribution for the cast gypsum and geo-architected samples which are color-coded to match the load-displacement curves in Figure 3.1. (b) Simulated fluid permeability based on surface roughness data from the cast gypsum and geo-architected samples (Figures 3.4 & 3.5). Solid color: in the direction of fracture propagation (*y-direction*); Hatched/shaded Color: in the direction perpendicular to fracture propagation (*x-direction*)

From the microslope analysis (Figure 3.3a), when no layering and a uniform mineral distribution exists, such as in the cast gypsum sample, the surfaces of a tensile fracture are relatively smooth (Figure 3.4). As expected for the short traverse samples (V and Valt), the surfaces were smooth ( $\theta_{save} < 15^\circ$ ) because the fracture propagation path was parallel to the layering, i.e. breaking along the weaker bonds between the gypsum mineral and the



bassanite layers. The difference in the fracture trace observed for samples V and Valt in Figure 3.2 is evident in the microscope analysis where the surface is slightly rougher in the y-direction for V. Direction dependent roughness is also observed for arrester sample Halt and divider sample VValt. The smooth direction ( $\theta_{save} < 15^\circ$ ) in both of these samples is parallel to the mineral texture orientation, while the rough direction ( $\theta_{save} > 15^\circ$ ) occurs as the fracture propagates perpendicular to the mineral texture (y-direction for sample Halt, x-direction for sample Valt). Samples H and VV are rough in both directions because the layers and mineral texture both provide resistance to fracturing but in orthogonal directions. The mineral texture in sample H and VV results in additional roughness in the y- and x-directions, respectively, while the layering produces roughness in the x- and y-directions, respectively.

These results indicate that there is an additional toughness that is associated with the difference in resistance to fracturing between the layering and the mineral fabric. 3D X-ray microscopy was performed to examine this difference. Figure 3.6 contains images from a 3D tomographic reconstruction of sample H after post-peak loading, showing the fracture trace in the y-direction (Figure 3.6a) and the x-direction (Figure 3.6b). In Figure 3.6b, bands of mineral texture are observed, indicating the width of the spray from the binder application that results in the formation of gypsum crystals. The fracture trace in the x-direction exhibits roughness on the scale of the width of the binder spray as the strength and amount of gypsum crystals is less between mineral bands. In Figure 3.6b, the fracture path is observed to wander around the mineral texture, seeking the path of least resistance through the mineral bands. While in (Figure 3.6a), the fracture is observed to deviate from a straight path because of the layering. This observation shows that the competition in resistance to fracturing between the layers and mineral texture affects the roughness of the induced tensile fractures.

Whether an induced tensile fracture exhibits isotropy or anisotropy in surface roughness (Figure 3.5) also depends on both the layering and mineral texture directions relative to the direction of fracture propagation. The fracture surfaces from the cast gypsum sample exhibited isotropic asperity heights (Figure 3.4) because the mineral composition was homogeneous and no layers existed in the sample. However, both isotropic and anisotropic

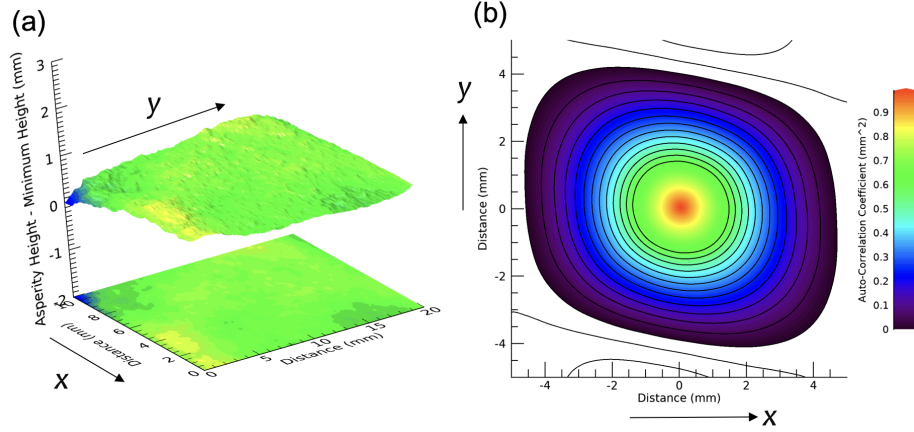


**Figure 3.4.** (a) 3D surface and 2D contour of surface roughness for the cast gypsum sample (y direction is the direction of fracture propagation). (b) Normalized auto-correlation function for the cast gypsum sample.

surface roughness were observed for the geo-architected samples (Figure 3.5). While the weakest samples (short traverse V and Valt) were relatively smooth, the oriented mineral textures resulted in small amplitude corrugations that give rise to stronger spatial correlations in the direction of mineral texture (e.g. x-direction in V Figure 3.5e; y-direction in Valt Figure 3.5f). For the strongest geo-architected samples (H and VV), the surfaces exhibited short-range isotropy as indicated by the nearly circular contour lines because the surfaces were rough both parallel and perpendicular to the direction of fracture propagation, leading to isotropic rough surfaces (Figure 3.5a&b). The strong anisotropy in surface roughness for samples Halt and Valt occurs from the high amplitude corrugations (Figure 3.5 c&d) with valley/ridges in a preferred orientation. These corrugations are on the scale of the mineral texture width (Figure 3.6) and the ridges of the corrugation are aligned parallel to the direction of mineral texture. The strong anisotropy in the asperity height distribution for Halt and VValt occurs because the layers and mineral texture both provide geometric toughening in the same direction, enhancing the roughness.

To summarize, when a propagating fracture does not cross the layers (e.g. V and Valt) the fracture surfaces tend to be smooth and the anisotropy is governed by the mineral texture orientation. If a propagating fracture crosses the layers, the fracture surfaces tend to be rough (e.g. H, Halt, VV and VValt). However, the isotropy/anisotropy of the roughness is



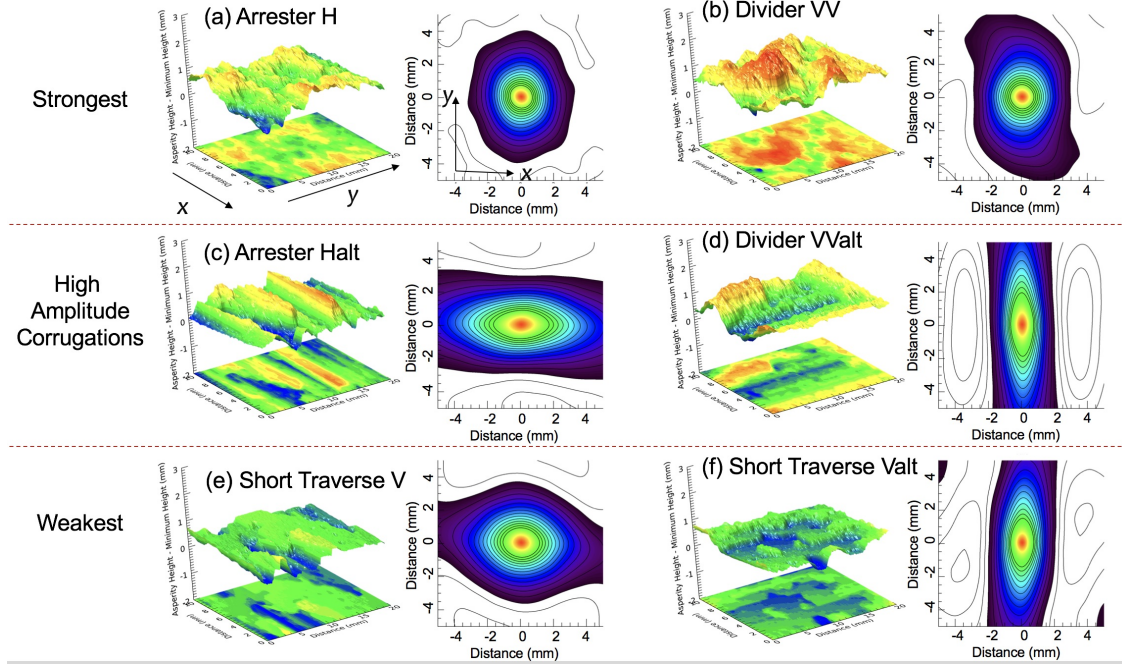


**Figure 3.5.** 3D surface and 2D contour of surface roughness and the normalized 2D autocorrelation function for the geo-architected samples grouped. Note: All axes are the same as those shown in Figure 3.4.

controlled by the mineral texture orientation relative to the layering. If the mineral texture and layer orientations are orthogonal (e.g. H and VV), the fracture surface roughness tends to be isotropic. Conversely, if the mineral texture and layer orientation are aligned (e.g. Halt and VValt), strong anisotropy in surface roughness is observed (Figures 3.3a & 3.5c&d).

Several of the induced tensile fractures in the geo-architected samples had corrugated surfaces. From this study, corrugation in surface roughness was suppressed in the strongest samples (H and V), but enhanced in the intermediate strength when the resistance to fracturing from both the mineral texture and layers were aligned. The weakest samples resulted in the small-amplitude corrugation. Corrugated surfaces often exhibit preferred directions of fluid flow that are parallel to the ridges/valley. Flow perpendicular to the corrugations is expected to be less because of the differences in path length.

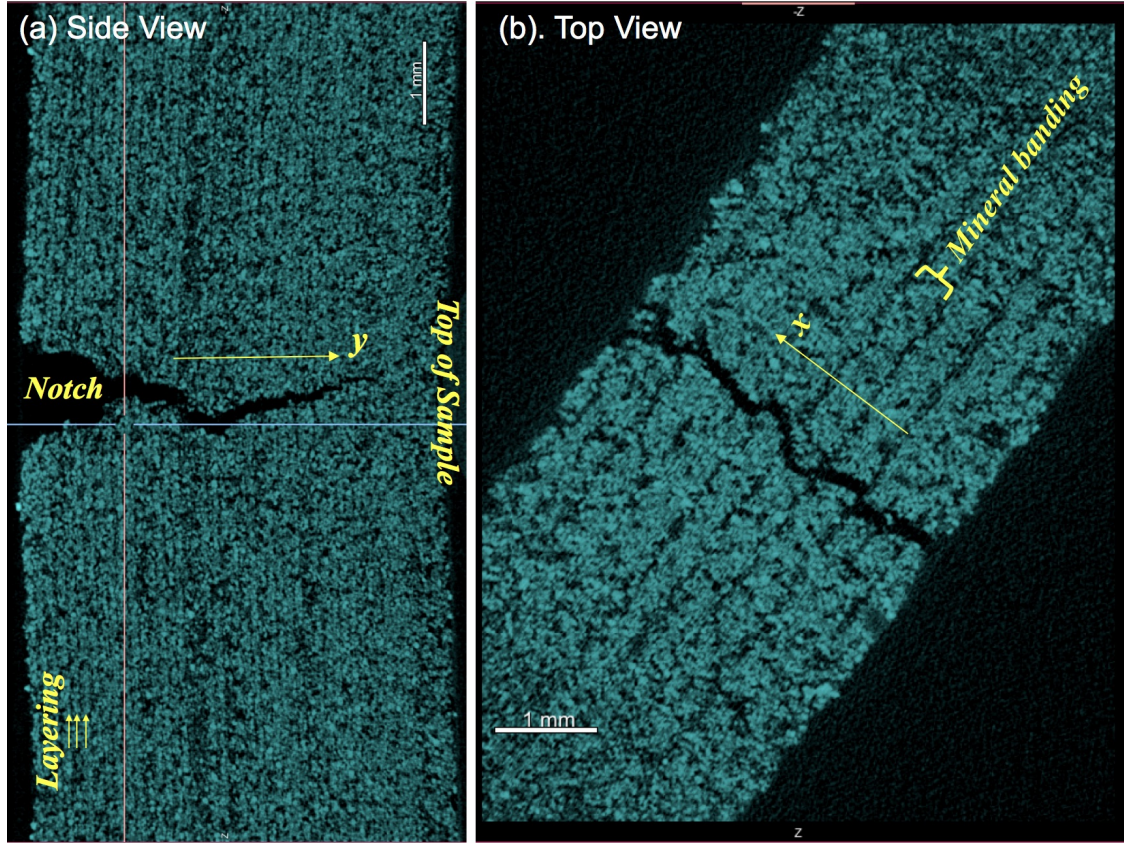


**Figure 3.6.** Image from 3D X-ray tomographic reconstruction of small sample H post-peak showing the fracture trace in the (a) Side view showing the fracture trace in the direction of fracture propagation from notch to top of sample (y-direction) with layer direction indicated by the small yellow arrows. (b) Top view showing the fracture trace in the x-direction and gypsum mineral banding. Scale bars in each image represent 1 mm.

### 3.3 Mineral Texture Controls on Fracture Fluid Flow

Fluid flow through a fracture is intimately related to the roughness of the fracture surfaces and the flow path topology that is formed when the two surfaces are in contact [1], [47]. Simulations of fluid flow were performed using the surface roughness measurements from each sample and the numerical method described in [2], [48]. The roughness from one fracture surface was placed in contact with a flat plane to simulate the flow path topology. A contact area of 5% was selected to reduce the arbitrariness in fracture aperture. Figure 3.3b shows the simulated permeability for two orthogonal directions (parallel and perpendicular to the

direction of fracture propagation) for the tensile fractures that formed in cast gypsum and the geo-architected samples. The permeability is scaled by the ratio of the critical neck (smallest aperture along the dominant flow path) to the mean aperture to account for differences in the size of the apertures among the different samples and between orthogonal directions on the same sample. With this normalization, any variations in flow rate are related to spatial correlations in the aperture distribution [2].

Samples with isotropic surface roughness (cast gypsum, H, VV) exhibited flow rates in the two orthogonal directions that were within 30%. For anisotropic surfaces (V, Valt, Halt and VValt), flow rates varied between the parallel and perpendicular directions of fracture propagation by factors of 4 to 40. For Halt and Valt, the samples exhibiting the strongest corrugations in surface roughness, the permeability is greater parallel to the ridges (y- and x- directions, respectively) than perpendicular to the ridges. The anisotropy observed from the microslope analysis (Figure 3.3a) manifests in permeability anisotropy for the fractures (Figure 3.3b). This finding suggests that estimates of permeability isotropy or anisotropy could be potentially predicted from careful study of mineral texture orientation relative to layering and strength of each feature prior to fracturing a rock.

### 3.4 Conclusions

Geo-architected rock is instrumental in unraveling the complexity and heterogeneity observed in fracture formation in natural rock. Geo-architected rock enabled directional control of mineral texture in layered samples in a repeatable manner. Variability in peak strengths of the geo-architected rock was still observed ( $\approx 10\%$ ) but was less than that observed for natural rock ( $\approx 25\%$ ). From this study, the degree of roughness of a fracture surface was dominated by the orientation of layering relative to the applied load. But the isotropy or anisotropy in roughness was controlled by the relative orientation between the layers and mineral texture along the failure path. These results suggest that detailed mineralogical studies of mineral texture/fabric in laboratory samples is important to unravel failure strength, surface roughness, preferential flow paths, and how fractures propagate in layered geological media.

## 4. EFFECT OF MINERAL TEXTURE ORIENTATION RELATIVE TO LAYERING ON FRACTURES INDUCED BY MIXED MODE LOADING

Portions of this chapter are from from Liyang Jiang’s ARMA conference proceedings with permission from the American Rock Mechanics Association (ARMA) to use material.

### 4.1 Mixed Mode I and II

Depositional, compaction and diagenetic processes all contribute the to the formation of sedimentary rock with layering. In some sedimentary rock, the layers may contain a preferred mineral orientation from interlocked crystals, foliations, or oriented rock fragments. Past research has shown that layers or preferred mineral orientations affect the mechanical properties of rock leading to direction dependent or anisotropic elastic moduli ([5]–[7], [12], [14], [49]–[53]). In previous work by Jiang et al. (2020) [15], tensile fractures (Mode I) toughness and roughness were controlled by the relative orientation between the layering and the in-plane mineral fracture orientation.

For anisotropic rock, research has often focused on fracturing under mode I loading conditions because mode I loading occurs more often and produces the most damage [54]. Here, results are presented from three point bending (3PB) tests with mixed Mode I-II loading of anisotropic 3D printed gypsum rock. Mixed I-II loading is is achieved by moving the notch on the sample away from the center of the sample (Figure 4.1). Measurements were performed to determine if the failure load, fracture path, and surface roughness differed significantly when anisotropic rock samples fractures from both tensile and shear loading, as compared to pure tensile failure (mode I only).

#### 4.1.1 Peak Load

The effect of in-plane mineral fabric on the peak load can be observed by comparing the results from samples H and Halt (Figure 4.1), both of which are arrester samples but with different in-plane mineral fabric directions (Figure 4.2). In H-type samples, both the



layering and mineral fabric provide resistance to failure in the same direction, while in the H-alt sample they provide resistance in orthogonal directions. The results suggest that both the bedding layer and in-layer mineral fabric orientations must be considered when interpreting the resistance to fracturing. Maximum peak loads were observed when both the bedding layers and mineral fabric orientations were perpendicular to the fracture plane (H and VV samples), while smaller peak loads occurred when both the bedding layers and the mineral fabric orientations were parallel to the fracture plane (V and Valt samples). This is similar to what was observed for purely Mode I failure (see Chapter 3) For a given sample type, as the notch moved away from the center, the contribution to failure from mode II loading increased, which resulted in an increase in the peak failure load (e.g. for sample H, by 20% with the notch 19.05 mm away from the center).

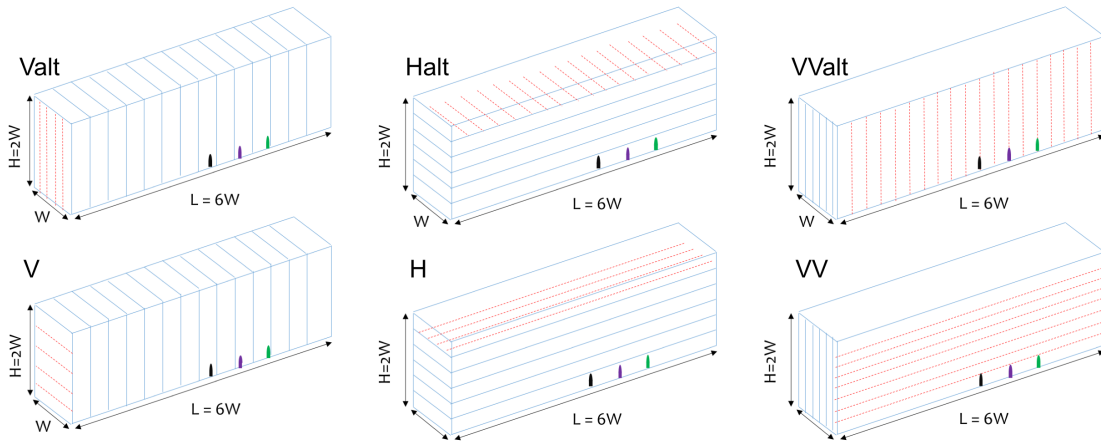


**Figure 4.1.** 3D printed samples for three-point bending tests. The blue lines in the figure show the orientation of the basaltic layers (BL) and the red lines, the orientation of in-plane mineral growth (MG). The location of the notches are denoted by the black, purple or green marks.

#### 4.1.2 Fracture Path

Figures 4.3, 4.4 and 4.5 contain digital images of the induced fractures in samples post failure. The crack path and length, as a function of notch location, were similar for those samples that have the same bedding orientation (H and Halt), irrespective of the orientation of the mineral fabric. The fractures, for both H and Halt samples, initiated at the top of

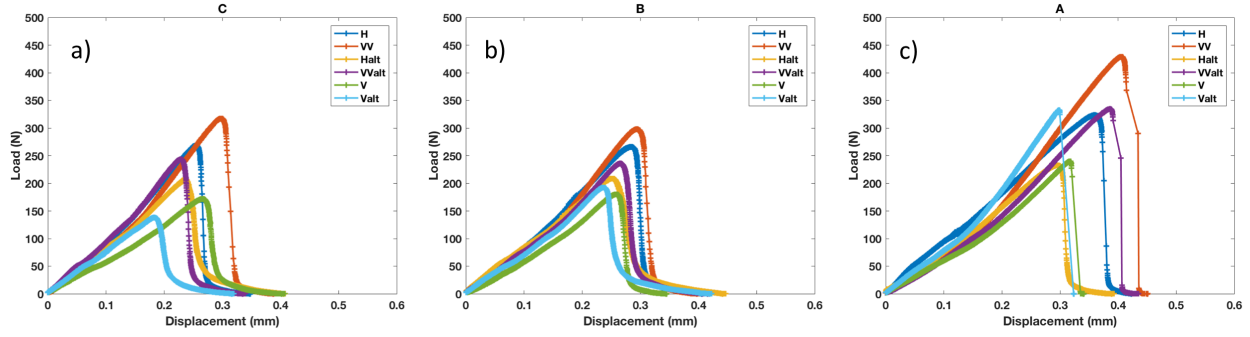


**Figure 4.2.** (a) Load and displacement curves of 3PB tests among 6 sample geometries when the notch is located at the center (type C);(b) when the notch is located 9.53 mm away from the center (type B);(c) when the notch is located 19.05 mm away from the center (type A)

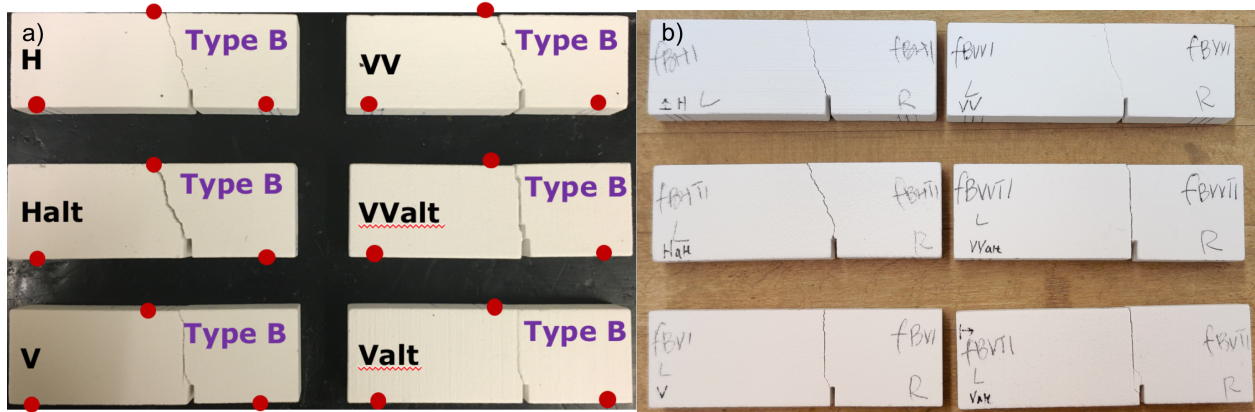


**Figure 4.3.** (a) Fracture paths for a group of samples under Mixed Mode I and II loading (type B);(b) Fracture paths for a group of samples under Mixed Mode I and II loading (type B).

the tip of the notch and propagated towards the center of the sample, where the load was applied. As the notch moved away from the center, the angle between the fracture path and the loading direction increased. However, for the divider samples (VV and VValt), the mineral fabric did affect the crack path. The VV sample had a fracture path similar to the H sample, which is an angled crack, but the VValt sample fracture path tended to be parallel to the loading direction and not associated with the notch. The same occurred for the V and Valt samples where the fracture path was parallel to the loading direction and to the layering, regardless of notch location. For type A samples, where the notch was located the

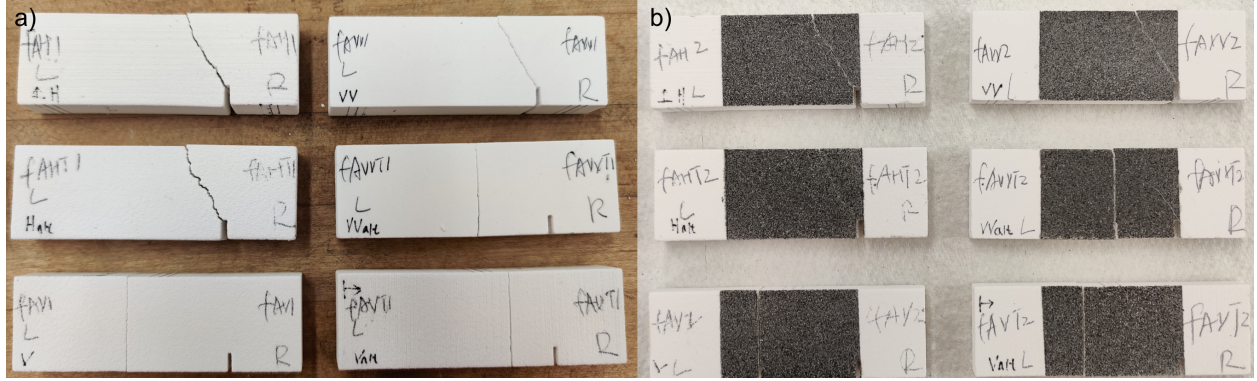


**Figure 4.4.** (a) Fracture paths for a group of samples under Mixed Mode I and II loading (type A);(b) Fracture paths for another group of samples under Mixed Mode I and II loading (type A).

farthest from the center, some of the fractures (V, Valt and VValt) did not initiate at the tip of the notch (Figure 4.4). This suggests that the bedding strength was low such that failure occurred first in the material rather than at the tip of the crack.

#### 4.1.3 Fracture Roughness

The factors that determine whether an induced tensile fracture is smooth or rough, or whether it exhibits direction-dependent roughness depend on the relative resistance to failure among the rock constituents and structural features. Both the layering and the mineral fabric can cause a fracture to wander or deviate from a straight path, creating roughness along the fracture surfaces.

Laser profilometry was performed on the surface of all the fractures induced from the tests. The surface roughness maps were corrected for any rotations due to mounting the samples on the laser profilometer. Micro-slope angles [15] were calculated from the surface maps by finding the local gradient in both the x and y directions. Figures 4.6, 4.7, 4.8, 4.9, 4.10, and 4.11 are the micro-slope angles in the x and y directions taken from representative samples. The angles were repeatable within  $2^\circ$ . Based on this, the full width half maximum (FWHM) is essentially the same for all the different notch locations for a given sample geometry, i.e. layering and mineral fabric orientations (Table 4.1). A  $\pm 15\%$  deviation in FWHM values were observed from the samples of the same type and with the same notch

location. When both the bedding layers and mineral fabric orientations were perpendicular to the loading, the fracture surface roughness had the same microslope distribution in the x and y-directions (Figures 4.6 and 4.10), while in all other cases a the microslope distribution differed between these two orthogonal directions, with a smoother roughness (narrower distribution in Figures 4.6 and 4.10) in the direction parallel to the direction of the mineral fabric. Thus, whether the fracture roughness of a sample was isotropic or anisotropic was not determined by the notch location. Essentially increase the shear contribution to failure did not affect fracture surface roughness,

**Table 4.1.** Full width half maximum (FWHM) values of the micro slope distributions in both X and Y directions from the fracture surfaces formed with different bedding layer and mineral growth directions and different notch locations (samples type A, B, C).

Sample (Figure 4.1)	X axis			Y axis		
	C	B	A	C	B	A
H	27°	31°	35°	23°	31°	27°
Halt	9°	13°	15°	29°	42°	30°
VV	26°	30°	34°	25°	27°	24°
VValt	39°	56°	36°	12°	17°	12°
V	5°	6°	4°	8°	7°	5°
Valt	5°	8°	6°	7°	8°	5°

#### 4.1.4 Conclusion

3D printed rock is instrumental in helping to in unravel the complexity and heterogeneity observed in fracture formation in natural rocks. It enables directional control of the in-layer mineral fabric and layering in a repeatable manner. Compared to the results from previous work [15], [39] that found that differences in failure load and fracture roughness for layered rock are affected by both the layer and mineral fabric orientations, this work has discovered that the fracture path is influenced by the bedding and mineral fabric directions, when mode II loading is introduced. However, the surface roughness attributes (isotropy/anisotropy and smoothness/roughness) are similar to those found previously from pure Mode I loading. In the next section, fracture formation under mixed mode I and III



loading is presented. The results from mixed mode I-II suggest that detailed mineralogical studies of mineral texture/fabric in laboratory or core samples is important to unravel failure strength, surface roughness, and how fractures propagate in layered geological media. With this information, we have the potential to predict preferential flow paths in anisotropic fractures based on microscopic inspection of mineral texture orientation relative to layering, and the mode of failure, which are vital to induced fracturing for geothermal and  $CO_2$  sequestration applications.

## 4.2 Mixed Mode I and III

### 4.2.1 Fracture Path

A comparison of the fracture path in cast gypsum and 3D printed gypsum samples under mixed Mode I and III loading are shown in Figure 4.12 and Figure 4.13. The cast gypsum samples were made in a mold with notches rotated about the center of the sample, the same as the notches in the 3D printed samples. The fractures are observed to initiate from the tip of the notch and moved smoothly to the center of the top face where the central loading rod was located. For cast gypsum cases with  $\theta = 30^\circ$  and  $\theta = 20^\circ$ , the fractures did not twist (Figure 4.12). For the 3D printed samples, the type H geometry was used (Figure 4.13) to determine the effect of out of plane shear on the fracture path and surface roughness, particularly the corrugations along the surfaces. The fractures were initiated from the tip of the notch and quickly curved towards the center of the sample and then propagated through the rest of the sample in a manner similar to Mode I case (Figure 4.13). For the  $\theta = 20^\circ$  case, there were more than one fracture induced that had different paths between the front and back of two samples.

### 4.2.2 Fracture Roughness

Here, the fracture surface roughness is examined for the 6 sample geometries (see Figure 2.6) with 4 notch angles using 3D Xray CT computed tomography. The 3D X-Ray Microscope (Zeiss Xradia 510 Versa) was used to perform 3D computed tomography for induced fractures after 3PB loading test. The settings for 3D X-ray scans were 150 kV and 10 W

Xrays, at 0.4x magnification, with a source and detector distances of 200 mm and 75 mm, respectively, 4 s exposure time and camera binning of 1 setting for each of the 3201 projections. The voxel and pixel edge length were 25  $\mu\text{m}$ . Data reconstructions and analysis were performed using Object Research Systems (ORS) Dragonfly Pro 4.0 software (figures 4.14, 4.15, 4.16, and 4.17).

When the notch is rotated a small amount ( $\theta = 60^\circ$ ) (Figure 4.14), only a small portion of the fracture path twisted. The untwisted portions of the fracture surfaces were observed to be similar to those from the pure Mode I case. For the case where  $\theta = 45^\circ$ , the twisting of the fracture surface is more obvious (Figure 4.15). At  $\theta = 30^\circ$ , for V and Valt samples, the vertical bedding affected the fracturing, resulting in fractures were that exhibited more whole plane twisting (figure 4.16). The surface geometry is more complicated when the notch was rotated to  $\theta = 20^\circ$ . We can see that there are more than one fracture plane in the Halt case (Figure 4.17).

### 4.2.3 Conclusion

As the notch rotates away from the long axis of the notch, the contribution to failure from the Mode III component increases, which leads to an increase in the area of the region of twisting and to a smaller region that exhibits pure Mode I behavior. The local properties of the fracture surfaces remained the same when Mode II or Mode III components were added. The bedding and in-layer mineral fabric orientations controls the small scale properties of the fracture surface. The general shape of the fracture also depends on the bedding and in-layer mineral fabric relative orientation. Most of the time, the mixed Mode I-III case demonstrated a surface that twisted from the angle of the printed notch to the mode I tensile fracture condition when the fracture propagated from the top of the notch to the top of the sample. In addition, when the notch was off-centered (like type A) which experienced both mode I and II stresses, there was significant non-Mode I components. For samples V and Valt under mixed Mode I-II and Mode I-III loading, the sample did not fail as expected, i.e. a crack path initiated from the notch tip to the centered rod. Instead, failure occurred away from the notch. The failure in samples V and V alt was dominated by failure along the

layering. This resulted in planar fractures with roughness governed by the orientation of the mineral fabric, and no twisting of the failure plane like that observed in the other samples. The V and Valt for all loading conditions are the weakest samples.

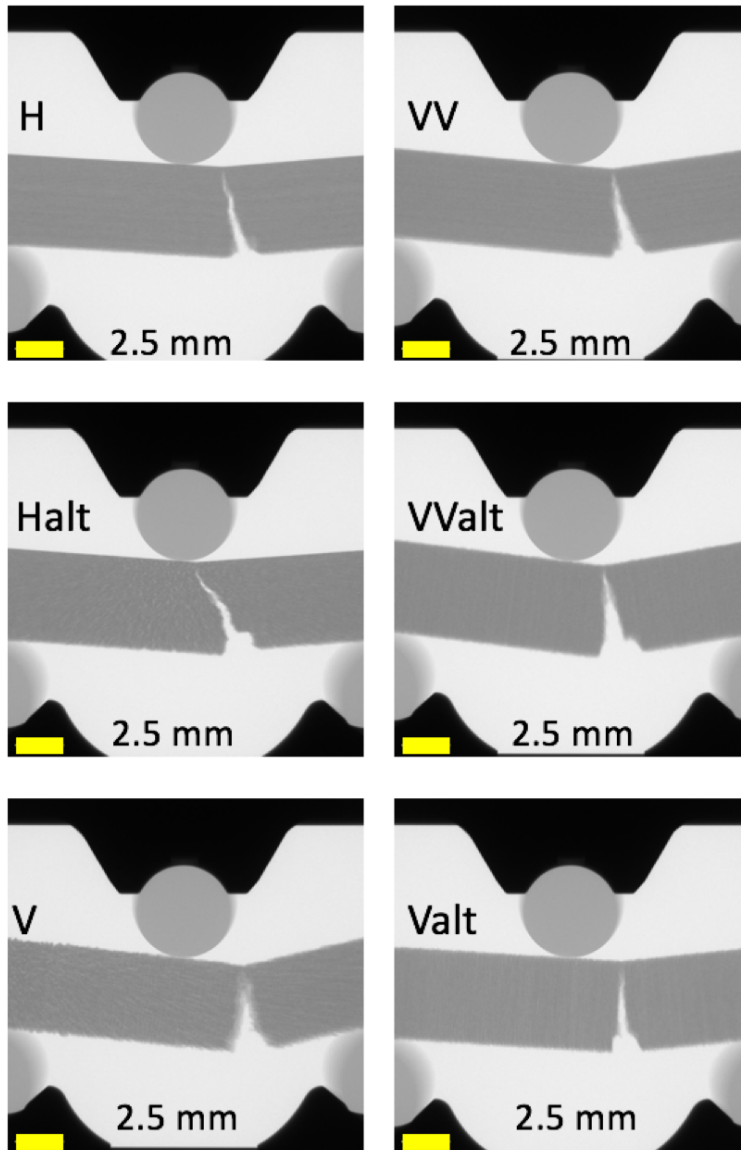


**Figure 4.5.** Fracture paths for a group of samples under Mixed Mode I and II loading (type B) in Deben with 2D Xray projection shown similar results as the Figure [4.3](#)

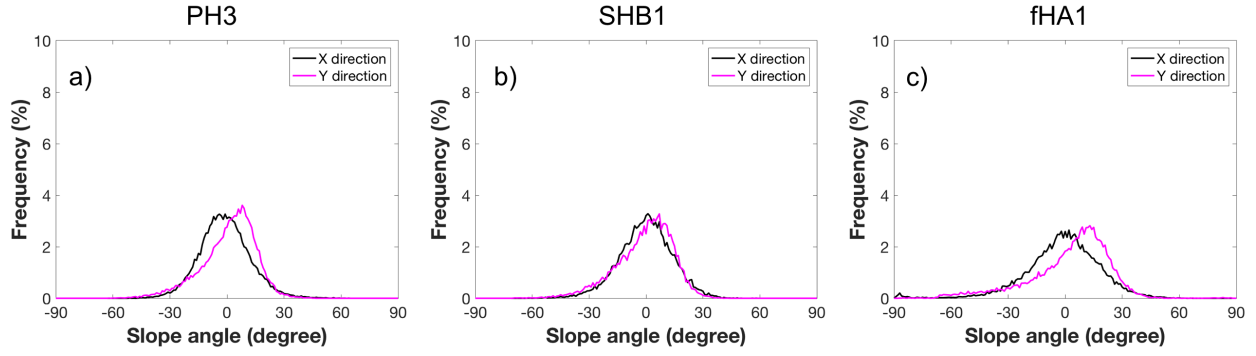


**Figure 4.6.** (a) Micro-slope angle distributions in the loading direction (Y) and sample thickness direction (X) of H samples' fractures under loading type C; (b) type B; (c) type A

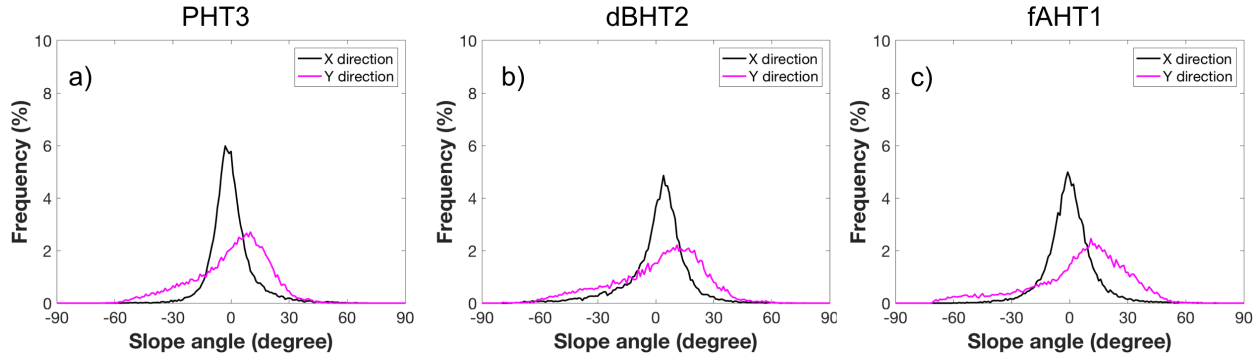


**Figure 4.7.** (a) Micro-slope angle distributions in the loading direction (Y) and sample thickness direction (X) of Halt samples' fractures under loading type C; (b) type B; (c) type A

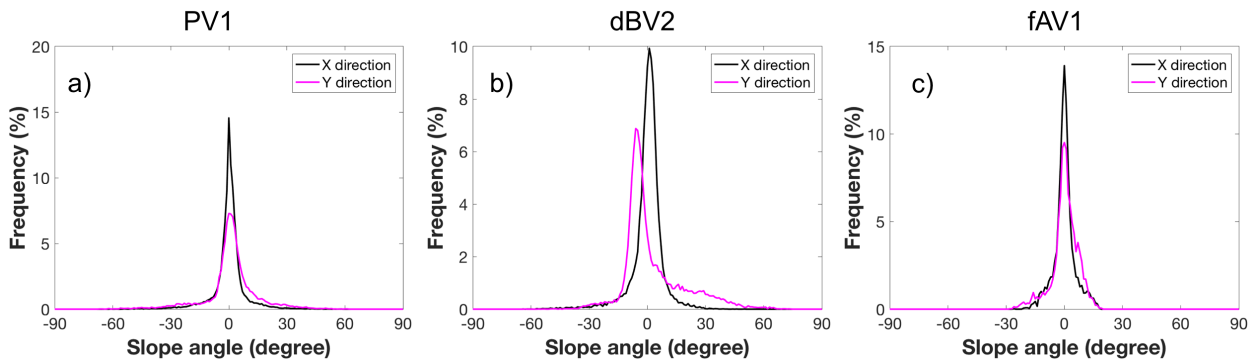


**Figure 4.8.** (a) Micro-slope angle distributions in the loading direction (Y) and sample thickness direction (X) of V samples' fractures under loading type C; (b) type B; (c) type A

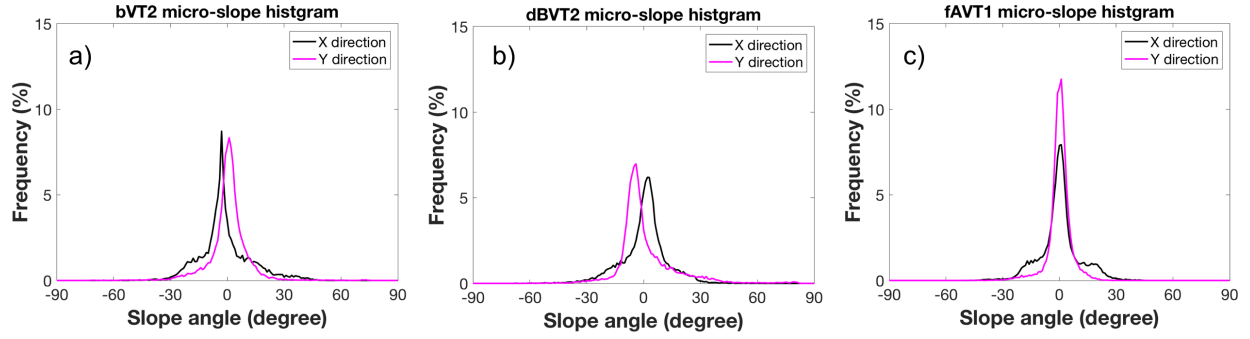


**Figure 4.9.** (a)Micro-slope angle distributions in the loading direction (Y) and sample thickness direction (X) of Valt samples' fractures under loading type C; (b)type B; (c)type A

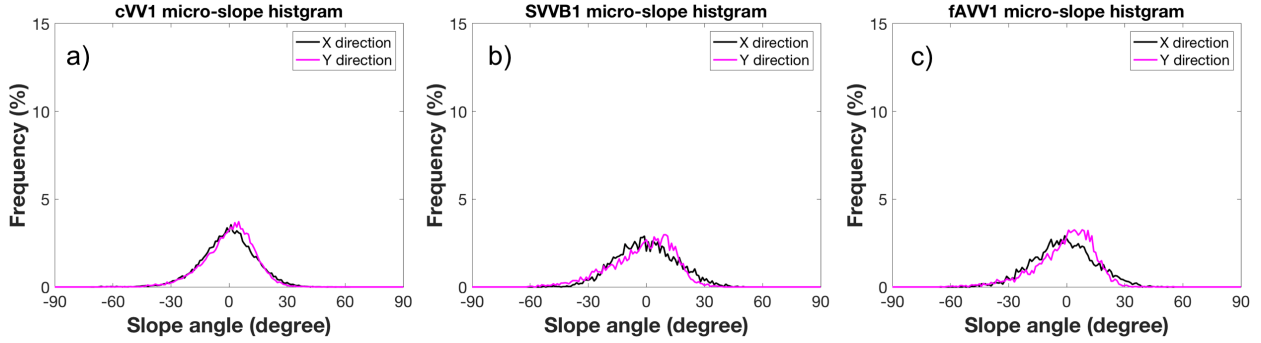


**Figure 4.10.** (a)Micro-slope angle distributions in the loading direction (Y) and sample thickness direction (X) of VV samples' fractures under loading type C; (b)type B; (c)type A

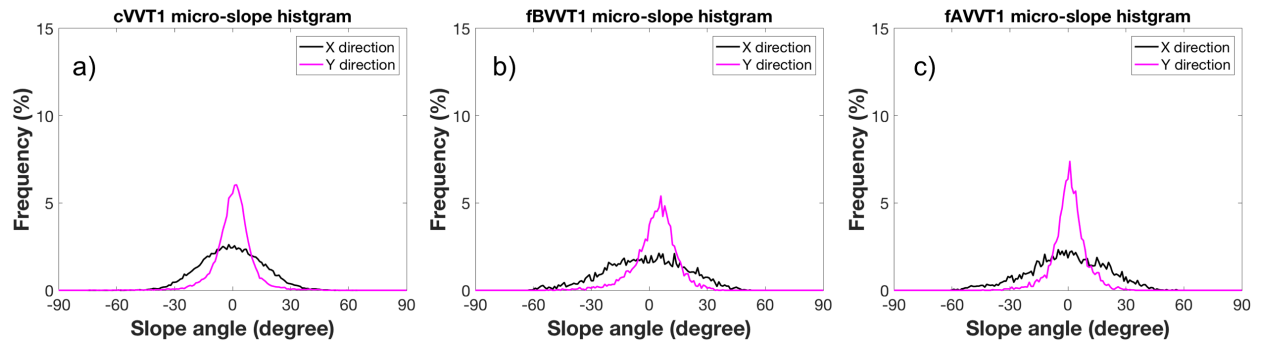


**Figure 4.11.** (a)Micro-slope angle distributions in the loading direction (Y) and sample thickness direction (X) of VValt samples' fractures under loading type C; (b)type B; (c)type A

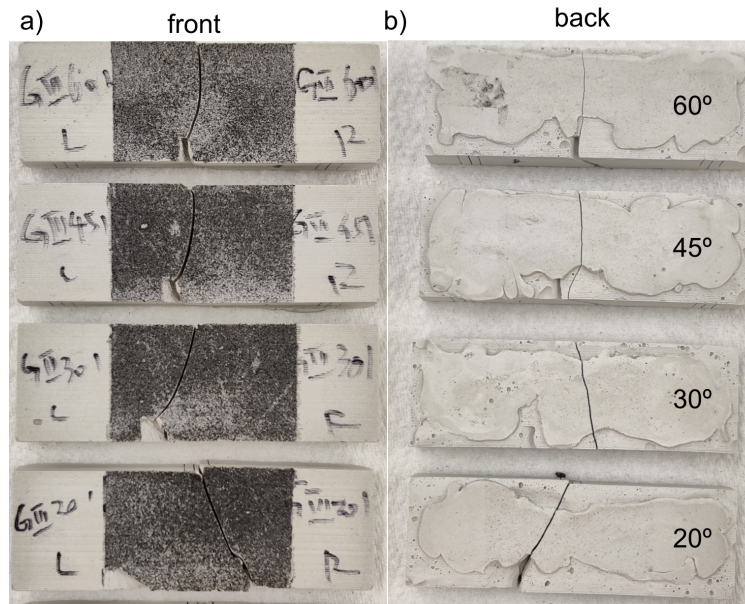


**Figure 4.12.** Photos of front and back faces of cast gypsum samples with notches tilted at angles of 60°, 45°, 30°, and 20°

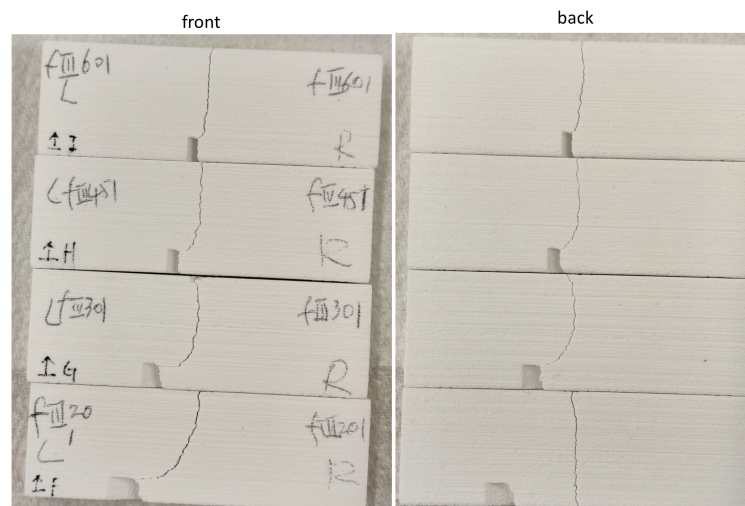


**Figure 4.13.** Photos of front and back faces of 3D printed gypsum samples (type H) with notches tilted at angles of 60°, 45°, 30°, and 20°

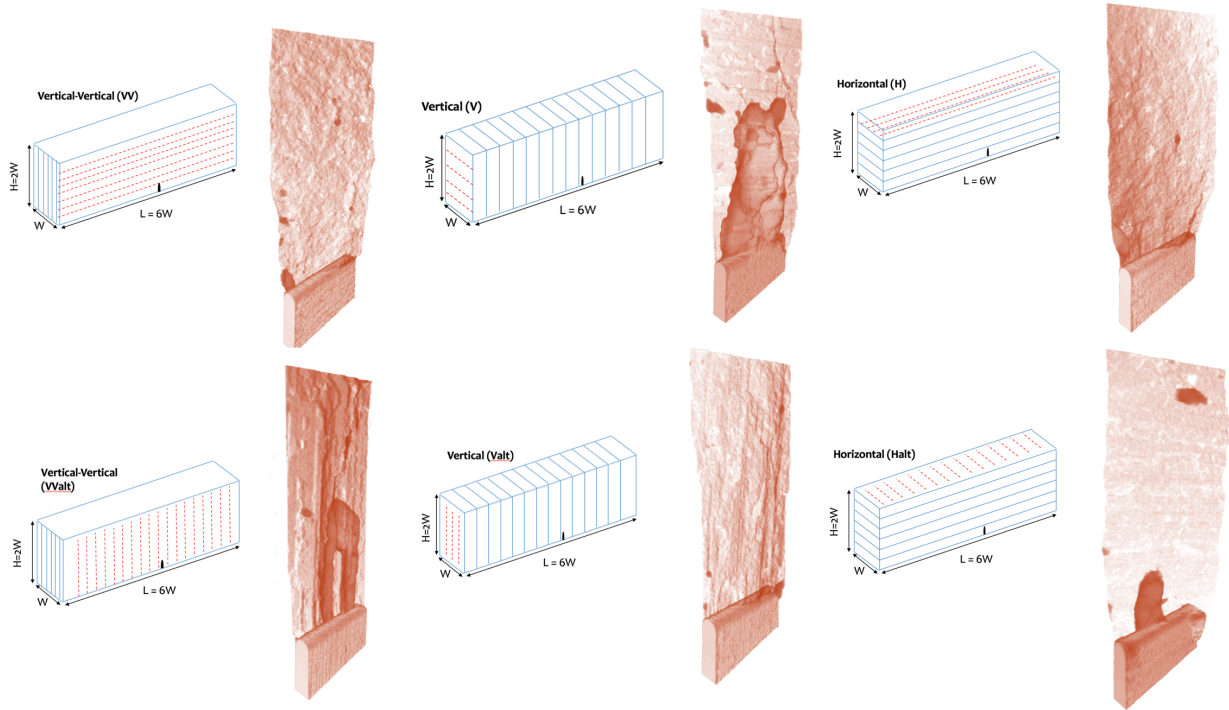


**Figure 4.14.** 3D view of the segmented reconstructed X-ray CT tomography of sample fractures with different bedding layers and mineral growth orientation directions (Mixed Mode I and III notch angle  $60^\circ$ ); bedding layer and mineral growth orientation directions regarding each sample type name are shown next to the fractures.



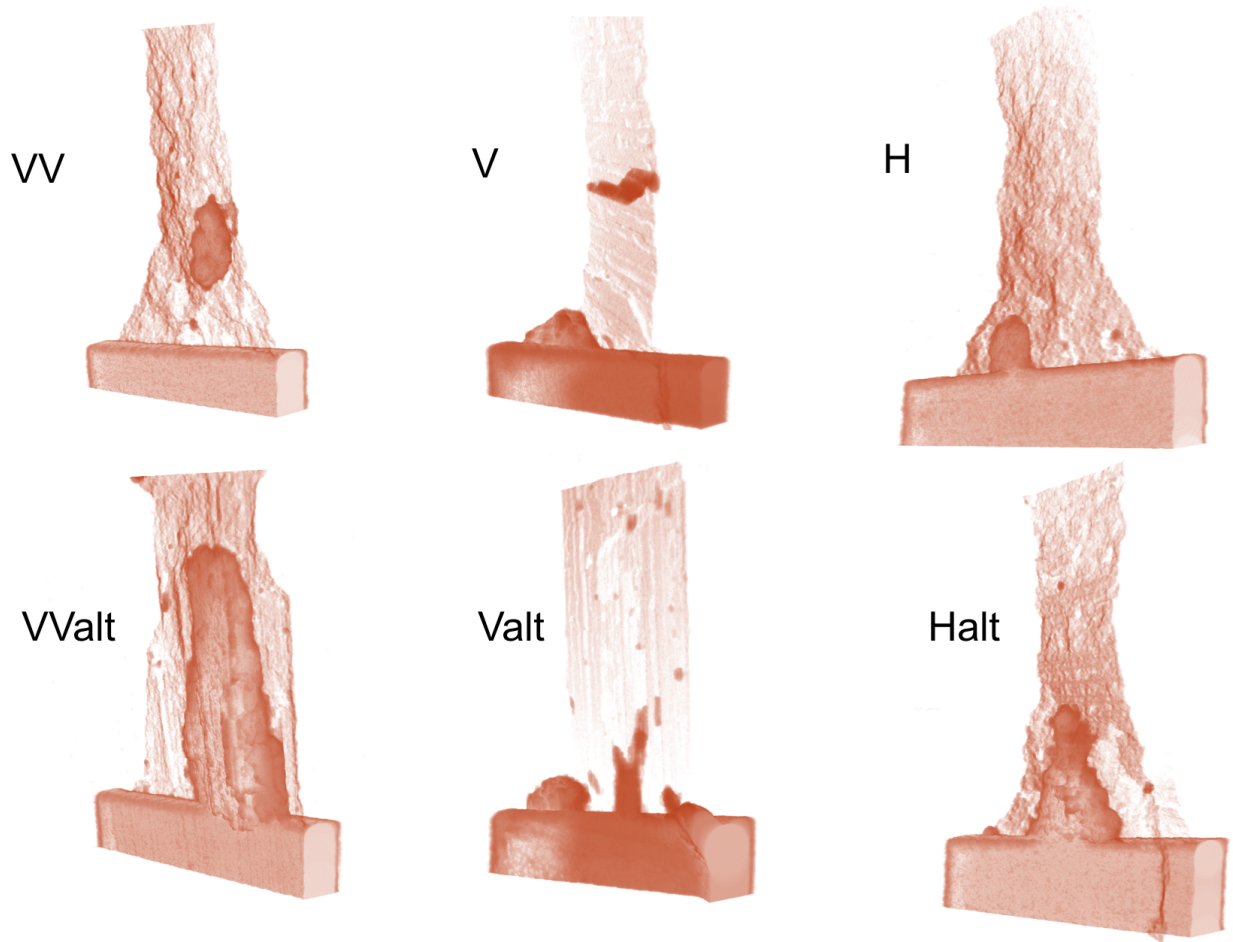


**Figure 4.15.** 3D view of the segmented reconstructed Xray CT tomography of sample fractures with different bedding layers and mineral growth orientation directions (Mixed Mode I and III notch angle  $45^\circ$ ); obvious thick chunk inside the fracture scan was the result of a missing piece after failure.

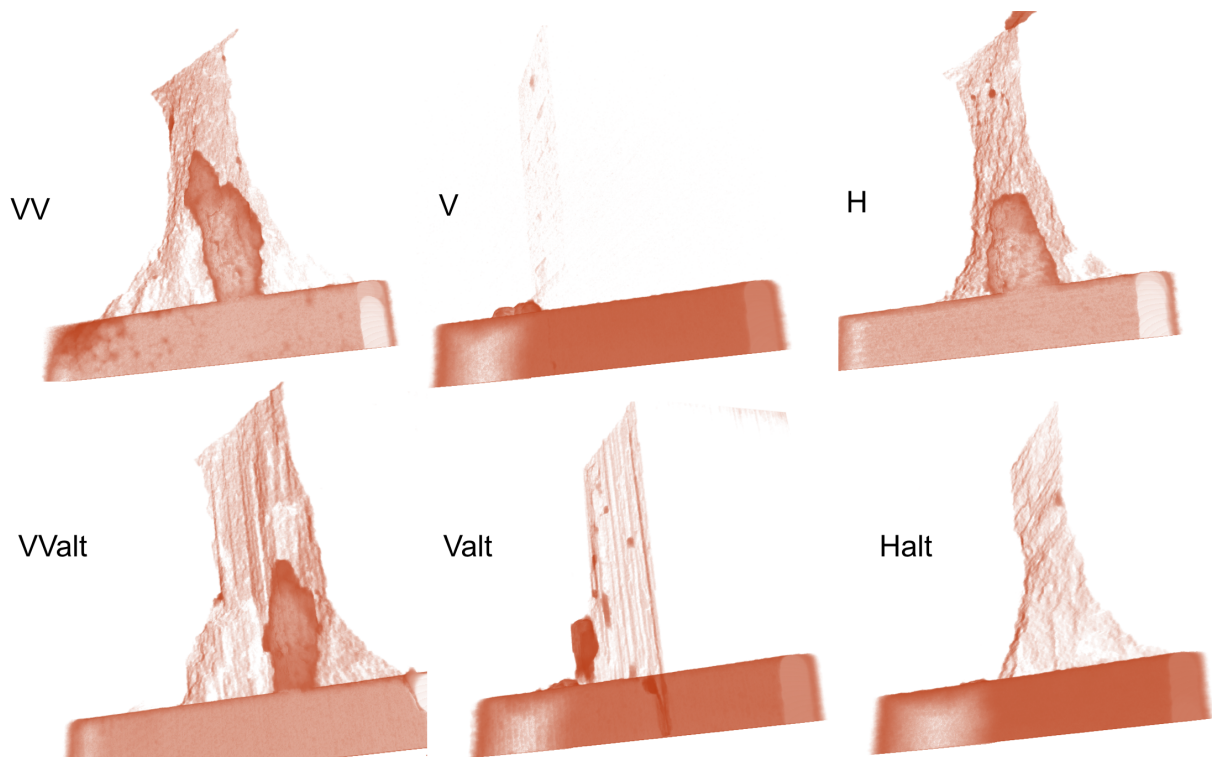


**Figure 4.16.** 3D view of the segmented reconstructed Xray CT tomography of sample fractures with different bedding layers and mineral growth orientation directions (Mixed Mode I and III notch angle  $30^\circ$ ); Some samples had fractures initiated not from the tip of the notch.

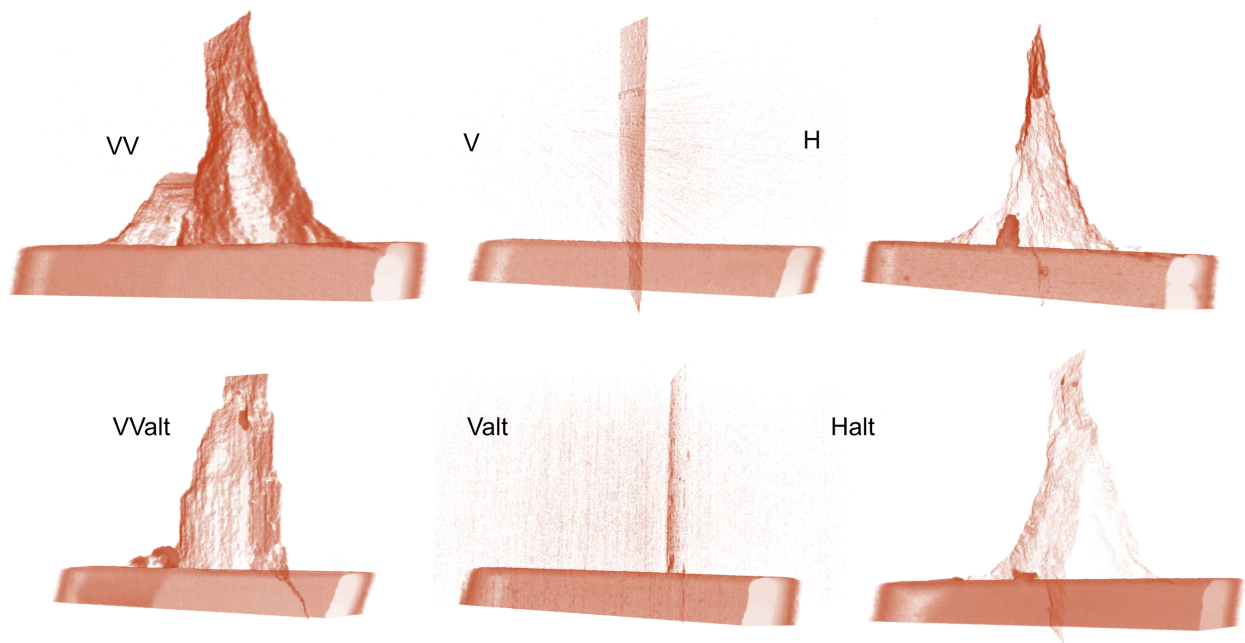


**Figure 4.17.** 3D view of the segmented reconstructed X-ray CT tomography of sample fractures with different bedding layers and mineral growth orientation directions (Mixed Mode I and III notch angle  $20^\circ$ ); Some samples had fractures initiated not from the tip of the notch; some samples had more than one single fracture surfaces.

## 5. ACOUSTIC EMISSION FROM LAYERED MEDIA DURING UNIAXIAL COMPRESSION TESTING

Acoustic emission sensing is often used to monitor crack and fracture initiation, propagation and coalescence during loading. Here, results from an acoustic emission study are presented that explore the effects of oriented layers and texture (oriented minerals) on fracture evolution in 3D printed gypsum samples. Portions of this chapter are from from Liyang Jiang's AEWG conference proceedings with permission from the Acoustic Emission Working Group (AEWG).

### 5.1 Sample Fabrication

3D printing was used to create analog gypsum rock samples. 100  $\mu\text{m}$  thick layers, of calcium sulfate hemi-hydrate (bassanite) powder, were bonded with a proprietary water-based binder, which chemically transformed the bassanite into gypsum [55]. The gypsum texture contained in a layer was controlled by selecting the direction of binder application and layering. The gypsum crystals formed bonds between sequential bassanite layers that were stronger than the gypsum-bassanite bonds, resulting in anisotropic material properties. UCS tests were conducted on printed cylindrical specimens (50.8 mm in height, 25.4 mm in diameter) with different orientations of bassanite layers and gypsum texture relative to the loading direction (Figure 5.1). Non-layered reference samples with no preferred mineral orientation were fabricated by casting gypsum in a mold. A silicon rubber mold was created from a solid resin sample (3D printed on a FormLabs 2) with the same dimensions as the 3D printed (3DP) samples. The mold was filled with mixed gypsum and water, then vibrated to minimize the amount of trapped air, and then cured. The resulting casted gypsum (CG) samples were cylindrical in shape and had the same heights and diameters as the 3DP samples.

## 5.2 Experimental Setup and Procedure

Acoustic-emission (AE) measurements were made to monitor time-dependent crack formation. The samples were monitored using an array of six (6) Physical Acoustics Corporation transducers - F15 $\alpha$  sensors (with flat frequency response between 20-400 kHz). The sensors were connected via preamplifiers to a Mistra/Physical Acoustics AE measurement system with a 10MHz sampling frequency. The threshold amplitude was set at 27 dB. AE sensing was also performed on an aluminum sample of similar dimensions alongside the geo-architected sample for the sample experimental time window to determine background noise. All transducers were secured to samples using hot Gorilla Glue. During monitoring, acoustic sensor transmission tests (AST) were also performed before and after active monitoring to determine the effect of drying and crack formation on compressional wave speeds. AST is a process by which the system allows the transducers to act as both a source and a receiver. The AST data provides velocities across the sample and between transducers, which are calculated from the respective arrival times.

All samples were loaded parallel to the long axis of the cylinder with an ELE International Soil Testing load frame with an S-shaped load cell (2000 lbs capacity). A steel ball and a steel spacer were placed on top of the samples to function as a spherical seat. AE measurements were recorded with Mistras Express II station together with load and displacement data synced by parametric channels. Broadband transducers (F15 $\alpha$  sensors from Physical Acoustics) were attached to the side of the cylinder samples at 6 different locations. 20-1200 kHz preamplifiers were used with a 60 dB gain and 27 dB threshold setting for recording. During monitoring, acoustic transmission tests were also performed to provide velocities across the samples. A 3D X-Ray Microscope (Zeiss Xradia 510 Versa) was used to image each sample after a test if coalescence did not lead to complete failure. The induced fractures were visualized in 3D using Dragonfly Pro software. If failure resulted in a sample breaking into two pieces, then laser profilometry was performed to determine the fracture surface roughness. An aluminum cylinder was also tested to determine the background noise levels.

Data were analyzed with Noesis software only for signals with peak frequencies between 200-400 kHz because lower frequency signals were identified as noise. The small samples (6 mm in diameter by 12 mm in height cylinders) were placed in a Deben CT5000 in-situ uniaxial loading device in the 3D X-ray microscope. During the loading several scans were performed at different loads to study the crack growth under different loading conditions. The loading rate was 0.1 mm/min with load information recorded at 100 millisecond sampling rate. Data reconstructions and analysis were performed using Object Research Systems (ORS) Dragonfly Pro 4.0 software.

### 5.3 Results

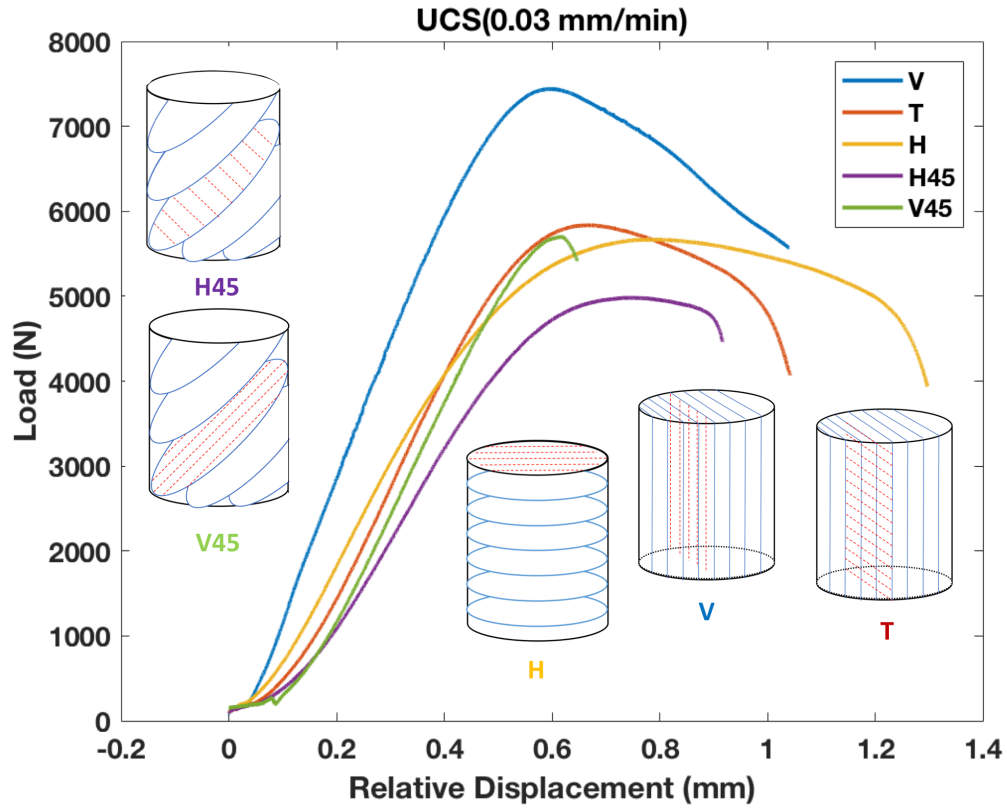


**Figure 5.1.** Sketch of 3D printed samples showing orientation of the bassanite layers (blue lines) and oriented mineral feature (red dashed lines) and the load displacement curves of each type.

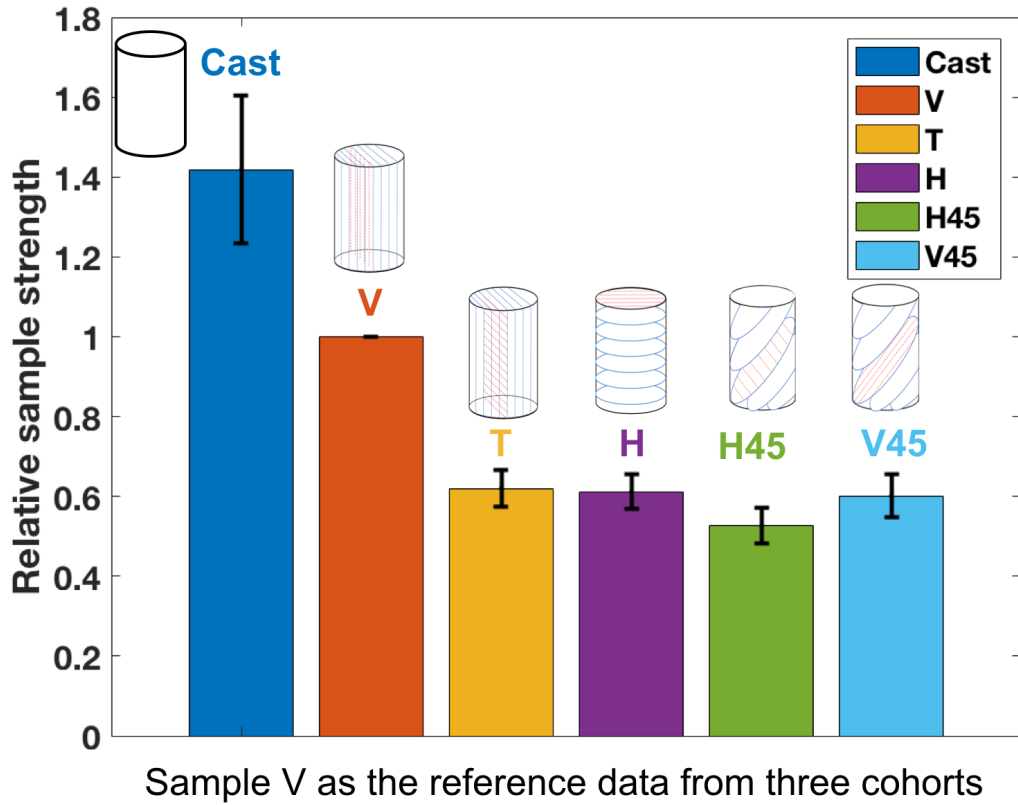


**Figure 5.2.** Test repeatability of UCS

Three cohorts of samples were measured where a cohort consisted of the caste gypsum sample and the 5 different 3D printed geometries (i.e. layer orientation and mineral fabric orientation). The measured peak failure load varied the most for cast gypsum samples. V samples were the strongest while H45 samples were the weakest. The largest values of UCS were observed in samples where both the layering and gypsum texture were oriented parallel to the loading direction. This is counterintuitive as usually breaking parallel to layering (see Chapter 2) resulted in lower failure strengths. However, the 3D sample V did not exhibit axial splitting but instead an inclined fracture formed causing the fracture to propagate across the gypsum mineral texture, and in turn leading to a higher failure load. The lowest UCS was found for samples with bedding layers oriented  $45^\circ$  to the applied load (Figure 5.1 and 5.2). Unlike the CG samples, no axial splitting was observed among the 3DP samples. Samples with the layering oriented  $45^\circ$  to the load failed along the bedding

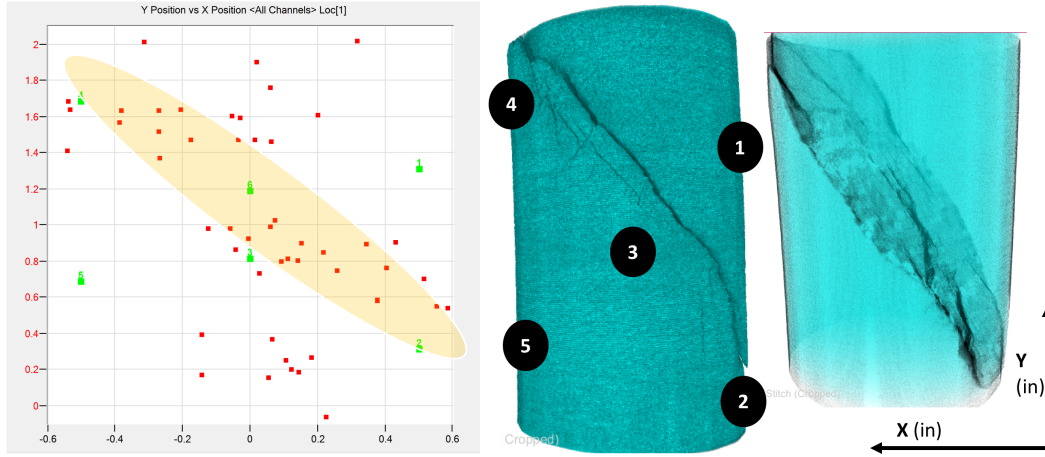


**Figure 5.3.** Estimated fracture location from AE and the reconstructed X-ray computed tomography images.

planes and typically broke into two pieces with smooth failure surfaces as determined from laser profilometry (Figure 5.4). Irrespective of the orientation of the layers and texture, all samples exhibited a single major crack that spanned the entire length of the sample that was inclined to the direction of loading.

As mentioned, the CG samples failed immediately after reaching a peak load, while 3DP samples exhibited ductile post-peak behavior. Figure 5.5 provides a comparison of the amplitude of the measured acoustic emission to the applied normal load as a function. Examination of the AE signal amplitude (Figure 5.5) from post-peak loading revealed that more ductile behavior was associated with more AE events that occurred over a longer period of time, and the resultant fracture surfaces were rougher than for narrow time distributions of events. Monitoring of AE signals during failure of rock has the potential to predict fracture roughness, and the mineral and layering orientations.

#### 5.4 Deben Results

Unconfined compressive strength tests were also performed on smaller 3D printed gypsum samples using a Deben CT5000 in-situ stress rig inside a Zeiss Xradia 510 X-ray microscope. Visual interpretation of how the material changed under different loading conditions was provided to determine the role of mineral texture orientation and layer orientation on fracture



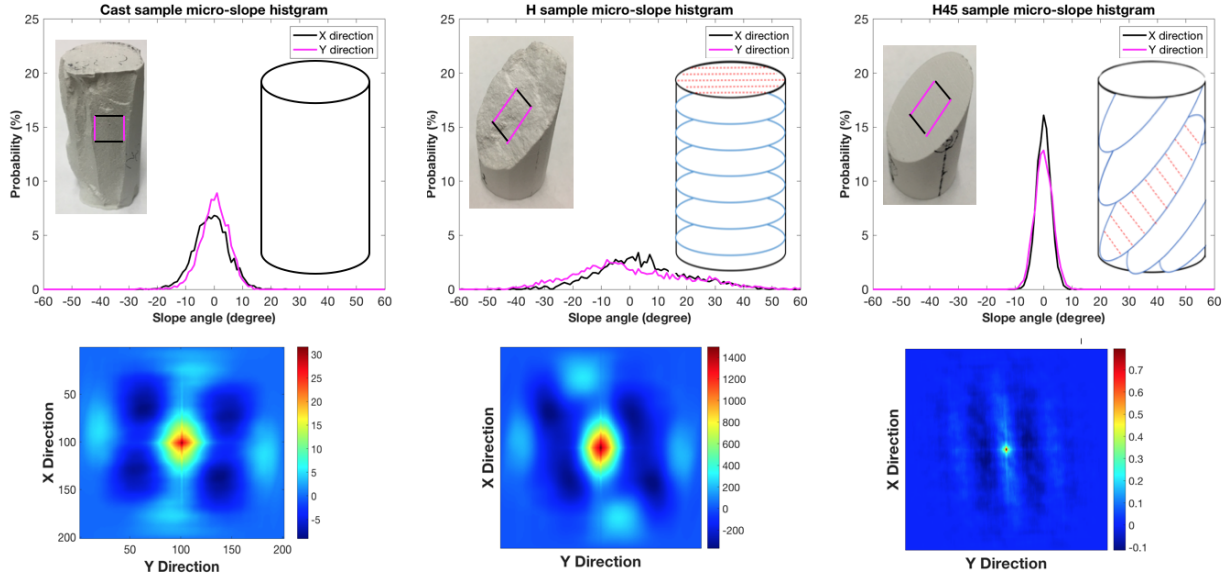


**Figure 5.4.** Micro slope and autocorrelation of induced surfaces for CG, H, and H45 samples

formation (Figure 5.6). No evidence of cracking for an imaging resolution of xx micrometers was observed before the sample reached the peak load. This indicates that only the signals after reaching the peak load were associated with cracking.

## 5.5 Conclusion

UCS testing found that the largest values of UCS were observed when both the layering and gypsum mineral texture were oriented parallel to the loading direction. The lowest UCS values were measured on samples with bedding layers oriented 45° to the applied load. Unlike the CG samples, no axial splitting was observed among the 3DP samples. Irrespective of the orientation of the layers and texture, all samples exhibited a single major crack that spanned the entire length of the sample, inclined to the direction of loading. Samples with bedding oriented 45° to the load failed along the bedding planes, breaking into two pieces with the smoothest failure surfaces as determined from laser profilometry. Examination of the AE signal amplitude distribution in time for post-peak loading revealed that a longer period of AE events correlated with more ductile behaviors and the resultant fracture surfaces were rougher than for narrow AE distributions.

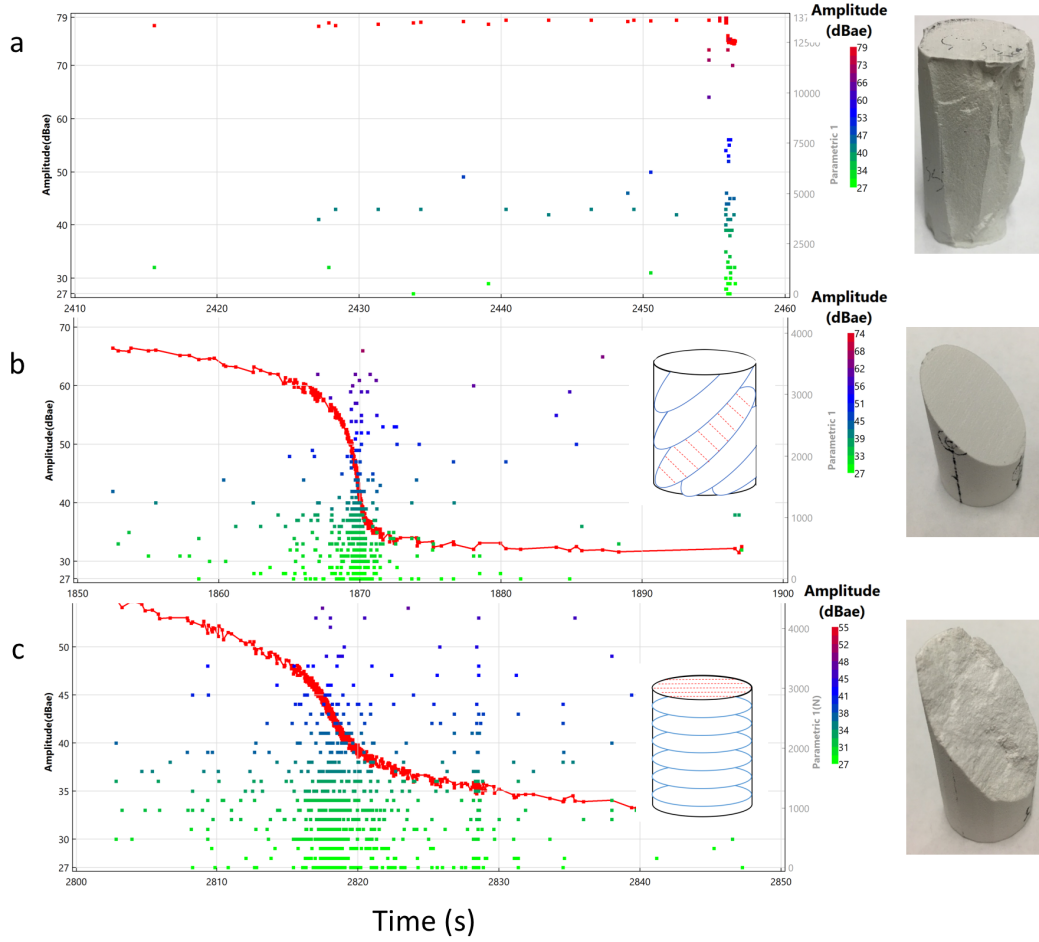


**Figure 5.5.** (a) The CG sample failed almost instantly and had the narrowest AE amplitude distribution in time; (b) The H45 sample had smoother fracture surfaces and a relatively narrower AE amplitude distribution compared to other 3DP samples; (c) The H sample exhibited the most significant ductile post-peak behavior, produced relatively rougher surfaces and a longer period of AE events.

The CG sample failed almost instantly and had the narrowest AE amplitude distribution in time. The H45 sample had smoother fracture surfaces and a relatively narrower AE amplitude distribution compared to other 3D printed samples. The H sample exhibited the most significant ductile post-peak behavior, produced relatively rougher surfaces and a longer period of AE events. The results have the potential to be used as an effective tool to study the influence of texture and layering on sample strength and cracking patterns

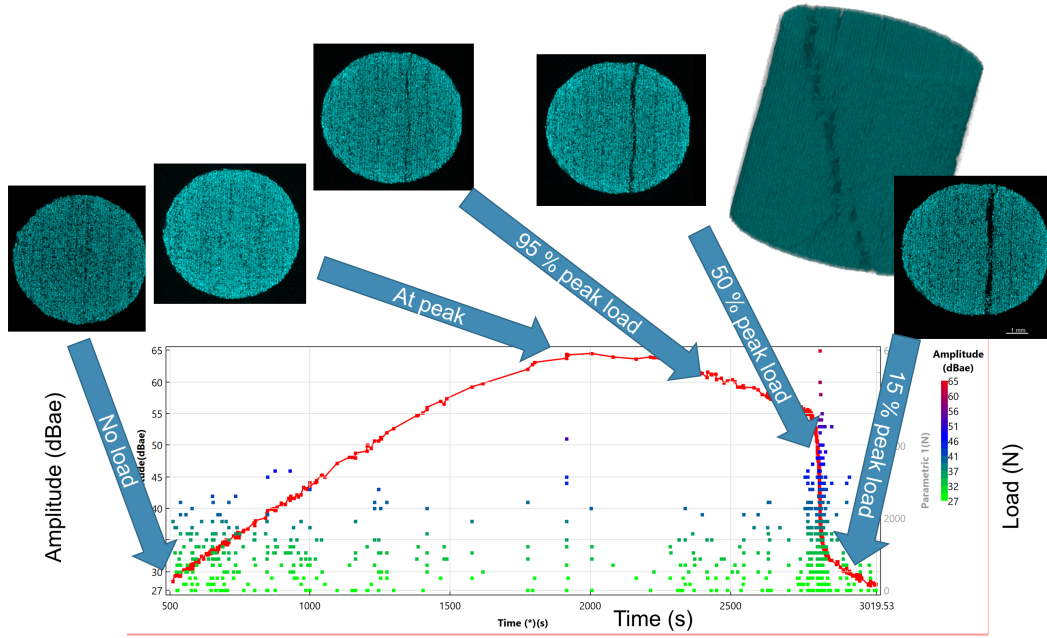


**Figure 5.6.** AE Amplitude Distribution in Time with cross section view of 3D reconstructed Xray CT tomography indicates the fracturing started after the peak load was reached (UCS-T type sample as Figure 2.7).

and monitoring AE signals during failure of rock may have the potential to predict fracture roughness and the mineral and layering patterns.

## 6. CONVERTED WAVES FROM ORIENTED VOIDS IN FRACTURES

In this chapter, the study of cross coupling, which is potential for remotely probing the fractures with passive seismic measurements are presented here. Portions of this chapter are from from Liyang Jiang's ARMA conference proceedings with permission from the American Rock Mechanics Association (ARMA) to use material.

### 6.1 Numerical Modeling

Compressional and shear wave propagation across a single fracture with oriented voids was simulated in 2D for a range of micro-crack-orientations to determine the sensitivity of P-S and S-P mode conversion on the details of the fracture void geometry. A discontinuous Galerkin (DG) approach was used to generate compressional and shear waves from a point source that were propagated across a fracture (Figure 6.1). The DG method enables waves to travel over multiple wavelengths with minimal dispersion [56], [57]. For more information on the details of the DG method, the reader is referred to [26] and [58].

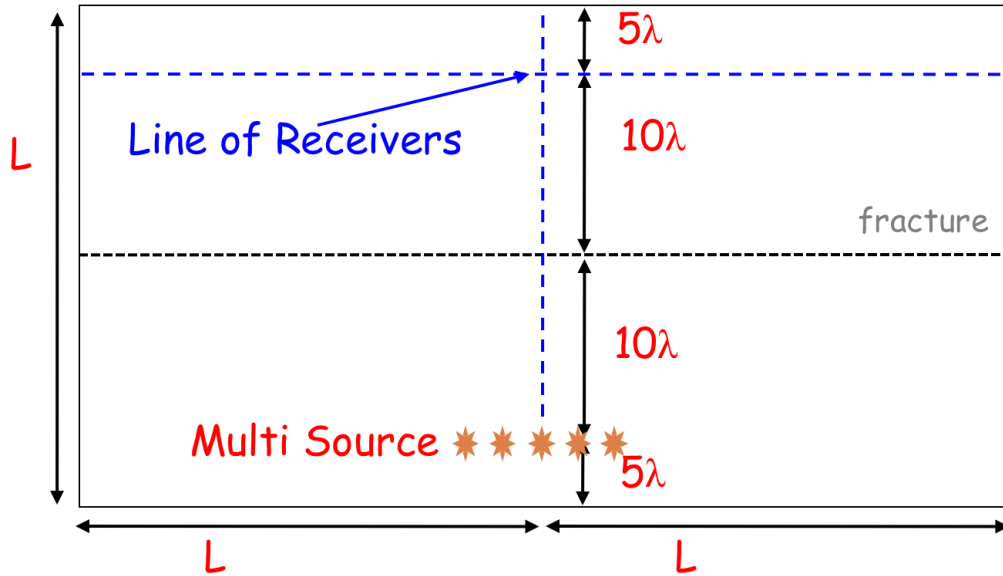


**Figure 6.1.** Structure of the modeling

In the simulation, the fracture was represented by a linear array of microcracks modeled as ellipses with a major axis = 2 mm and a minor axis = 1 mm. Microcrack orientations are taken relative to the orientation of the major axis. Inclination angles of  $\theta = 0^\circ, \pm 15^\circ, \pm 30^\circ, \pm 45^\circ, \pm 60^\circ, \pm 75^\circ$ , and  $90^\circ$  were studied. For  $\theta = 0^\circ$  the spacing between the microcracks was 1 mm, and then increased as  $\theta$  increased, i.e. the number of voids was held constant but the contact length changed as the inclination angle of the voids changed. Each void was rotated about its center.

The fracture resided in an isotropic medium with a compressional wave velocity of 2500 m/s, a shear wave velocity of 1250 m/s and density of  $1170 \text{ kg/m}^3$ . Simulations were performed using the computational domain shown in Figure 6.1 where  $L = 25\lambda$  for a wavelength of  $\lambda = 2.5$  mm at 1 MHz.

A computational domain with the same dimensions but with no fracture was used to obtain an “intact” signal to use as a reference signal. The stress at the receiver directly across from the source was used to analyze the transmission of P-P, S-S and P-S/S-P modes for source central frequency of 0.5 MHz. Micro-crack orientation affected the transmitted waves as shown in Figure 6.2. For P-P transmission, the signal amplitude increased with increasing  $\theta$ . This is consistent with an increase in fracture specific stiffness because the contact area between the voids increased as the voids were rotated at a fixed location. However, this did not significantly affect the S-S transmitted amplitude. The transmitted wave amplitude for the P-S and S-P waves were significantly affected by the microcrack orientation. The cross-coupling stiffness is observed to be finite but relatively weak for  $\theta = 0^\circ$  and  $\theta = 90^\circ$ . The non-zero amplitudes are attributed to scattering from the ends of the ellipses. The cross-coupling stiffness reached a maximum for  $\theta = 45^\circ$  where the largest P-S/S-P amplitudes are observed.

## 6.2 Experimental Approach

Experiments were performed to examine the effects of oriented voids in a fracture on energy partitioning among compressional, shear and converted waves, and to compare to the simulation results.

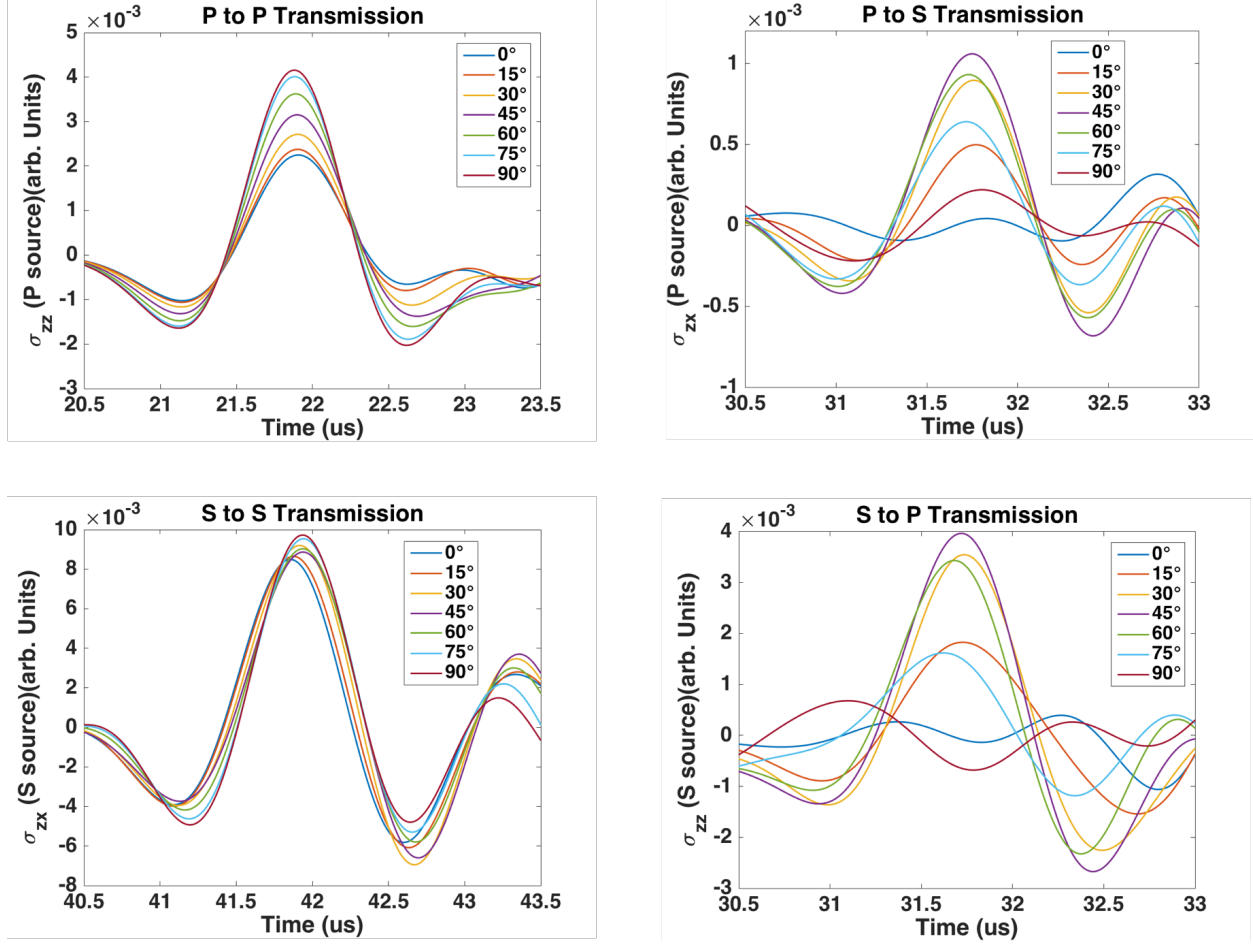


**Figure 6.2.** Simulated transmitted (upper left) P-P, (lower left) S-S, (upper right) P-S and (lower right) S-P for fracture void orientations of  $\theta = 0^\circ, 15^\circ, 30^\circ, 45^\circ, 60^\circ, 75^\circ$ , and  $90^\circ$

### 6.2.1 Samples

A FormLabs 2 3D printer was used to fabricate 12 samples that measured  $100mm \times 50mm \times 50mm$ . The 3D printer uses stereolithography to transform a clear liquid resin into a solid material [59]. The samples were printed with a layer resolution of 25 micrometers. Each of the 12 samples contained a linear array of micro-cracks with a single orientation. The orientations studied included  $\theta = 0^\circ, \pm 15^\circ, \pm 30^\circ, \pm 45^\circ, \pm 60^\circ, \pm 75^\circ$ , and  $90^\circ$ . A 25 mm length of each sample contained no micro-cracks to act as a reference material because the repeatability of the 3D printed material was found to vary among printings, even for the same resin, print specification, and print orientation. The orientation of the sample

during printing was chosen to enable the liquid resin to drain to create open micro-cracks. The spacing of the micro-cracks was based on a center-to-center spacing of 3 mm. The crack length was 2 mm and the width was 1 mm, and extended 50 mm in depth. Amongst samples, the voids were rotated about their central axis. This resulted in samples with the same void volume but different amounts of contact area (i.e. regions between the micro-cracks similar to the simulated geometry in section 6.1). A Zeiss Versa 510 3D X-ray microscope was used to image the printed void geometry. The X-ray images show that the cross section of the micro-cracks are elliptical in shape and that the dimensions of the crack width and height were smaller than the print specification, (Figures 6.3 , 6.4) by roughly 200 - 300 micrometers..

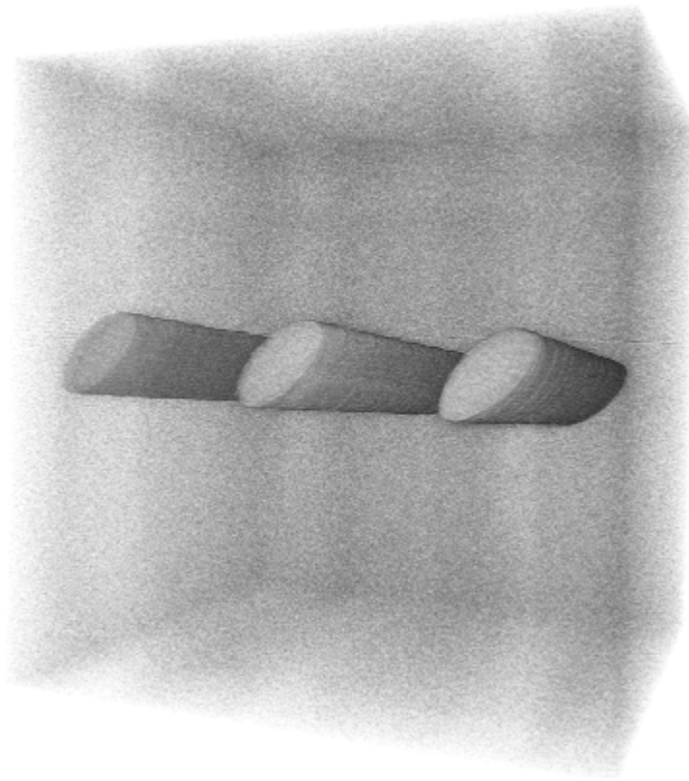


**Figure 6.3.** X-ray CT reconstructed 3D image of 8 mm portion of the 45° sample.



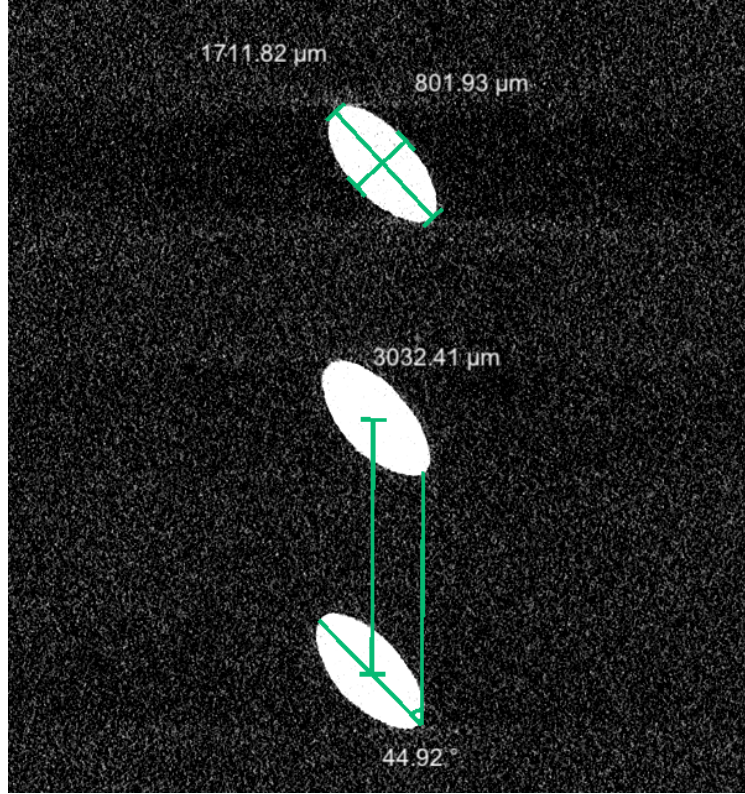


**Figure 6.4.** Actual dimensions of voids in the 3D printed sample for  $\theta = 45^\circ$ . On average, the crack length was 1.7 mm and the width was 0.8 mm.

### 6.2.2 Ultrasonic Measurements

Olympus Panametric piezoelectric contact transducers (V-103 and V-153) were used to send and receive ultrasonic (central frequency of 1 MHz) signals. Shear waves measurements were made with the source and receiver polarized perpendicular and parallel to the long axis of the micro-cracks. All measurements were made at normal incidence to the fracture plane. The transducers were coupled to a sample with baked honey (8.75% weight loss) and mounted on a sample using two steel plates connected by four springs. The spring extension length was measured and controlled to apply constant load (74 lbs) for all experiments to minimize the effect of coupling on the measured signals. Measurements were recorded over 6 hours to ensure the stability of the signal (within 2% difference, which is a systematic error from the source). An Olympus 5077PR pulse generator, set at 400V excitation with a 1 MHz repetition frequency was used to excite the piezoelectric transducers. After propagating



through a sample, the signals were digitized using a National Instruments USB-5133 digitizer and stored on a computer for analysis. A sampling rate of 100 MSamples/sec was used to get a bin size of 0.01 microseconds.

### 6.2.3 Calibration

Calibration experiments were performed to account for differences among the compressional and shear wave transducers in response to a transmitted S or P wave, and because different transducers were used to measure the transmission signals on different samples. A specially designed aluminum block was used to calibrate measurements of P-S conversions using an aluminum - air interface. Gain difference between different pair of transducers was smaller than 2%, which is the systematic error from the source.

## 6.3 Results

### 6.3.1 Simulate Shearing Along Fracture with Oriented Voids

Instead of applying shear stress on a fracture to change the void orientation like Nakagawa et al. ([38]), 3D printed resin samples with periodic patterns were used as analogies for different shearing and roughness conditions. To check if an analogy sample can simulate different shear conditions experiments were conducted with voids with or without preferred void orientations. Three samples with  $\theta = \pm 30^\circ, \pm 45^\circ, \pm 60^\circ$  respectively were printed with the no preferred shear orientation (Figure 6.5). These are examples of saw tooth shaped fracture creating both positive and negative oriented voids when there is no shearing. The different angles of orientations are to mimic different roughness. For a P transducer as source and an S transducer as the receiver, there is no significant signal in the P-S conversion mode time range ( P-S region in Figure 6.5), and the P-P transmission is higher in amplitude for the higher angles that result in more contact area. This results show that there is no cross coupling when there is no shearing and the fracture stiffness is higher when the fracture is rougher (i.e. greater microslope angle). Next, samples were printed (Figure 6.6) with an extra positive or negative angle oriented void to simulate the case with nonuniform shearing along a fracture. In this case, P-S converted mode was observed that provides evidence of

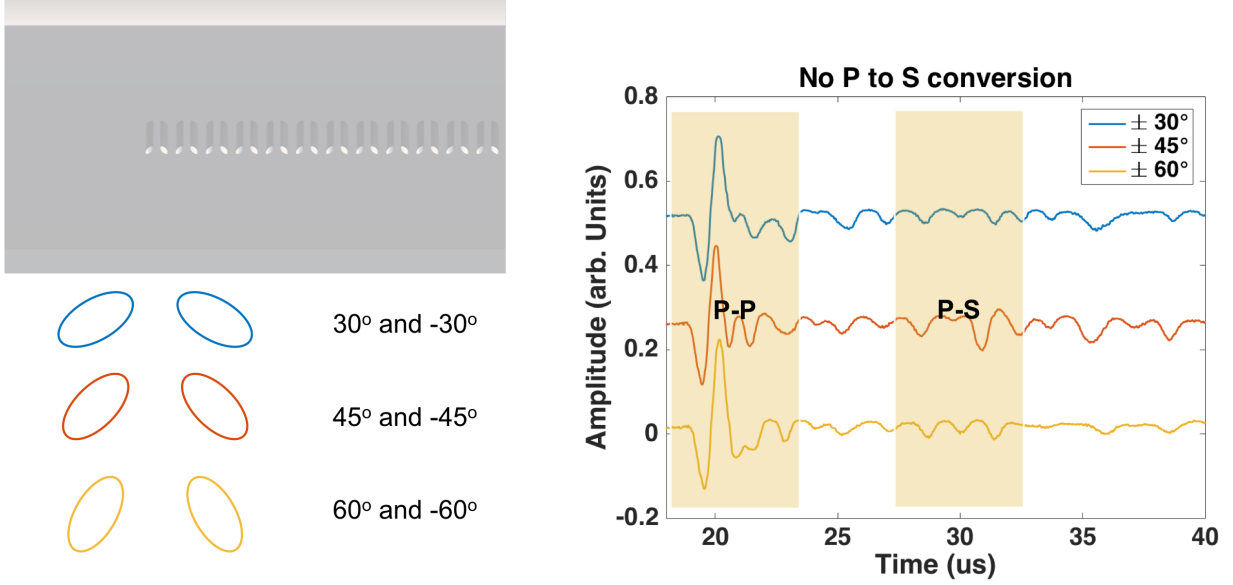


**Figure 6.5.** Simulate no shear along fracture with void orientations of  $\theta = \pm 30^\circ, \pm 45^\circ, \pm 60^\circ$  (left); No P-S converted mode observed when there is no shearing (right).

cross coupling when there is shearing which results in a more of the voids having a preferred orientation. In this case, 60% of the void have the same orientation.

### 6.3.2 Fixed Void Spacing and Fixed Void Geometry but Variable Angle

To mimic sheared fracture, one direction samples were printed with all voids oriented at the same angle. For normally incident waves on the array of cracks, the emergence of wave conversions (P-to-S or S-to-P waves) is an indication of the existence of oriented cracks (Figures 6.7, 6.8 , 6.9). As predicted by the simulations, the amount of energy partitioned into converted modes is greatest for fractures with void inclinations of  $\theta = 45^\circ$ , and least for P-S transmitted amplitudes are observed for  $\theta = 0^\circ$  and  $90^\circ$  (Figure 6.8 , 6.9). In addition, cracks oriented with the same magnitude of inclination but with negative and positive angles, the P-S/S-P modes are  $180^\circ$  out of phase as predicted by the theory [38] (Figure 6.7).

As the microcrack orientation increased from  $0^\circ$  to  $90^\circ$ , normally incident P-to-P transmitted wave amplitudes increased significantly, while S-to-S wave amplitudes were relatively constant for different cracks orientations (Figure 6.10).

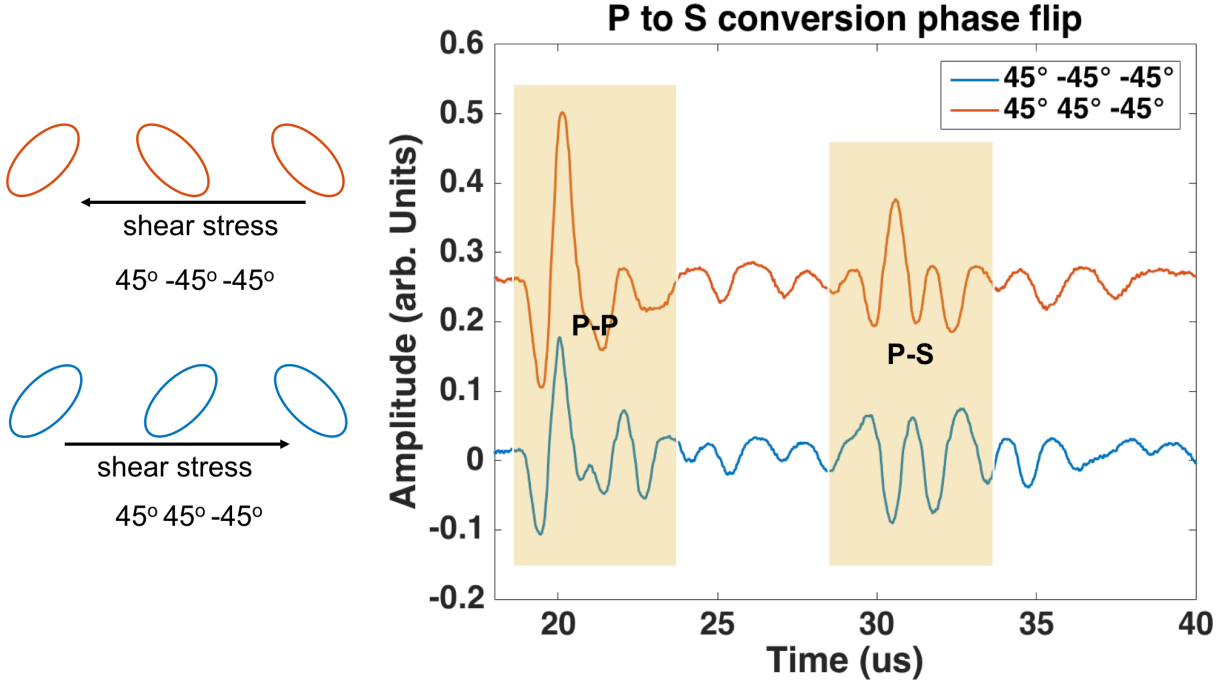


**Figure 6.6.** Simulate small shear in two different directions along fracture with void orientations of  $\theta = +45^\circ, -45^\circ, -45^\circ, \theta = +45^\circ, +45^\circ, -45^\circ$  (left); P-S converted mode observed when there is shearing (right).

From comparison of Figures 6.11 and 6.12, the observed energy partitioning from the experiments is similar to the simulated results except for the S-S transmission. The measured S-S transmission coefficients are higher than those from the simulation. A wavelet analysis showed that the central frequency of the measured S-S wave was 0.24 MHz compared to a value of 0.5 MHz from the simulations. This suggests that additional frequency filtering is occurring in the experiments that is not captured by the 2D simulation. Additional work is required to confirm this hypothesis.

The simulated P-S transmission signals from positive and negative angles are strictly  $180^\circ$  out of phase (Figure 6.8), whereas the experimental data displays a minor difference (Figure 6.7). The differences in signal components from the measure data may arise from the anisotropic nature of the 3D printed material. During printing, the sample was inclined resulting in a lack of material symmetry in material properties for opposite crack orientations,

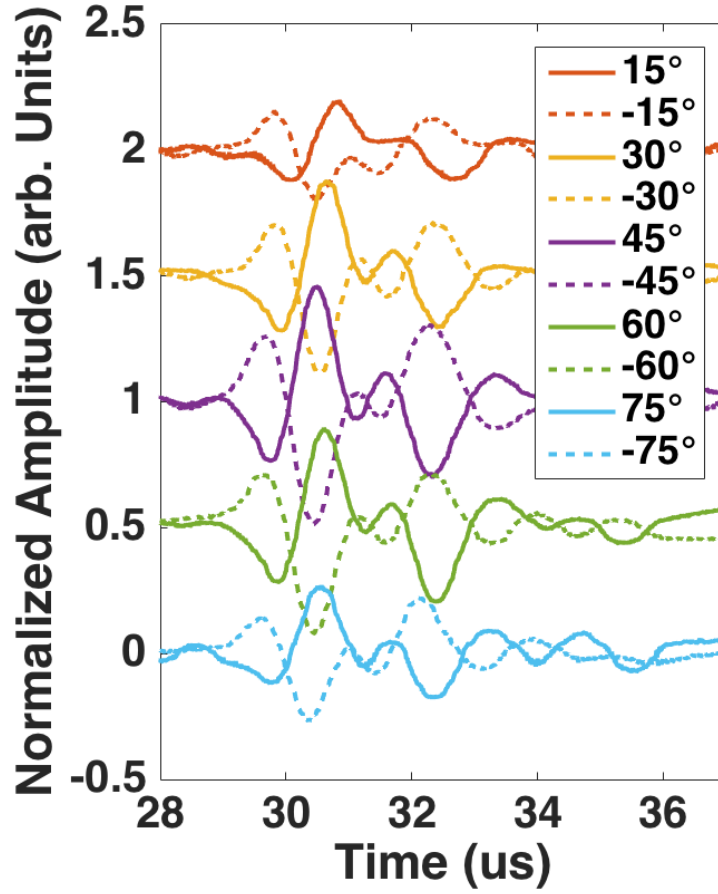


**Figure 6.7.** Measured P to S converted modes of the same oriented microcrack inclination from  $15^\circ$  to  $75^\circ$  for both negative and positive orientations.

i.e. orientation relative to the layering in the sample. Future work is required to extend the theory for anisotropic media.

### 6.3.3 Fixed Void Spacing and Fixed Void Angle but Different Void Geometry

The experimental results in previous section show that the generation of P-S or S-P converted mode is intimately linked to the orientation of the fracture void. This results in the question: how does the shape of a void affect P-S conversions. The following experiments and simulations were designed to study whether changing the shape of the voids alone will effect the P-P, S-S, P-S, S-P energy partitioning. Here, samples were printed with diamond-shaped, and rectangle-shaped voids to compared to the samples with elliptical voids. The length and

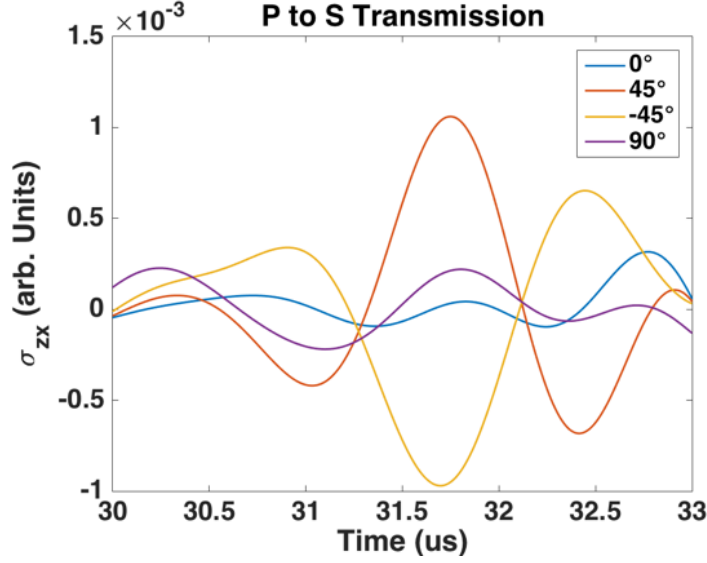


**Figure 6.8.** Simulated P-S conversion signals on positive and negative 45°-oriented cracks.

height of the rectangles and the diagonals of the diamonds were kept the same as the long and short axes of the ellipses (Figure 6.13 left). Simulations were also conducted (Figure 6.14 left) for the same geometries. When the void shape changed from diamond to ellipse to rectangle, the void volume increased and resulted in smaller S-S and P-P transmission amplitudes. Thus, fracture specific stiffness is related to void volume[60]. The smaller the void volume the higher the value of fracture stiffness. Figure 6.14 (center and right) demonstrates with the simulation's results for samples with different void shapes but oriented at an angle ( $\theta = 45^\circ$ ). It shows that the shape of the void has a slight effect on the P-S and S-P conversions. The rectangular shaped voids provide a larger more uniform surface (i.e. all at the same orientations) than either the ellipse or diamonds.

#### 6.3.4 Fixed Void Angle and Fixed Void Geometry but Different Spacing

Experiments and simulation work were performed for micro-cracks with the same shape and orientation of the voids but the spacing between each void was changed to examine the effect of contact area (spacing of the voids) on mode conversion. Experiments were performed with three samples with 45° angle-voids separated by 2 mm, 3 mm, and 4 mm

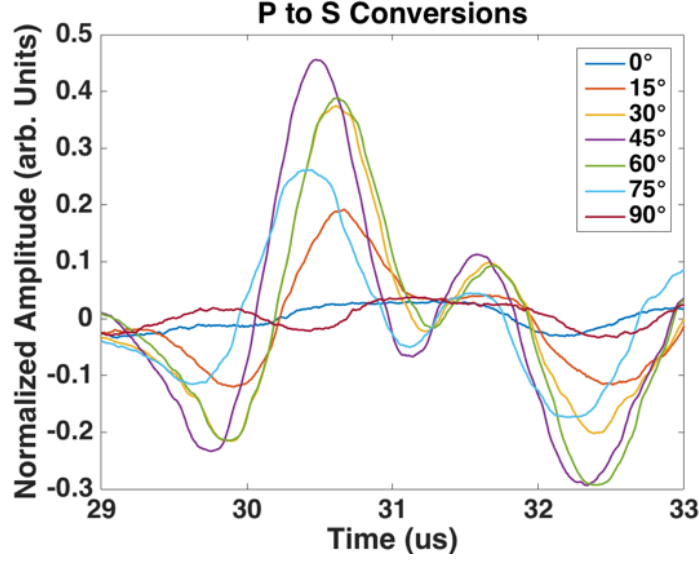


**Figure 6.9.** P-S wave conversions emerged and increased in amplitude as the crack inclination increased from  $0^\circ$  to  $45^\circ$ .

respectively. Figure 6.15 shows that an increase in contact area resulted in the expected increase in transmitted P-P energy. However, the energy associated with the P-S conversion decreased. This occurs because there are fewer oriented surfaces in the collection window of transducers resulting in fewer regions where conversion could occur. The simulation 6.16 for 5 different spacing showed the same trends for S-S transmissions and S-P conversions as the experimental results.

#### 6.4 Wave Propagation Through Oriented Voids Filled with Viscous Fluids

Here, the question of how a fluid affects the cross coupling is addressed through a series of experiments. Experiments were performed on 3D printed samples with oriented micro cracks that are saturated with a fluid for a range of viscosities. Water and silicon oil with different viscosities (1, 10, 100, 1000, 10k, 100k, 300k cSt) were used to determine how fluid-filled oriented voids in a fracture affect energy partitioning.

A FormLabs 2 3D printer was used to fabricate samples ( $50\text{mm} \times 50\text{mm} \times 100$ ) with a linear array of micro cracks oriented at  $45^\circ$  (the angle that partitions the most energy into P-S converted mode) with a printing resolution of 25 micrometers. The micro-cracks had

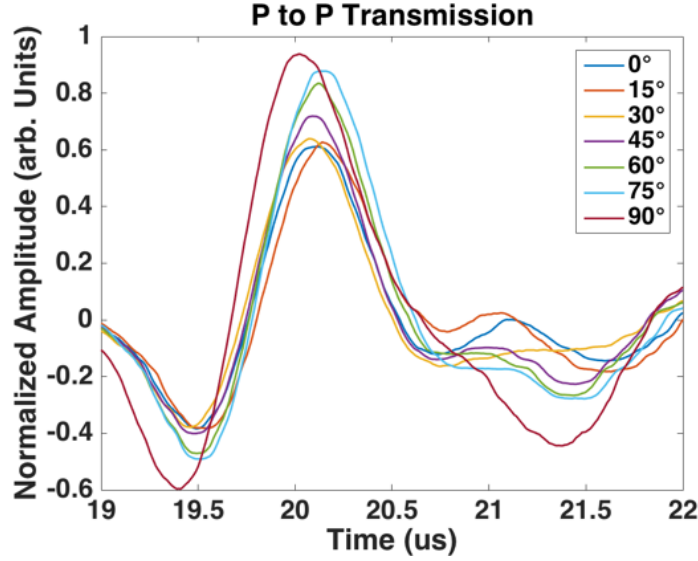


**Figure 6.10.** P-wave amplitude increased, as the micro-crack orientation increased from  $0^\circ$  to  $90^\circ$ .

elliptical cross-sections (2 mm long x 1 mm wide), through the 50 mm thickness of a sample, and were spaced 3 mm apart (center-to-center for adjacent cracks). Broadband transducers (0.2-1.5 MHz) were used to transmit and receive P and polarized S wave signals that were propagated at normal incidence to the linear array of micro cracks.

Examination of transmitted P-P and S-S waves, and P-S converted mode reveals that the P-S converted mode exhibited the most sensitivity to fluid viscosity. Figure 6.17 shows wavelet analysis [61] of the P-P transmission of the signals propagated through samples for 3 different fluid viscosities and one case where there is no fluid in the oriented voids. There are differences when water added to an empty fracture and the viscous fluid silicon oil will make the wavelet pattern bifurcating. However, the difference between low and high viscous silicon oil fill was small. Figure 6.18 shows the wavelet analysis of S-S wave transmissions with the similar experimental designs. The viscous fluid fill in an empty fracture did not make a huge difference here. Figure 6.19 is where we used converted signals to study the influence of the fluid fill. All 4 sub-figures shown a distinction. The spectral content of the P-S mode was observed to be affected when a viscous fluid filled the voids. The central frequency of the P-S converted mode was observed to increase (100-200 kHz) while P-P and S-S transmitted signals through silicon oil-filled cracks exhibited a smaller shift compared to air-filled micro

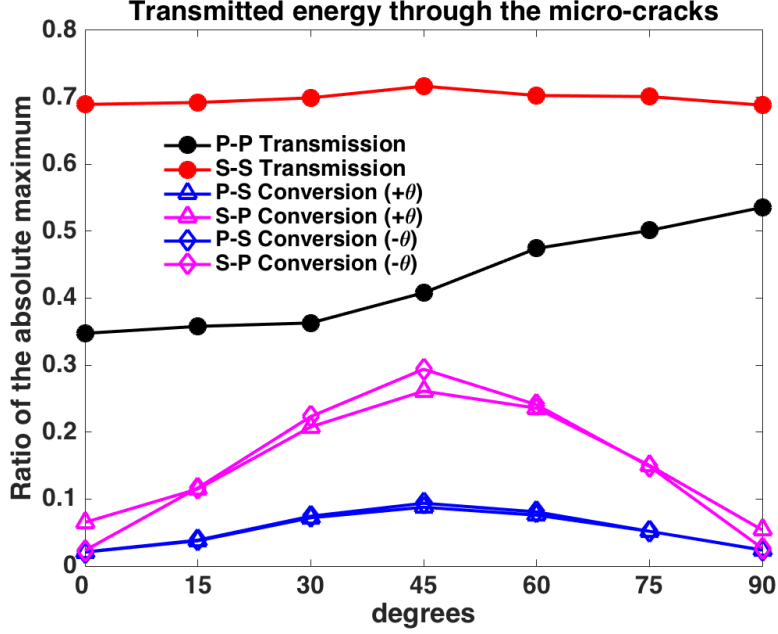


**Figure 6.11.** Transmission coefficients from normal incidence by experiments.

cracks and between high and low viscosity fluids. The P-P and S-S wave modes showed slight increases and decreases, respectively, in amplitude (less than 10%) when the fluid viscosity increased. However, the amplitude of the P-S mode exhibited a significant decrease (about 30% between 1 - 100k cSt). This suggests that P-S converted mode provides a potential method to remotely probe changes in fluid viscosity in fractures.

## 6.5 Conclusions

3D printing enabled the study of microstructural effects on macro-scale energy partitioning of waves into bulk and converted modes. In this project we used 3D printed resin samples as mimics to test wave cross coupling through fractures under shear stress. The convenience of 3D printing enabled the precision and easy fabrication of samples with voids in all kind of conditions so that the geometry property and fluid fill influences on wave energy partitioning in transmission and conversion can be studied. Simulation study was conducted and compared with experiments so that the understanding of the prediction of fracture property by seismic testing can be applied in other cases with more complicated



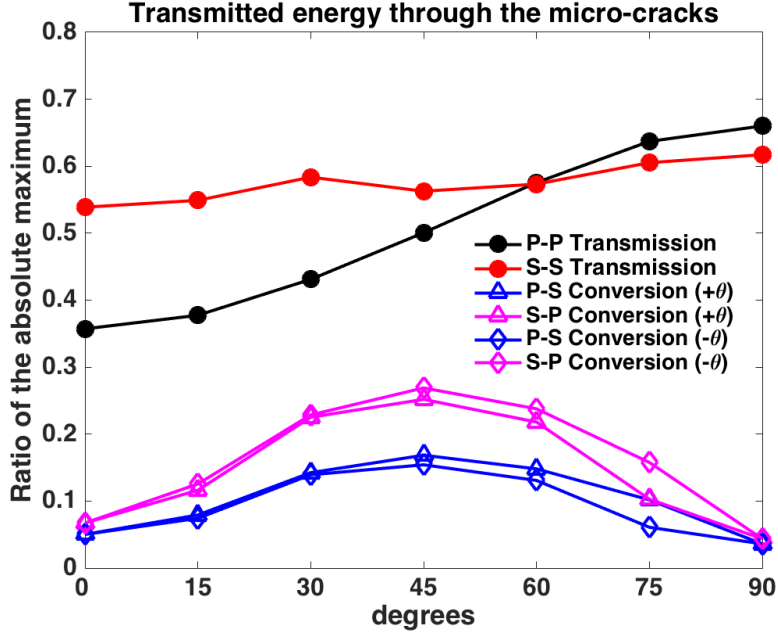


**Figure 6.12.** Transmission coefficients from normal incidence by simulation.

fractures. The observed energy partitioning matched the computed compliances obtained from discontinuous Galerkin simulations. Information on local fracture geometry and fluid flowing through is contained in the far-field waves. This finding supports a wide range of potential applications for monitoring and determining the presence and inclination angle of mechanical discontinuities along fractures in geologic and engineered materials.

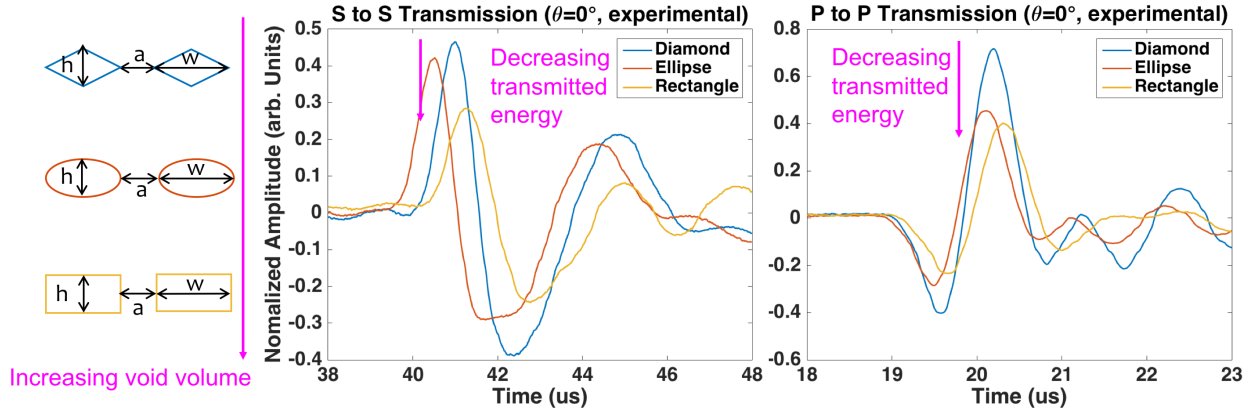


**Figure 6.13.** Experimentally measured S-S and P-P transmitted wave signals for voids with the same oriented angle ( $0^\circ$ ) and same spacing (3 mm) on samples with different void geometries.

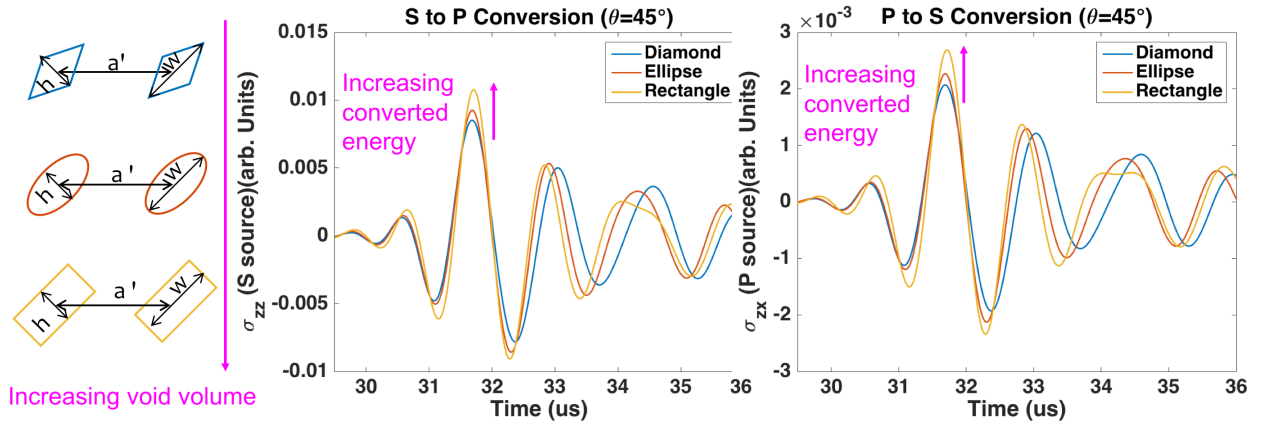


**Figure 6.14.** Simulation results of S-P and P-S converted modes for voids with the same oriented angle ( $0^\circ$ ) and same spacing (3 mm) on samples with different void geometries.

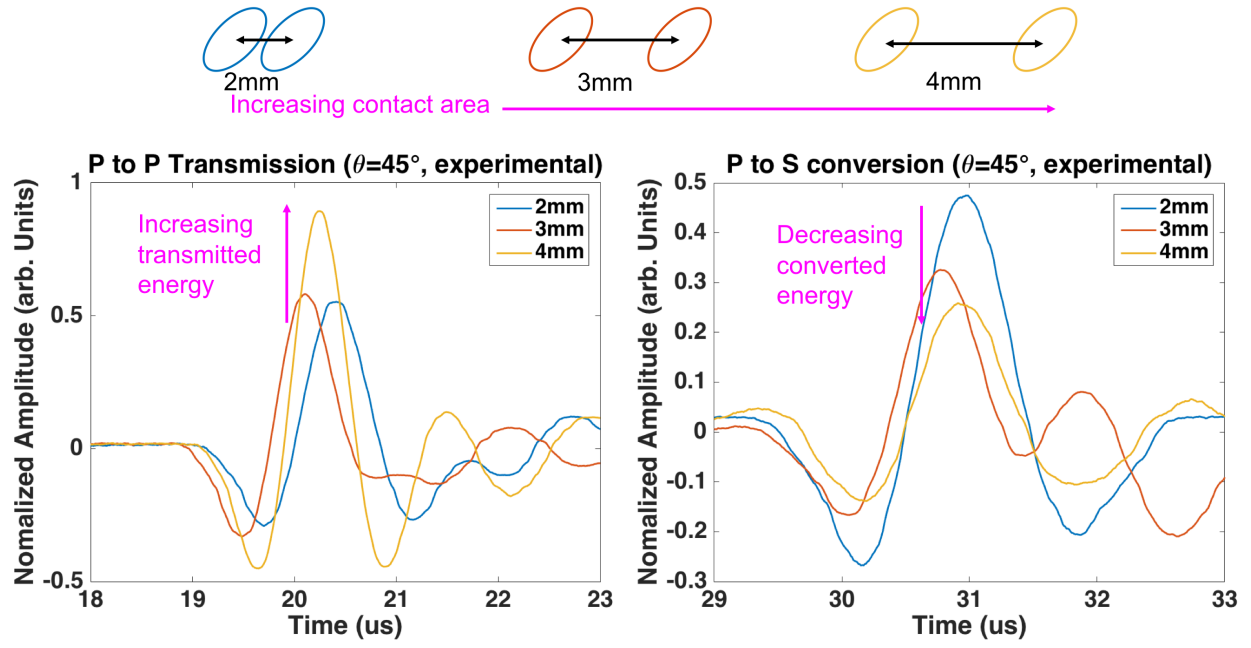


**Figure 6.15.** Experimentally measured P-P and P-S wave signals for elliptical voids with the same oriented angle ( $45^\circ$ ) but different void spacing.

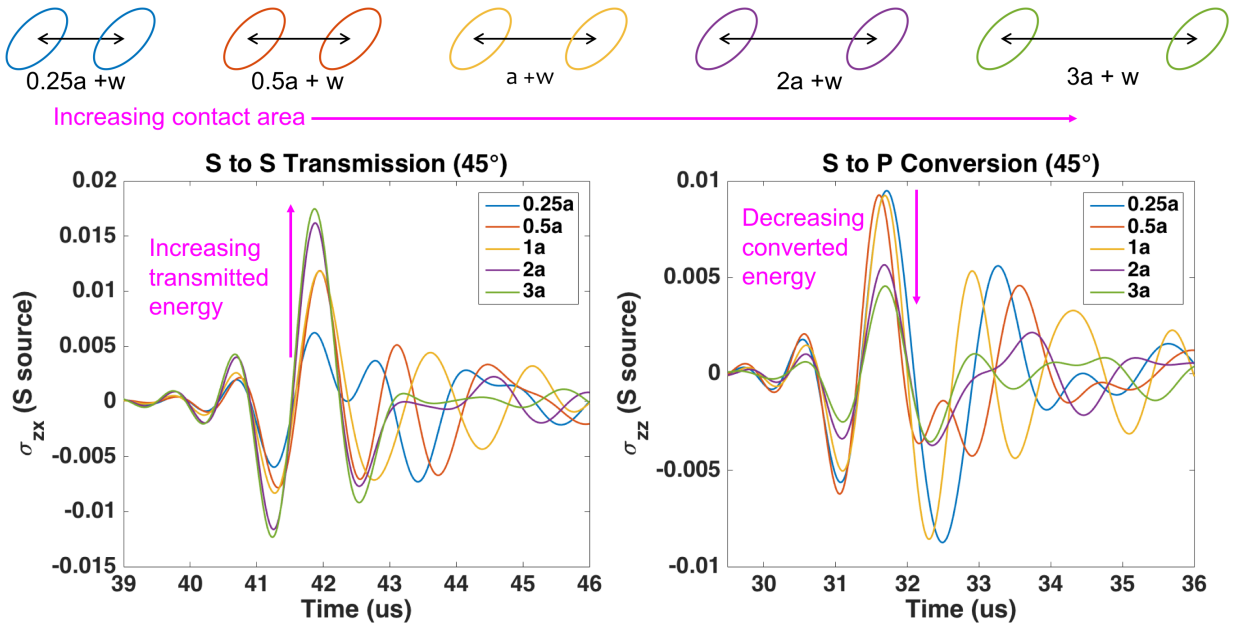


**Figure 6.16.** Simulation results of S-S and S-P wave signals for elliptical voids with the same oriented angle ( $45^\circ$ ) but different void spacing.

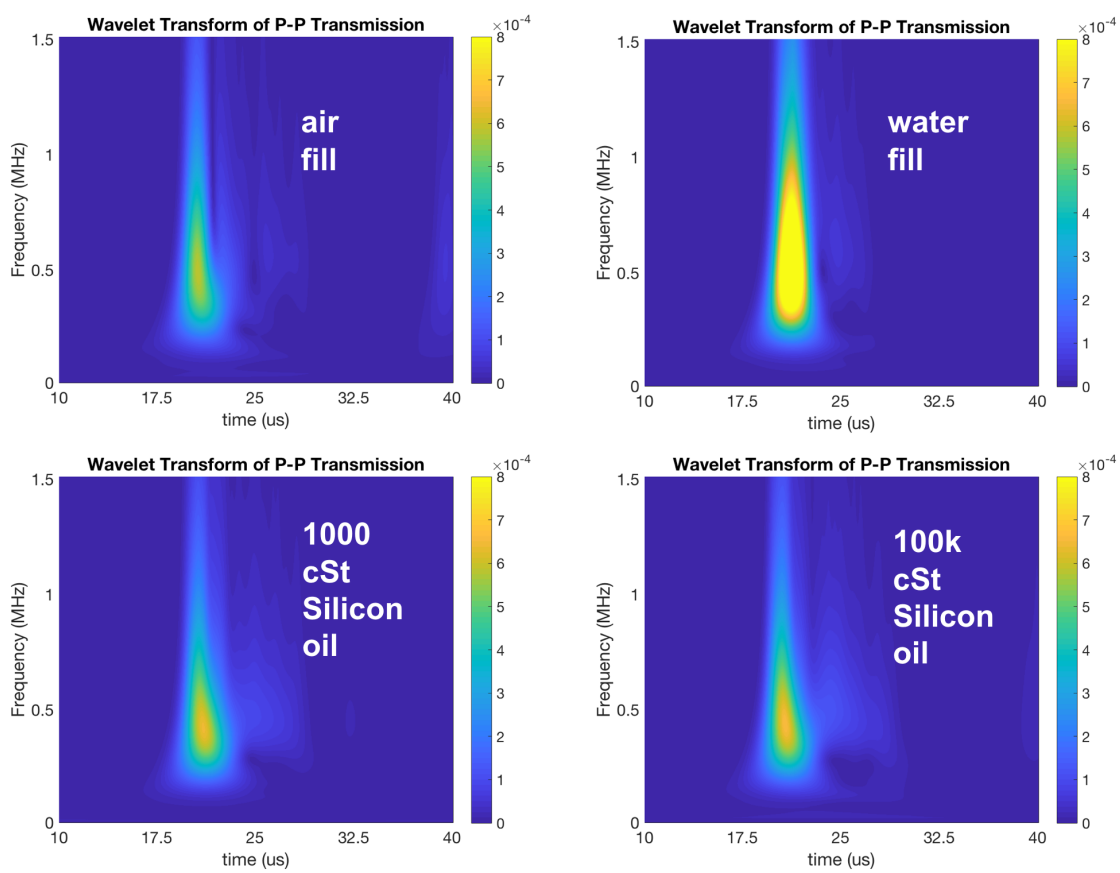


**Figure 6.17.** P-P transmission mode to fluid viscosity

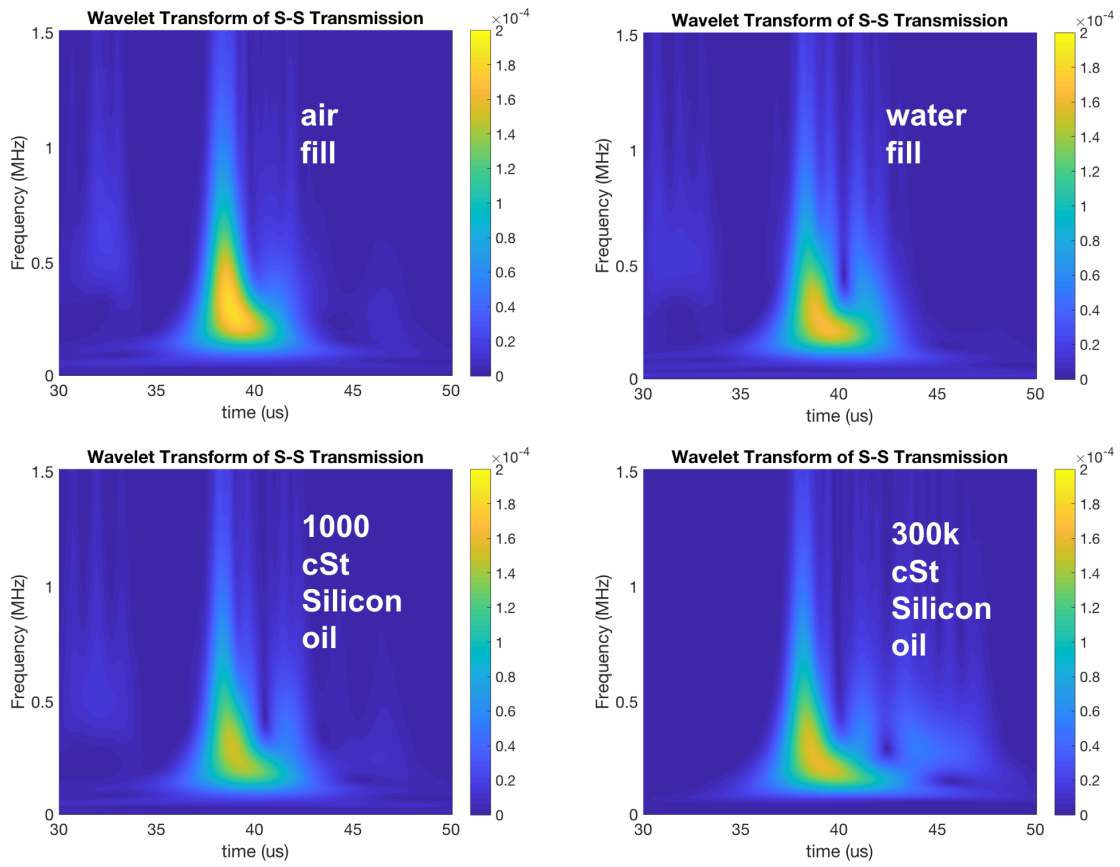


**Figure 6.18.** S-S transmission mode to fluid viscosity

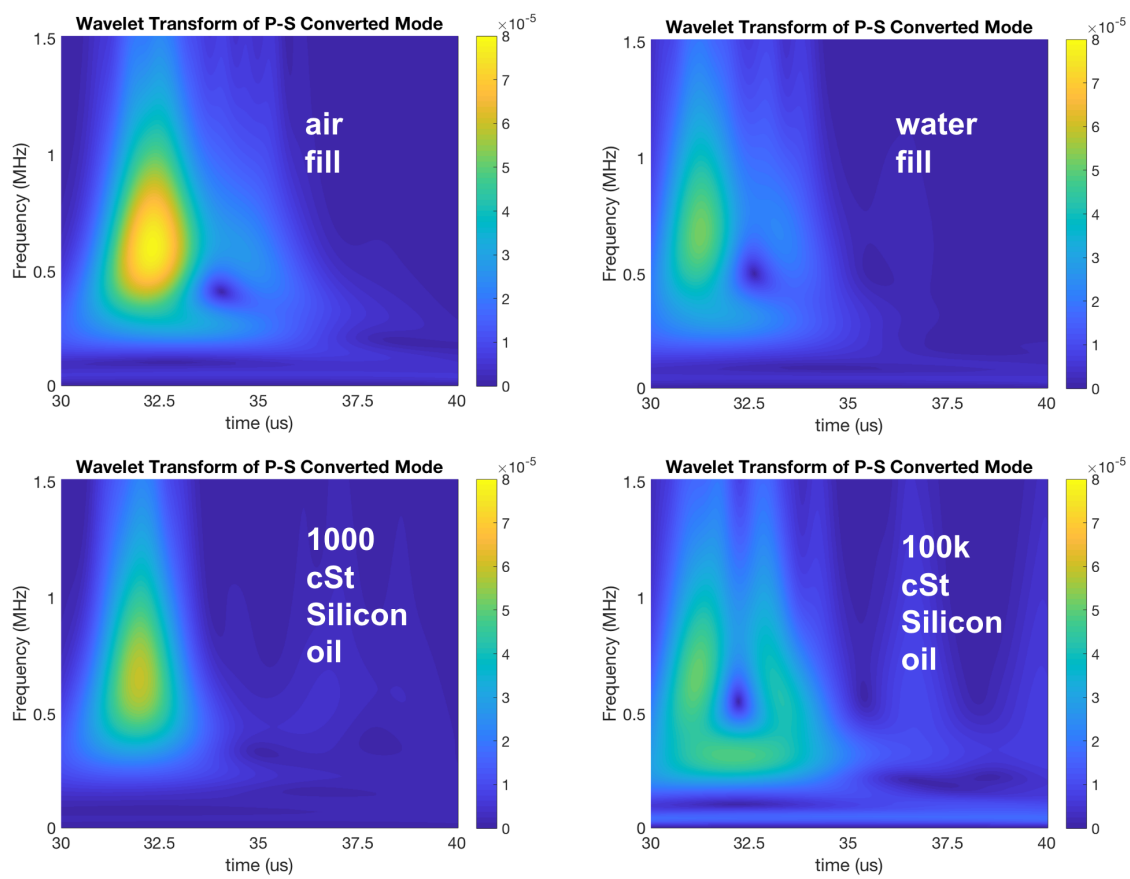


**Figure 6.19.** P-S converted mode to fluid viscosity

## 7. SUMMARY

The goal of experimental laboratory-based research is to design controlled experiments to illuminate fundamental physical behavior of materials subjected to controlled conditions. The field of laboratory rock physics is a fascinating field because rock is not a simple, uniform material, but is structurally and compositionally complex with features and heterogeneity occurring over a range of length scales. In this paper, we present several short examples of the use of crafted or geo-architected samples to explore and provide basic insight into contribution of microscale texture and structure on macro-scale measurements.

Geo-architected and analog gypsum samples enabled exploration of the effect of layer and mineral texture orientations on peak load achieved as a tensile fracture was induced. Additional testing has shown that the observed trends in peak failure load are consistent in terms the ranking of peak strength and the relative orientation between the layers and mineral texture. The greatest failure loads where obtained when the mineral texture direction was perpendicular to the fracture plane, and the smallest when the layering is parallel to the fracture plane. The 3D printed and cast gypsum samples exhibit some variability but less variation than that observed in natural rock samples.

One goal of laboratory-based research is to designed controlled experiments to elucidate and quantify the physical behavior of materials in response to physical and chemical perturbation. When working on rock, the most difficult aspect to control is the uniformity or repeatability of sample composition and structure of natural rock samples. This makes identification of the contributions to behavior from specific microstructural features difficult. Here, the use of 3D printed rock was instrumental in unraveling the complexity and heterogeneity observed in fracture formation. It enabled directional control of the in-layer mineral fabric, in layered samples, and in a repeatable manner. From these controlled samples, it was determined that anisotropy in 3D printed rock can rise from two sources: layering and direction of mineral growth. Peak failure loads were found to depend on the relative orientations among the loading direction, the layering and mineral fabric. Peak loads during tensile failure (Mode I) were the smallest when the layering was oriented parallel to the fracture plane, and greatest when the mineral growth direction is perpendicular to the fracture

plane. Whether the surface roughness of the induced tensile crack is isotropic or anisotropic depended on both the layering and mineral texture directions relative to the direction of fracture propagation. For mixed Mode I-II cases, it was discovered that the fracture toughness and roughness findings were unchanged when Mode II is introduced. However, fracture path was influenced by the bedding and mineral fabric directions, when mode II loading is introduced. When Mode III is introduced, the local properties of the fracture surfaces remained the same. However, as the notch rotates away from the long axis of the notch, the contribution to failure from the Mode III component increases, which leads to an increase in the area of the region of twisting and to a smaller region that exhibits pure Mode I behavior. The bedding and in-layer mineral fabric orientations controls the small scale properties of the fracture surface while the general shape of the fractures determined by the different modes also differed for different bedding and in-layer mineral fabric relative orientations.

3D printed gypsum (3DP) samples were also used to determine the effect of relative orientation between the microfabric and the layering on UCS values and the occurrence and number of acoustic emissions throughout the loading cycle. Samples where both the layering and gypsum texture were oriented parallel to the loading direction exhibited the largest values of UCS. While the lowest UCS values were observed for samples with bedding layers oriented  $45^\circ$  to the applied load. Unlike the CG (cast gypsum) samples, no axial splitting was observed among the 3DP samples. Irrespective of the orientation of the layers and texture, all samples exhibited a single major crack that spanned the entire length of the sample, inclined to the direction of loading. Samples with bedding oriented  $45^\circ$  to the load failed along the bedding planes, breaking into two pieces with the smoothest failure surfaces as determined from laser profilometry. Examination of the AE signal amplitude distribution in time for post-peak loading revealed that a longer period of AE events correlated with more ductile behaviors and the resultant fracture surfaces were rougher than for narrow AE distributions.

3D printing was also used to create samples with fractures with oriented voids to study compressional to shear (P-to-S) conversions for a range of orientations. The convenience of 3D printing enabled precision and easy fabrication of samples with voids in all kind of conditions so that the effect of geometry and fluids on energy partitioning. A simulation



study was also conducted and compared to experiments so that an understanding of the prediction of fracture property by seismic testing can be applied in other cases with more complicated fractures. The observed energy partitioning matched the computed compliances obtained from discontinuous Galerkin simulations. Information on local fracture geometry and fluid flowing through is contained in the far-field waves, and P-to-S converted modes were most sensitive to fluid viscosities.

My thesis work discovered that microstructural and failure modes control fractures surface roughness. This is important because fracture surface roughness defines the void geometry and contact area of a fracture which affects fluid flow. This research demonstrates the importance of understanding the mineralogy of sample and the failure mode to design successful subsurface strategies to maximize production potential from fractures. My research also found that the roughness of the fracture surface can be inferred from acoustic emissions, with smoother surfaces resulting in fewer measurable emissions. This work shows the potential of using acoustic emissions in the laboratory or induced seismicity in field to obtain information on the geometry of the fracture. Another outcome of my research was the acquisition of a laboratory benchmark data set to study damage evolution in brittle-ductile material. The goal is to provide numerical modelers with a calibration data set for their computational approaches. This data set is available to the community and can be found at <https://purr.purdue.edu/publications/3905/1> [43].

Future work should focus on improved methods for fracture location in anisotropic rock from interpretation of acoustic emissions. AE localization technique was compared to that observed from reconstructed X-ray computed tomography images, and error occurred due the anisotropic properties of the samples. Improved location methods are needed to include the velocity anisotropy of the sample for a better prediction of fracture location. Future research needs to expand the theory and use different models for studying cross-coupling stiffness effects for fractures in anisotropic media. The comparison of laboratory measurements and numerical simulation of P-to-S and S-to-P conversions for waves normally incident on fracture with oriented voids showed differences in the transmitted P-to-P and S-to-S wave amplitudes. The simulations were 2D with an isotropic background medium and a point source, while the experiments worked on a 3D dimensional geometry with plane wave sources and receivers. In

addition, the 3D printed samples were tilted during printing, and resulting the major axes for a transversely isotropic medium being neither parallel or perpendicular to the fracture plane. The 3D simulations for cross-coupling behavior for a fracture in an anisotropic medium with a plane wave source using a 3D DG program would enable modeling of both shear wave polarizations which is currently not possible with the 2D model.

## REFERENCES

- [1] S. R. Brown, “Fluid flow through rock joints: The effect of surface roughness,” *Journal of Geophysical Research*, vol. 92, pp. 1337–1347, 1987.
- [2] L. Pyrak-Nolte and D. D. Nolte, “Approaching a universal scaling relationship between fracture stiffness and fluid flow,” *Nature Communications*, vol. 7, Article Number 10663, 2016. DOI: [10.1038/ncomms10663](https://doi.org/10.1038/ncomms10663).
- [3] P. Lang, A. Paluszny, and R. Zimmerman, “Hydraulic sealing due to pressure solution contact zone growth in siliciclastic rock fractures,” *Journal of Geophysical Research Solid Earth*, vol. 120, pp. 4080–4101, 2015.
- [4] K. Spokas, C. Peters, and L. J. Pyrak-Nolte, “Influence of rock mineralogy on reactive fracture evolution in carbonate-rich caprocks,” *Environmental Science and Technology*, vol. 52, no. 17, pp. 10 144–10 152, 2018.
- [5] L. E. A. Jones and H. F. Wang, “Ultrasonic velocities in cretaceous shales from the williston basin,” *Geophysics*, vol. 46, pp. 288–297, 1981.
- [6] L. Vernik and A. Nur, “Ultrasonic velocity and anisotropy of hydrocarbon source rock,” *Geophysics*, vol. 57, no. 727-735, 1992.
- [7] C. M. Sayers, “Seismic anisotropy of shales,” *Geophysical Prospecting*, vol. 53, no. 667-676, 2005.
- [8] H.-R. Wenk, I. Lonardelli, F. Herman, K. T. Nihei, and S. Nakagawa, “Preferred orientation and elastic anisotropy of illite-rich shale,” *Geophysics*, vol. 72, no. 2, E69–E75, 2007.
- [9] X. Song, “Anisotropy of the earth’s inner core,” *Reviews in Geophysics*, vol. 35, pp. 297–313, 1997.
- [10] Y. Gao, Z. Liu, Q. Zeng, T. Wang, Z. Zhuang, and K.-C. Hwang, “Theoretical and numerical prediction of crack path in material with anisotropic fracture toughness,” *Engineering Fracture Mechanics*, vol. 180, pp. 330–347, 2017.
- [11] X. Zheng and Y. Wei, “Crack deflection in brittle media with heterogeneous interfaces and its application in shale fracking,” *Journal of the Mechanics and Physics of Solids*, vol. 101, pp. 235–249, 2017.
- [12] M. R. Chandler, P. G. Meredith, N. Brantut, and B. R. Crawford, “Fracture toughness anisotropy in shale,” *Journal of Geophysical Research*, vol. 121, pp. 1706–1729, 2016.

- [13] R. A. Schmidt, “Fracture mechanics of oil shale - unconfined fracture toughness, stress corrosion cracking, and tension test results,” in *The 18th U.S. Symposium on Rock Mechanics*, Balkema, 1977, 2A21–2A26.
- [14] N. D. Forbes Inskip, P. G. Meredith, M. R. Chandler, and A. Gudmunsson, “Fracture properties of nash point shale as a function of orientation to bedding,” *Journal of Geophysical Research - Solid Earth*, vol. 123, pp. 8428–8444, 2018.
- [15] L. Jiang, H. Yoon, A. Bobet, and L. J. Pyrak-Nolte, “Mineral fabric as a hidden variable in fracture formation in layered media,” *Scientific Reports*, vol. 10, no. 1, p. 2260, 2020. DOI: 10.1038/s41598-020-58793-y. [Online]. Available: <https://doi.org/10.1038/s41598-020-58793-y>.
- [16] B. N. Whittaker, R. N. Singh, and G. Sun, “Rock fracture mechanics. principles, design and applications,” 1992.
- [17] A. A. Griffith, “The phenomenon of rupture and flow in solids,” *Phil. Trans. Royal Soc. London, A*, vol. 221, pp. 163–198, 1920.
- [18] G. R. Irwin, “Analysis of stresses and strains near the end of a crack traversing a plate,” 1957.
- [19] B. McGinty, *Loading modes i, ii, iii*, <http://www.fracturemechanics.org/modes123.html>, Accessed: 2021-11-30.
- [20] R. K. Miller and P. McIntire, “Acoustic emission testing,” American Society for Non-destructive Testing., Tech. Rep., 1987.
- [21] C. Bates, D. Phillips, R. Grimm, and H. Lynn, “The seismic evaluation of a naturally fractured tight gas sand reservoir in the wind river basin, wyoming,” *Petroleum Geoscience*, vol. 7, no. 1, pp. 35–44, 2001.
- [22] R. D. Cicerone and M. N. Toksöz, “Fracture characterization from vertical seismic profiling data,” *Journal of Geophysical Research: Solid Earth*, vol. 100, no. B3, pp. 4131–4148, 1995.
- [23] F. D. Day-Lewis, J. W. Lane Jr, J. M. Harris, and S. M. Gorelick, “Time-lapse imaging of saline-tracer transport in fractured rock using difference-attenuation radar tomography,” *Water Resources Research*, vol. 39, no. 10, 2003.
- [24] C. S. Hartline, M. A. Walters, M. C. Wright, C. K. Forson, and A. J. Sadowski, “Three-dimensional structural model building, induced seismicity analysis, drilling analysis, and reservoir management at the geysers geothermal field, northern california,” *GRC Trans.*, vol. 39, pp. 603–614, 2015.

- [25] J. H. Queen, T. M. Daley, E. L. Majer, K. T. Nihei, D. L. Siler, and J. E. Faulds, “Surface reflection seismic and vertical seismic profile at brady’s hot springs, nv, usa,” in *Proceedings, forty-first workshop on geothermal reservoir engineering. Stanford: Stanford University*, 2016.
- [26] C. Petrovitch, D. D. Nolte, and L. Pyrak-Nolte, “Scaling of fluid flow versus fracture stiffness,” *Geophysical Research Letters*, vol. 40, pp. 2076–2080, 2013. DOI: [doi:10.1002/grl.50479](https://doi.org/10.1002/grl.50479).
- [27] C. L. Petrovitch, L. J. Pyrak-Nolte, and D. D. Nolte, “Combined scaling of fluid flow and seismic stiffness in single fractures,” *Rock mechanics and rock engineering*, vol. 47, no. 5, pp. 1613–1623, 2014.
- [28] L. J. Pyrak-Nolte, “Fracture specific stiffness: The critical link between the scaling behavior of hydro-mechanical coupling in fractures and seismic monitoring,” in *Science of Carbon Storage in Deep Saline Formations*, Elsevier, 2019, pp. 233–251.
- [29] R. E. Goodman, R. L. Taylor, and T. L. Brekke, “A model for the mechanics of jointed rock,” *Journal of Soil Mechanics & Foundations Div*, 1968.
- [30] R. Mindlin, “Waves and vibrations in isotropic, elastic plates,” *Structure Mechanics*, pp. 199–232, 1960.
- [31] K. Kendall and D. Tabor, “An ultrasonic study of the area of contact between stationary and sliding surfaces,” *Proceedings of the Royal Society of London. A. Mathematical and Physical Sciences*, vol. 323, no. 1554, pp. 321–340, 1971.
- [32] M. Schoenberg, “Elastic wave behavior across linear slip interfaces,” *The Journal of the Acoustical Society of America*, vol. 68, no. 5, pp. 1516–1521, 1980.
- [33] M. Schoenberg, “Reflection of elastic waves from periodically stratified media with interfacial slip,” *Geophysical Prospecting*, vol. 31, no. 2, pp. 265–292, 1983.
- [34] C. Kitsunezaki, “Behavior of plane elastic waves across a plane crack,” *Journal of the Mining College, Akita University. Ser. A, Mining geology*, vol. 6, no. 3, pp. 173–187, 1983.
- [35] L. J. Pyrak-Nolte and N. G. Cook, “Elastic interface waves along a fracture,” *Geophysical Research Letters*, vol. 14, no. 11, pp. 1107–1110, 1987.
- [36] L. J. Pyrak-Nolte, L. R. Myer, and N. G. Cook, “Transmission of seismic waves across single natural fractures,” *Journal of Geophysical Research: Solid Earth*, vol. 95, no. B6, pp. 8617–8638, 1990.
- [37] L. J. Pyrak-Nolte, L. R. Myer, and N. G. Cook, “Anisotropy in seismic velocities and

amplitudes from multiple parallel fractures,” *Journal of Geophysical Research: Solid Earth*, vol. 95, no. B7, pp. 11 345–11 358, 1990.

[38] S. Nakagawa, K. Nihei, and L. Myer, “Shear-induced conversion of seismic waves across single fractures,” *International Journal of Rock Mechanics and Mining Sciences*, vol. 37, no. 1-2, pp. 203–218, 2000.

[39] L. Jiang, H. Yoon, A. Bobet, and L. J. Pyrak-Nolte, “Effect of mineral orientation on roughness and toughness of mode i fractures,” in *53rd US Rock Mechanics/Geomechanics Symposium*, OnePetro, 2019.

[40] L. Jiang, H. Yoon, A. Bobet, and L. J. Pyrak-Nolte, “Fracture formation in layered synthetic rocks with oriented mineral fabric under mixed mode i and ii loading conditions,” in *55th US Rock Mechanics/Geomechanics Symposium*, OnePetro, 2021.

[41] L. Jiang, H. Yoon, A. Bobet, and L. J. Pyrak-Nolte, “Monitoring fracture formation in additively manufactured anisotropic rocks,” *Journal of Acoustic Emission*, vol. 36, S51–S51, 2019.

[42] L. Jiang and L. J. Pyrak-Nolte, “Elastics wave conversion from fractures with oriented voids,” in *52nd US Rock Mechanics/Geomechanics Symposium*, OnePetro, 2018.

[43] L. Jiang, H. Yoon, L. J. Pyrak-Nolte, A. Bobet, and J. Morris, *Calibration data set for damage mechanics challenge on brittle-ductile material*, Jan. 2022. DOI: [doi:/10.4231/QF39-Q924](https://doi.org/10.4231/QF39-Q924). [Online]. Available: <https://purrr.purdue.edu/publications/3905/1>.

[44] J.-W. Park and J.-J. Song, “Numerical method for the determination of contact areas of a rock joint under normal and shear loads,” *International Journal of Rock Mechanics and Mining Sciences*, vol. 58, pp. 8–22, 2013.

[45] A. Bobet and H. Einstein, “Fracture coalescence in rock-type materials under uniaxial and biaxial compression,” *International Journal of Rock Mechanics and Mining Sciences*, vol. 35, no. 7, pp. 863–889, 1998.

[46] L. Kong, M. Ostadhassan, M. Li, and N. Tamimi, “Can 3-d printed gypsum samples replicate natural rocks? an experimental study,” *Rock Mech. Rock Eng.*, 2018. DOI: [DOI-10.1007/s00603-018-1520-3](https://doi.org/10.1007/s00603-018-1520-3).

[47] D. F. Boutt, G. Grasselli, J. T. Fredrich, B. K. Cook, and J. R. Williams, “Trapping zones: The effect of fracture roughness on the directional anisotropy of fluid flow and colloid transport in a single fracture,” *Geophysical Research Letters*, vol. 33, no. 21, 2006.

- [48] C. Petrovitch, L. Pyrak-Nolte, and D. D. Nolte, “Combined scaling of fluid flow and seismic stiffness in single fractures,” *Rock Mechanics And Rock Engineering*, 2014. DOI: [DOI10.1007/s00603-014-0591-z](https://doi.org/10.1007/s00603-014-0591-z).
- [49] B. E. Hornby, L. M. Schwartz, and J. A. Hudson, “Anisotropic effective-medium modeling of the elastic properties of shales,” *Geophysics*, vol. 59, no. 10, pp. 1570–1583, 1994.
- [50] C. Sayers, “The elastic anisotropy of shales,” *Journal of Geophysical Research: Solid Earth*, vol. 99, no. B1, pp. 767–774, 1994.
- [51] H.-R. Wenk, I. Lonardelli, H. Franz, K. Nihei, and S. Nakagawa, “Preferred orientation and elastic anisotropy of illite-rich shale,” *Geophysics*, vol. 72, no. 2, E69–E75, 2007.
- [52] A. Tavallali and A. Vervoort, “Behaviour of layered sandstone under brazilian test conditions: Layer orientation and shape effects,” *Journal of Rock Mechanics and Geotechnical Engineering*, vol. 5, no. 5, pp. 366–377, 2013.
- [53] N. Dutler, M. Nejati, B. Valley, F. Amann, and G. Molinari, “On the link between fracture toughness, tensile strength, and fracture process zone in anisotropic rocks,” *Engineering Fracture Mechanics*, vol. 201, pp. 56–79, 2018.
- [54] M. Nejati, A. Aminzadeh, T. Driesner, and M. O. Saar, “On the directional dependency of mode i fracture toughness in anisotropic rocks,” *Theoretical and Applied Fracture Mechanics*, vol. 107, p. 102 494, 2020.
- [55] N. Singh and B. Middendorf, “Calcium sulphate hemihydrate hydration leading to gypsum crystallization,” *Progress in crystal growth and characterization of materials*, vol. 53, no. 1, pp. 57–77, 2007.
- [56] M. Dumbser and M. Käser, “An arbitrary high-order discontinuous galerkin method for elastic waves on unstructured meshes—ii. the three-dimensional isotropic case,” *Geophysical Journal International*, vol. 167, no. 1, pp. 319–336, 2006.
- [57] R. Ye, M. V. de Hoop, C. L. Petrovitch, L. J. Pyrak-Nolte, and L. C. Wilcox, “A discontinuous galerkin method with a modified penalty flux for the propagation and scattering of acousto-elastic waves,” *Geophysical Journal International*, vol. 205, no. 2, pp. 1267–1289, 2016.
- [58] S. Shao, C. Petrovitch, and L. Pyrak-Nolte, “Wave guiding in fractured layered media,” *Geological Society, London, Special Publications*, vol. 406, no. 1, pp. 375–400, 2015.
- [59] P. J. Bártolo and I. Gibson, “History of stereolithographic processes,” in *Stereolithography*, Springer, 2011, pp. 37–56.

- [60] N. Cook, “Natural joints in rock: Mechanical, hydraulic and seismic behaviour and properties under normal stress,” *International Journal of Rock Mechanics and Mining Sciences & Geomechanics Abstracts*, vol. 29, no. 3, pp. 198–223, 1992, ISSN: 0148-9062. DOI: [https://doi.org/10.1016/0148-9062\(92\)93656-5](https://doi.org/10.1016/0148-9062(92)93656-5). [Online]. Available: <https://www.sciencedirect.com/science/article/pii/0148906292936565>.
- [61] L. J. Pyrak-Nolte and J. P. Morris, “Single fractures under normal stress: The relation between fracture specific stiffness and fluid flow,” *International Journal of Rock Mechanics and Mining Sciences*, vol. 37, no. 1-2, pp. 245–262, 2000.



## A. MATLAB CODE

### A.1 Load and displacement reading

```
1 function [l, s]=loaddisplacement(f)
2
3 filename=horzcat('/Users/liyangjiang/Documents/Phys 590 Pyrak-
    Nolte/3PB 2018/',f, '.xlsx');
4 sheet = 1;
5
6 xlRange = 'B24:C200000';
7 %xlRange = 'D24:E200000';
8 z1Range = 'B18:B18';
9 z2Range = 'C18:C18';
10 C1Range = 'B16:B16';
11 C2Range = 'C16:C16';
12 E1Range='B17:B17';
13 E2Range='C17:C17';
14 %f1=-622218;
15 %f2=-0.7692;
16
17 M = xlsread(filename, sheet, xlRange);
18 z1=xlsread(filename, sheet, z1Range);
19 z2=xlsread(filename, sheet, z2Range);
20 f1=xlsread(filename, sheet, C1Range);
21 f2=xlsread(filename, sheet, C2Range);
22 E1=xlsread(filename, sheet, E1Range);
23 E2=xlsread(filename, sheet, E2Range);
24
25 l=f1*(M(:,1)-z1)*4.45/E1;%unit in N
```

```
26 s=f2*(M(:,2)-z2)*25.4/E2;%unit in mm
```

## A.2 Load and displacement plotting

```
1 function M=ppp(N)
2
3 f=horzcat('LOADING/',N);
4 [L,S]=loaddisplacement(f);
5 %G=gradient(L);
6 ix = find(L > 8, 1, 'first');
7 M=max(L)-min(L);
8 S=smooth(S);
9 %[m, ix]=max(L)
10 %plot(S(ix+1000:end)-S(ix),L(ix+1000:end)-min(L),'linewidth',2);
    hold on;
11 plot(S(ix:end-10)-S(ix),L(ix:end-10)-min(L),'linewidth',2);hold
    on;
12 %plot(S(ix:end)-S(ix),L(ix:end)-min(L),'-+','linewidth',0.1);hold
    on;
13 %
14 mini=min(S);
15 maxi=max(S);
16 s=size(S);
17 SS=0:(maxi-mini)/s(1):(maxi-mini);
18 %plot(SS(ix+1:end),L(ix:end)-min(L),'-+','linewidth',2);hold on;
19 %}
20 %plot(S(ix:end)-S(ix),L(ix:end)-min(L),'linewidth',1);hold on;
21 %scatter(S(ix:end)-S(ix),L(ix:end)-min(L));hold on;
```

```

22 %plot (S(ix:end)-S(ix),L(ix:end)-min(L),'-o','Visible','off','
    linewidth',2);hold on;
23 %plot (S(ix:end)-S(ix),'linewidth',2);hold on;
24 %plot (L(ix:end)-min(L),'--k','linewidth',2);hold on;
25 %plot (smooth(S-S(ix)),smooth(L-min(L)),'linewidth',2);hold on;
26 %{
27 [a b]=size(L);
28 x=1:1:a;
29 plot((x-ix)*0.0001,L-min(L),'linewidth',2);hold on;
30 %}
31 %{
32 B=[L,S];
33 snn=horzcat(N,'_LD.xlsx');
34
35 xlswrite(snn,B);
36 %}

```

### A.3 Fracture surface 3D plot

```

1 %clear Ag xx yy qx qy u
2 clear all;
3
4 SN='fCVT1';
5
6 filename=horzcat('/Users/liyangjiang/Documents/Phys 590 Pyrak-
    Nolte/3PB 2018/surface roughness/',SN,'_R.txt');
7
8 Ag=dlmread(filename);
9 %%%%%%%%%%%%%%%%%%%%%%%%%%%%%%%%%%%%%%%%%%%%%%%%%%%%%%%%%%%%%%%%%%%%%%%%%

```

```

10
11 %Ag(2:end,1)=Ag(2:end,1)-min(Ag(2:end,1));
12 %Ag(2:end,2)=Ag(2:end,2)-min(Ag(2:end,2));
13 Ag(1:end,1)=Ag(1:end,1)-min(Ag(1:end,1));
14 Ag(1:end,2)=Ag(1:end,2)-min(Ag(1:end,2));
15 Ag(1:end,3)=Ag(1:end,3)-max(Ag(1:end,3));
16
17 stepsize=0.1;
18 xposg=Ag(1:end,1);
19 yposg=Ag(1:end,2);
20 Ampg=Ag(1:end,3)*0.9969;
21
22 xxg=round(min(xposg)):stepsize:round(max(xposg));
23 yyg=round(max(yposg))-stepsize:round(min(yposg));
24
25 [qxg,qyg]=meshgrid(xxg,yyg);
26 for kk=1:length(xxg)
27     ug(kk,:)=Ampg(1+(kk-1)*length(yyg):kk*length(yyg),1);
28 end
29 for k=1:length(xxg)/2
30     ug(2*k,:)=flipud(ug(2*k,:)')';
31 end
32
33 ug(3:118,2:240)=ug(3:118,2:240)-max(max(ug(3:118,2:240)));
34 %
35 %20180816
36 fl=figure(1);
37 surf(qxg(2:240,3:118),qyg(2:240,3:118),ug(3:118,2:240)');
38 %

```

```

39 c = colorbar;
40 c.Label.String = 'Asperity (mm)';
41
42 %}
43 %surf(qxg,qyg,ug');
44 caxis([-15 0]);
45 xlim([0 12]);
46 ylim([0 25]);
47 zlim([-15 0]);
48 daspect([1 1 1]);
49 set(gca, 'FontSize',20);
50 %xlabel('Width Direction (mm)', 'Rotation',80);
51 %ylabel('Loading Direction (mm)', 'Rotation',-5);
52 %zlabel('Asperity (mm)', 'Rotation',90);
53
54 %xlabel('X axis (mm)', 'FontSize',14, 'FontWeight', 'bold');
55 %ylabel('Y axis (mm)', 'FontSize',14, 'FontWeight', 'bold');
56
57 sn=horzcat(SN, ' 3D');
58
59 %daspect([5 1 1]);
60
61 title(sn);
62 %title('Cast gypsum sample micro-slope histogram');
63 saveas(fl,sn, 'png');
64 %}
65
66 %
67 snn=horzcat(SN, '_SF.xlsx');

```

```

68 xlswrite(snn,ug');
69
70 %}

```

#### A.4 Fracture surface micro slope distribution

```

1 %clear Ag xx yy qx qy u
2 clear all;
3
4 SN='fIII601';
5
6 filename=horzcat('/Users/liyangjiang/Documents/Phys 590 Pyrak-
    Nolte/3PB 2018/surface roughness/',SN, '_R.txt');
7
8 Ag=dlmread(filename);
9
10 %Ag=dlmread('/Users/liyangjiang/Documents/Phys 590 Pyrak-Nolte/
    data raw/laser/20171116/SV3/sv3.txt');
11
12
13 %
    _____

14
15 Ag(1:end,1)=Ag(1:end,1)-min(Ag(1:end,1));
16 Ag(1:end,2)=Ag(1:end,2)-min(Ag(1:end,2));
17
18 stepsize=0.1;
19 xposg=Ag(1:end,1);

```

```

20 yposg=Ag(1:end,2);
21 Ampg=Ag(1:end,3)*0.9969;
22
23 xxg=min(xposg):stepsize:max(xposg);
24 %yyg=max(yposg):-stepsize:min(yposg);
25 yyg=min(yposg):stepsize:max(yposg);
26
27
28 [qxg,qyg]=meshgrid(xxg,yyg);
29 for kk=1:length(xxg)
30     ug(kk,:)=Ampg(1+(kk-1)*length(yyg):kk*length(yyg),1);
31 end
32 for k=1:length(xxg)/2
33     ug(2*k,:)=flipud(ug(2*k,:)')';
34 end
35 rmsg=rms(Ampg-min(Ampg));%root mean square
36
37
38 fg = fit([xposg, yposg], Ampg, 'poly11');
39 ag=fg(xposg,yposg);
40 [qxg,qyg]=meshgrid(xxg,yyg);
41 for kk=1:length(xxg)
42     Ug(kk,:)=ag(1+(kk-1)*length(yyg):kk*length(yyg),1);
43 end
44 for k=1:length(xxg)/2
45     Ug(2*k,:)=flipud(Ug(2*k,:)')';
46 end
47
48

```

```

49 B=(ug-Ug) ' ;
50 B=B(10:70,10:90) ;
51 [FX,FY]=gradient (B) ;
52 %%%%%%%%%%
53 C=FX;
54 %%%%%%%%%%
55 D=180*atan (10*C) / pi ;
56 E = D (:) ;
57 %%%%%%%%%%
58 C2=FY;
59 %%%%%%%%%%
60 D2=180*atan (10*C2) / pi ;
61 E2 = D2 (:) ;
62
63
64
65
66
67 AAg=Ampg-ag ;
68 rmscg=rms (AAg-min (AAg)) ;%root mean square after fixing the
    tilting
69 %{
70 xlabel ( 'X-Axis (mm) ' , 'FontSize ' ,16 , 'FontWeight ' , ' bold ' ) ;
71 ylabel ( 'Y-Axis (mm) ' , 'FontSize ' ,16 , 'FontWeight ' , ' bold ' ) ;
72 title ( 'sv3 ' ) ;
73 %}
74 %ylim ([0 18]) ;
75 %{
76 set (gca , ' fontsize ' ,14) ;

```



```

77 xbin=( -0.5:.005:0.5) ;
78 hist (C(:,1) ,xbin) ;
79 hold on;
80
81 for i=2:1:N
82 hist (C(:, i) ,xbin) ;
83 end
84
85 title ('SVC1') ;
86 xlim([ -0.2  0.2]) ;
87 %}
88
89 %{
90 fl=figure (1) ;
91 set (gca , ' fontsize ' ,14) ;
92 xbin=( -90:1:90) ;
93 [n1 ,x1]=hist (E(:,1) ,xbin) ;
94 hold on;
95
96 n1=(n1 ./sum(n1)) *100;
97 bar(x1 ,n1 , ' hist ' ) ;
98
99 title (SN) ;
100 xlim([ -90  90]) ;
101 ylim ([0  12]) ;
102 xlabel('Slope angle (degree) ' , 'FontSize ' ,16 , 'FontWeight ' , 'bold ' ) ;
103 ylabel(' Probability (%) ' , 'FontSize ' ,16 , 'FontWeight ' , 'bold ' ) ;
104 sn=horzcat (SN, ' micro-slope histogram (bar) ' ) ;
105 title (sn) ;

```

```

106 saveas(fl,sn,'png');
107 %}
108 %SS=[mean(E) max(E) min(E) median(E) mode(E) std(E) var(E)];
109
110 %surf(qxg,qyg,E);
111
112
113
114
115 %
116 %20180816
117 fl=figure(1);
118
119 xbin=(-90:1:90);
120 [n1,x1]=hist(E(:,1),xbin);
121 n1=(n1./sum(n1))*100;
122 %bar(x1,n1,'hist');
123 xbin2=(-90:1:90);
124 [n2,x2]=hist(E2(:,1),xbin2);
125 n2=(n2./sum(n2))*100;
126
127
128 plot(xbin,n1,'k','linewidth',2);hold on;
129 plot(xbin2,n2,'m','linewidth',2);
130 xlim([-90 90]);
131 ylim([0 15]);
132 set(gca,'FontSize',20);
133 xlabel('Slope angle (degree)','FontSize',26,'FontWeight','bold');
134 ylabel('Frequency (%)','FontSize',26,'FontWeight','bold');

```

```

135 legend('X direction','Y direction');
136
137 sn=horzcat(SN,' micro-slope histogram');
138 xticks([-90, -60, -30, 0, 30, 60, 90]);
139 %daspect([5 1 1]);
140
141 title(sn);
142 %title('Cast gypsum sample micro-slope histogram');
143 saveas(fl,sn,'png');
144 %}

```

## A.5 Fracture surface auto correction

```

1 function theta=SR_theta(N)% A: aperture, theta : micro slope 1:x
   2: y
2
3 filename=horzcat('/Users/liyangjiang/Documents/Phys 590 Pyrak-
   Nolte/3PB 2018/surface roughness/',N,'_R.txt');
4
5 Ag=dlmread(filename);
6
7 Ag(2:end,1)=Ag(2:end,1)-min(Ag(2:end,1));
8 Ag(2:end,2)=Ag(2:end,2)-min(Ag(2:end,2));
9
10 stepsize=0.1;
11 xposg=Ag(2:end,1);
12 yposg=Ag(2:end,2);
13 Ampg=Ag(2:end,3)*0.9969;
14

```

```

15 xxg=min(xposg):stepsize:max(xposg);
16 yyg=max(yposg):-stepsize:min(yposg);
17
18 xxg=min(xposg):stepsize:max(xposg);
19 %yyg=max(yposg):-stepsize:min(yposg);
20 yyg=min(yposg):stepsize:max(yposg);
21
22 [qxg,qyg]=meshgrid(xxg,yyg);
23 for kk=1:length(xxg)
24     ug(kk,:)=Ampg(1+(kk-1)*length(yyg):kk*length(yyg),1);
25 end
26 for k=1:length(xxg)/2
27     ug(2*k,:)=flipud(ug(2*k,:))';
28 end
29 rmsg=rms(Ampg-min(Ampg));%root mean square
30
31 fg = fit([xposg, yposg], Ampg, 'poly11');
32 ag=fg(xposg,yposg);
33 [qxg,qyg]=meshgrid(xxg,yyg);
34 for kk=1:length(xxg)
35     Ug(kk,:)=ag(1+(kk-1)*length(yyg):kk*length(yyg),1);
36 end
37 for k=1:length(xxg)/2
38     Ug(2*k,:)=flipud(Ug(2*k,:))';
39 end
40
41 B=(ug-Ug)';
42 B=B(6:195,4:100);
43 [FX,FY]=gradient(B);

```

```

44 %%%%%%%%%%
45 C=FX;
46 %%%%%%%%%%
47 D=180*atan(10*C)/pi;
48 E = D(:);
49 %%%%%%%%%%
50 C2=FY;
51 %%%%%%%%%%
52 D2=180*atan(10*C2)/pi;
53 E2 = D2(:);
54
55 xbin=(-90:1:90);
56 [n1,x1]=hist(E(:,1),xbin);
57 n1=(n1./sum(n1))*100;
58
59 xbin2=(-90:1:90);
60 [n2,x2]=hist(E2(:,1),xbin2);
61 n2=(n2./sum(n2))*100;
62
63 %{
64 ix1 = find(n1 > max(n1)/2, 1, 'first');
65 ix2 = find(n1(ix1:end) < max(n1)/2, 1, 'first');
66
67 iy1 = find(n2 > max(n2)/2, 1, 'first');
68 iy2 = find(n2(iy1:end) < max(n2)/2, 1, 'first');
69
70 theta=[ix2;iy2];%full width
71 %theta=[90-ix1;90-iy1];
72 %theta=[ix1+ix2-90;iy1+iy2-90];

```

```

73
74 %}
75 ix1 = find(n1 > max(n1)/2, 1, 'first');
76 ix2 = find(flip(n1(ix1:end)) > max(n1)/2, 1, 'first');
77 ix=length(n1(ix1:end))-ix2;
78
79 iy1 = find(n2 > max(n2)/2, 1, 'first');
80 iy2 = find(flip(n2(iy1:end)) > max(n2)/2, 1, 'first');
81 iy=length(n2(iy1:end))-iy2;
82
83 theta=[ix;iy];%full width

```

#### A.6 For Figure 3.5

```

1 H={SR_A('cH1'),SR_A('cH2'),SR_A('cH3'),SR_A('NHC1'), SR_A('NHC2')
   , SR_A('SHC3'),SR_A('PH3')};
2 HT={SR_A('cHT1'),SR_A('cHT2'),SR_A('cHT3'),SR_A('PHT1'),SR_A('
   NNHTC1'),SR_A('NNHTC2'),SR_A('NNHTC3'),SR_A('NNHTC4')};
3 VV={SR_A('cVV1'),SR_A('cVV2'),SR_A('cVV3'),SR_A('PVV1'),SR_A('
   NVVC1'),SR_A('NVVC2'),SR_A('NVVC3'),SR_A('SVVC1'),SR_A('SVVC2'
   ),SR_A('SVVC3')};
4 VVT={SR_A('cVVT1'),SR_A('cVVT2'),SR_A('cVVT3'),SR_A('NNVVT1'),
   SR_A('NNVVT2'),SR_A('NNVVT3'),SR_A('NNVVT4'),SR_A('PVVT1')
   };
5 V={SR_A('cV1'),SR_A('cV2'),SR_A('cV3'),SR_A('NVC1'),SR_A('NVC2'),
   SR_A('NVC3'),SR_A('SVC3'),SR_A('PV1'),SR_A('SVC1'),SR_A('SVC2'
   ),SR_A('SVC3')};
6 VT={SR_A('cVT1'),SR_A('cVT2'),SR_A('cVT3'),SR_A('bVT1'),SR_A('
   bVT2'),SR_A('bVT3'),SR_A('PVT1')};

```

```

7  G={SR_A( 'G11' ),SR_A( 'G12' ),SR_A( 'G22' ),SR_A( 'G24' ),SR_A( 'G31' ),
    SR_A( 'G33' ),SR_A( 'G34' ),SR_A( 'G41' ),SR_A( 'G42' ),SR_A( 'G43' ),
    SR_A( 'G44' ),SR_A( 'G52' ),SR_A( 'G53' ),SR_A( 'G54' ),SR_A( 'G61' ),
    SR_A( 'G62' ),SR_A( 'G63' ),SR_A( 'G82' ),SR_A( 'G83' ) };
8  MH=cat ( 3 ,H{:} ) ;H=mean(MH,3) ;
9  MHT=cat ( 3 ,HT{:} ) ;HT=mean(MHT,3) ;
10 MVV=cat ( 3 ,VV{:} ) ;VV=mean(MVV,3) ;
11 MVVT=cat ( 3 ,VVT{:} ) ;VVT=mean(MVVT,3) ;
12 MV=cat ( 3 ,V{:} ) ;V=mean(MV,3) ;
13 MVT=cat ( 3 ,VT{:} ) ;VT=mean(MVT,3) ;
14 MG=cat ( 3 ,G{:} ) ;G=mean(MG,3) ;
15
16  xlswrite( 'V.xlsx' ,V) ;
17  %}
18  %{
19  fl=figure (1) ;
20  imagesc(M) ;hold on ;daspect ([1 1 1]) ;
21  [M,c] =contour(M,6 , 'k' ) ;
22
23
24  c.LineWidth = 3;
25  %caxis ([0 , 1])
26  myColorMap = jet (256) ;
27
28  %myColorMap (1,:) = 1;
29  colormap (myColorMap) ;
30  colorbar ;
31  set (gca , 'FontSize' ,20) ;
32  xlabel ( 'Y Direction ' , 'FontSize' ,26 , 'FontWeight' , 'bold ' ) ;

```

```

33 ylabel('X Direction ','FontSize ',26,'FontWeight ','bold ');
34 set(gca,'XTick',[ ]);
35 set(gca,'YTick',[ ]);
36 sn=horzcat('Cast ','Autocorrelation ');
37
38 title(sn);
39 saveas(fl,sn,'png');
40 %}

```

## A.7 Fracture surface micro slope full width at half maximum

```

1 function M=SR_A(N)% A: aperture , theta : micro slope 1:x 2:y
2
3 filename=horzcat('/Users/liyangjiang/Documents/Phys 590 Pyrak-
    Nolte/3PB 2018/surface roughness/',N,'_B.txt');
4
5 Ag=dlmread(filename);
6 %%%%%%%%%%%%%%%%%%%%%%%%%%%%%%%%%%%%%%%%%%%%%%%%%%%%%%%%%%%%%%%%%%%%%%%%%
7
8 Ag(2:end,1)=Ag(2:end,1)-min(Ag(2:end,1));
9 Ag(2:end,2)=Ag(2:end,2)-min(Ag(2:end,2));
10
11 stepsize=0.1;
12 xposg=Ag(2:end,1);
13 yposg=Ag(2:end,2);
14 Ampg=Ag(2:end,3)*0.9969;
15
16 xxg=min(xposg):stepsize:max(xposg);
17 %yyg=max(yposg):-stepsize:min(yposg);

```



```

18 yyg=min(yposg):stepsize:max(yposg);
19
20 [qxg,qyg]=meshgrid(xxg,yyg);
21 for kk=1:length(xxg)
22     ug(kk,:)=Ampg(1+(kk-1)*length(yyg):kk*length(yyg),1);
23 end
24 for k=1:length(xxg)/2
25     ug(2*k,:)=flipud(ug(2*k,:))';
26 end
27 rmsg=rms(Ampg-min(Ampg));%root mean square
28
29 fg = fit([xposg, yposg], Ampg, 'poly11');
30 ag=fg(xposg,yposg);
31 [qxg,qyg]=meshgrid(xxg,yyg);
32 for kk=1:length(xxg)
33     Ug(kk,:)=ag(1+(kk-1)*length(yyg):kk*length(yyg),1);
34 end
35 for k=1:length(xxg)/2
36     Ug(2*k,:)=flipud(Ug(2*k,:))';
37 end
38
39 A=(ug-Ug)';
40
41 %%%%%%
42 %{
43 imageSizeX = 190;
44 imageSizeY = 100;
45 [columnsInImage,rowsInImage] = meshgrid(1:imageSizeX, 1:
    imageSizeY);

```

```

46 % Next create the circle in the image.
47 centerX = 95;
48 centerY = 50;
49 radius = 50;
50 circlePixels = (rowsInImage - centerY).^2 + (columnsInImage -
    centerX).^2 <= radius.^2;
51
52 %%%%%%%%%%%%%%%%%%%%%%%%%%%%%%%%%%%%%%%%%%%%%%%%%%%%%%%%%%%%%%%%%%%%%%%%%
53 B = A(6:195,4:103)'; % Initialize
54 % Mask
55 B(~circlePixels) = 0;
56
57 M = xcorr2(B);
58 %}
59 imageSizeX = 100;
60 imageSizeY = 100;
61 [columnsInImage, rowsInImage] = meshgrid(1:imageSizeX, 1:
    imageSizeY);
62 % Next create the circle in the image.
63 centerX = 50;
64 centerY = 50;
65 radius = 50;
66 circlePixels = (rowsInImage - centerY).^2 + (columnsInImage -
    centerX).^2 <= radius.^2;
67
68 %
69 %FOR CYLINDERS
70 B1 = A'; % Initialize
71 % Mask

```

```

72 B1(~circlePixels) = 0;
73 M = xcorr2(B1);
74 %}
75 %%%%%%%%%%%%%%%%%%%%%%%%%%%%%%%%%%%%%%%%%%%%%%%%%%%%%%%%%%%%%%%%%%%%%%%%%
76 %{
77 B1 = A(6:105,4:103)'; % Initialize
78 % Mask
79 B1(~circlePixels) = 0;
80
81 B2 = A(101:200,4:103)'; % Initialize
82 % Mask
83 B2(~circlePixels) = 0;
84
85 M1 = xcorr2(B1);
86 M2 = xcorr2(B2);
87 M=(M1+M2)/2;
88 %M(M==0) = nan;
89
90 %}

```

## A.8 For Figure 3.3

```

1 H=[SR_theta('cH1'),SR_theta('cH2'),SR_theta('cH3'),SR_theta('NHC1
   '), SR_theta('NHC2'), SR_theta('SHC3'),SR_theta('PH3')];
2 HT=[SR_theta('cHT1'),SR_theta('cHT2'),SR_theta('cHT3'),SR_theta('
   PHT1'),SR_theta('NNHTC1'),SR_theta('NNHTC2'),SR_theta('NNHTC3'
   ),SR_theta('NNHTC4')];

```

```

3 VV=[SR_theta( 'cVV1' ),SR_theta( 'cVV2' ),SR_theta( 'cVV3' ),SR_theta( '
    PVV1' ),SR_theta( 'NVVC1' ),SR_theta( 'NVVC2' ),SR_theta( 'NVVC3' ),
    SR_theta( 'SVVC1' ),SR_theta( 'SVVC2' ),SR_theta( 'SVVC3' )];
4 %VVT=[SR_theta( 'cVVT1' ),SR_theta( 'cVVT2' ),SR_theta( 'cVVT3' ),
    SR_theta( 'NNVVC1' ),SR_theta( 'NNVVC2' ),SR_theta( 'NNVVC3' ),
    SR_theta( 'NNVVC4' ),SR_theta( 'PVVT1' )];
5 VVT=[SR_theta( 'cVVT1' ),SR_theta( 'cVVT2' ),SR_theta( 'cVVT3' ),
    SR_theta( 'PVVT1' )];
6 V=[SR_theta( 'cV1' ),SR_theta( 'cV2' ),SR_theta( 'cV3' ),SR_theta( 'NVC1
    ' ),SR_theta( 'NVC2' ),SR_theta( 'NVC3' ),SR_theta( 'SVC3' ),SR_theta
    ( 'PV1' ),SR_theta( 'SVC1' ),SR_theta( 'SVC2' ),SR_theta( 'SVC3' )];
7 VT=[SR_theta( 'cVT1' ),SR_theta( 'cVT2' ),SR_theta( 'cVT3' ),SR_theta( '
    bVT1' ),SR_theta( 'bVT2' ),SR_theta( 'bVT3' ),SR_theta( 'PVT1' )];
8 G=[SR_theta( 'G11' ),SR_theta( 'G12' ),SR_theta( 'G22' ),SR_theta( 'G24'
    ),SR_theta( 'G31' ),SR_theta( 'G33' ),SR_theta( 'G34' ),SR_theta( '
    G41' ),SR_theta( 'G42' ),SR_theta( 'G43' ),SR_theta( 'G44' ),SR_theta
    ( 'G52' ),SR_theta( 'G53' ),SR_theta( 'G54' ),SR_theta( 'G61' ),
    SR_theta( 'G62' ),SR_theta( 'G63' ),SR_theta( 'G82' ),SR_theta( 'G83'
    )];
9
10 x=[mean(H' ),mean(HT' ),mean(VV' ),mean(VVT' ),mean(V' ),mean(VT' ),
    mean(G' )];
11
12 %stderror= std( m )./ sqrt( length( m ))
13 stderror=[std( H' )./ sqrt( length( H' )),std(HT' )./ sqrt(
    length( HT' )),std( VV' )./ sqrt( length( VV' )),std( VVT' )./
    sqrt( length( VVT' )),std( V' )./ sqrt( length( V' )),std( VT'
    )./ sqrt( length( VT' )),std( G' )./ sqrt( length( G' ))];
14

```

```

15 b1=bar(1,x(1)); hold on;
16 b2=bar(2,x(2)); hold on;
17 b3=bar(4,x(3)); hold on;
18 b4=bar(5,x(4)); hold on;
19 b5=bar(7,x(5)); hold on;
20 b6=bar(8,x(6)); hold on;
21 b7=bar(10,x(7)); hold on;
22 b8=bar(11,x(8)); hold on;
23 b9=bar(13,x(9)); hold on;
24 b10=bar(14,x(10)); hold on;
25 b11=bar(16,x(11)); hold on;
26 b12=bar(17,x(12)); hold on;
27 b13=bar(19,x(13)); hold on;
28 b14=bar(20,x(14)); hold on;
29 e=errorbar([1 2 4 5 7 8 10 11 13 14 16 17 19 20],x,stderror, ' . ');
30 %%%%%%%%%%
31 e.Color = [0 0 0];
32 e.LineWidth = 2;
33 b1.FaceColor = [0      0.4470      0.7410];
34 b2.FaceColor = [0      0.4470      0.7410];
35 b2.FaceAlpha = 0.3;
36
37 b3.FaceColor = [0.8500 0.3250 0.0980];
38 b4.FaceColor = [0.8500 0.3250 0.0980];
39 b4.FaceAlpha = 0.3;
40
41 b5.FaceColor = [      0.9290      0.6940      0.1250];
42 b6.FaceColor = [      0.9290      0.6940      0.1250];
43 b6.FaceAlpha = 0.5;

```

```

44
45 b7.FaceColor = [0.4940    0.1840    0.5560];
46 b8.FaceColor = [0.4940    0.1840    0.5560];
47 b8.FaceAlpha = 0.5;
48
49 b9.FaceColor = [0.4660    0.6740    0.1880];
50 b10.FaceColor = [0.4660    0.6740    0.1880];
51 b10.FaceAlpha = 0.5;
52
53 b11.FaceColor = [0.3010    0.7450    0.9330];
54 b12.FaceColor = [0.3010    0.7450    0.9330];
55 b12.FaceAlpha = 0.5;
56
57 b13.FaceColor = [0.6350    0.0780    0.1840];
58 b14.FaceColor = [0.6350    0.0780    0.1840];
59 b14.FaceAlpha = 0.5;
60
61 %%%%%%%%%%%%%%%%%%%%%%%%%%%%%%%%%%%%%%%%%
62 y=ylabel('Full Width Half Maximum (Angle)') ;
63 xlabel('Sample');
64
65 set(y, 'Units', 'Normalized', 'Position', [0, 0.5, 0]);
66 set(gca, 'fontweight', 'bold', 'FontSize', 18);
67 %title('');
68
69 set(gca, 'XTick', [1.5 4.5 7.5 10.5 13.5 16.5 19.5])
70 set(gca, 'XTickLabel', {'H', 'Halt', 'VV', 'VValt', 'V', 'Valt', 'Cast '
    });

```

## A.9 Digital image correlation (DIC) information extraction from analyzed data

```
1 %20180326 Liyang Jiang_ Purdue
2 %RD : raw data extract
3 %AD : analyzed data (show gradient)
4 %c : conversion between pixel and actual size
5 %k : the threshold to determine a crack
6 function [RD,AD]=dic ( filename , xi , xf , yi , yf )
7 %RD is the raw x y displacement; AD is analyzed cracking
8 M=importdata ( filename );%import data
9 %remesh
10 xpos=M.data ( 1:end , 1 ) ;
11 ypos=M.data ( 1:end , 2 ) ;
12 xdis=M.data ( 1:end , 3 ) ;
13 %(1:end,4) is vertical displacement (1:end,3) is horizontal
    displacement
14 xx=min ( xpos ) : 3 : max ( xpos ) ;
15 yy=min ( ypos ) : 3 : max ( ypos ) ;
16 [ ~ , b ] = size ( xx ) ;
17 [ ~ , d ] = size ( yy ) ;
18 Xdis=zeros ( b , d ) ;
19 for kk=1:length ( yy )
20     Xdis ( : , kk ) = xdis ( 1 + ( kk - 1 ) * length ( xx ) : kk * length ( xx ) , 1 ) ;
21 end
22 RD=Xdis ( xi : xf , yi : yf ) ;
23 %plot ( RD ( : , 250 ) )
24 lx=xf-xi ;
25 ly=yf-yi ;
26 %%%%%%%%%%%%%%%%%%%%%%%%%%%%%%%%%AD
27 AD=zeros ( lx , ly ) ;
```

```

28 c=0.5;%threshold
29 for j=1:1:ly
30     for i=50:1:lx-80
31         if RD(i,j)>RD(i-10,j)+c
32             AD(i-5,j)=(RD(i,j)+RD(i-5,j))/2;
33         else
34             AD(i-5,j)=0;
35         end
36     end
37 end

```

## A.10 DIC of single image

```

1 %%%%%%%%%Liyang Jiang%%%%%%%% PURDUE%%%
2 %%20190411
3 %This code is used to plot displacement in x or y direction in 2D
  domain
4 clear all
5
6 f='/Users/liyangjiang/Downloads/B00803.dat';%altered
7 %f='/Users/liyangjiang/Downloads/B00800.dat';%unaltered
8
9 %%%%%%%%%%aaaaaaaaaaaaaaaa%%%%%%%%%
10 %this part is to get rid of the nonzeros in the matrix
11 M=importdata(f);%import data
12 %remesh
13 xpos=M.data(1:end,1);
14 ypos=M.data(1:end,2);
15 xdis=M.data(1:end,4);

```



```

16 %%%%%%%%%%%%%%%%%%%%%%%%%%%%%%%%%important%%%%%%%%
17 %(1:end,4) is vertical displacement (1:end,3) is horizontal
    displacement
18 % you need to make sure dic.m file has the same setup in line 11
19 xx=min(xpos):3:max(xpos);
20 yy=min(ypos):3:max(ypos);
21 for kk=1:length(yy)
22     Xdis(:,kk)=xdis(1+(kk-1)*length(xx):kk*length(xx),1);
23 end
24 lx=size(nonzeros(Xdis(:,200)));lx=lx(1,1);
25 xi = find(Xdis(:,200),1);
26 xf =lx+xi;
27
28 ly=size(nonzeros(Xdis(200,:)) );ly=ly(1,1);
29 yi = find(Xdis(200,:),1);
30 yf=ly+yi;
31
32 %%%%%%%%%%%%%%%%%%%%%%%%%%%%%%%%%%%%%%%%%%%%%%%%%%%%%%%%%
33
34 %extract information
35 [RD,AD] = dic(f,xi+5,xf-5,yi+5,yf-5);
36 %%%%%%%%%%%%%%%%%%%%%%%%%%%%%%%%%%%%%%%%%%%%%%%%%%%%%%%%%plot raw data
37     c=2*25.4/(3*lx);%converting from pixel to mm (here,2 inches
        in x)
38     X=0:3*c:3*c*lx;
39     Y=0:3*c:3*c*ly;
40     RD=RD*c;%displacement in unit mm
41     %
42     [XXX,YYY]=size(RD);

```

```

43
44     %zlevel=mini:(maxi-mini)/40:maxi;
45     contourf(X(1,1:XXX),Y(1,1:YYY),flipud(RD')));
46     %caxis([-0.4 0.4]);
47 % you need to adjust the zlevel numbers and range
48 %to get a desired picture with nice contrast
49     colorbar;
50     cc = colorbar;
51     cc.Label;
52     cc.Label.String = 'horizontal displacement (mm)';
53     cc.Label.FontSize = 18;
54
55     xlabel('Horizontal direction (mm)','fontweight','b','fontsize'
56           ',18);
57     ylabel('Vertical direction (mm)','fontweight','b','fontsize'
58           ',18);
59     set(gca,'fontweight','b','fontsize',16);
60
61 %{
62 %plot displacements in different X and Y locations
63 plot(RD(:,250,1));hold on;
64 plot(RD(:,250,10));hold on;
65 plot(RD(:,250,50));
66 plot(RD(:,250,150));
67 plot(RD(:,250,250));
68 plot(RD(:,250,325));
69 xlabel('Time','FontSize',14);
70 ylabel('Y dis (mm)','FontSize',16);
71 set(gca,'fontweight','bold','FontSize',14);

```

```

70 title('VERTICAL LINE');
71
72 plot(RD(:,5,225));hold on;
73 plot(RD(:,50,225));hold on;
74 plot(RD(:,100,225));
75 plot(RD(:,150,225));
76 plot(RD(:,250,225));
77 plot(RD(:,290,225));
78 xlabel('Time','FontSize',14);
79 ylabel('Y dis (mm)','FontSize',16);
80 set(gca,'fontweight','bold','FontSize',14);
81 title('HORIZONTAL LINE');
82 %}

```

## A.11 DIC synced with load displacement data and seismic waves

```

1
2 time=10:0.01:59.99;
3 time=time';
4 SN='GB31';
5 f=horzcat('/Volumes/Liyang8TB1/20201122/',SN,'/',SN,'_');
6
7 fn=488;
8 %%%%%%%%% L D %%%%%%%%%
9 fload=horzcat('LOADING/',SN);
10 [L,S]=loaddisplacement(fload);
11 ix = find(L > 3, 1, 'first');
12
13 %%%%%%%%% SEISMIC %%%%%%%%%

```

```

14 tt=zeros (1 ,fn-1);
15 ll=zeros (1 ,fn-1);
16 ss=zeros (1 ,fn-1);
17
18     j=1;
19     filename=horzcat (f ,num2str (j) , '.txt ');
20     M=dlmread (filename);
21     M=M(1:10000 ,1);
22     m=max(M) ;
23 for i =1:1:fn-1
24
25     filename=horzcat (f ,num2str (i) , '.txt ');
26     M=dlmread (filename);
27     M=M(1:10000 ,1);
28     tt (i)=max(M)/m;
29     ll (i)=L(10*i);
30     ss (i)=S(10*i);
31 end
32
33 %%%%%%%%%%%%%%%%%%%%%%%%%%%%%%%%%%%%%%%%%%%%%%%%%%%%%%%%%%%%%%%%%%%%%%%%%
34 for i =30:1:fn-3
35 %data filename
36
37 %%%%%%%%%%%%%%%%%%%%%%%%%%%%%%%%%%%%%%%%%%%%%%%%%%%%%%%%%%%%%%%%%%%%%%%%% plotting %%%%%%%%%
38 FigH = figure ( 'Position' , get(0 , 'ScreenSize' ) , 'visible' , 'off
        ' );
39
40 % dic plot
41 %%%%%%%%%%title%%%%%%%%

```

```

42         t=0.2*3*i;
43         til=horzcat(num2str(L(LL(i))), ' N (' ,num2str(t), ' s) ');
44         title(til);
45
46         %%%%%%%%% load displacement plot %%%%%%%%%
47 subplot(2,1,1);
48
49 plot(S(ix:end)-S(ix),L(ix:end)-min(L), 'linewidth',2);hold on;
50 l1=line([ S(LL(i))-S(ix) S(LL(i))-S(ix)], [0 300], 'LineWidth',2)
        ;hold off;
51 l1.Color = 'black';
52 xlabel('Displacement (mm)')
53 ylabel('Load (N)') ;
54 xlim([0 0.4]);
55 ylim([0 300]);
56 daspect([1 1000 1]);
57 set(gca, 'fontweight','bold','FontSize',14);
58 title('Load Displacement Curve');
59
60         %%%%%%%%% seismic plot %%%%%%%%%
61 subplot(2,1,2);
62 xs=0:0.6:(FN-1)*0.6;
63 plot(xs',(tt-min(tt))/(tt(1)-min(tt)), 'linewidth',2);hold on;
64 ylim([0 1.2]);
65 xlim([0 900]);
66 daspect([600 1 1]);
67 xlabel('Time (s)')
68 ylabel('Amplitude Ratio') ;
69 title('P-P Transmission Amplitude');

```

```

70 set(gca, 'fontweight', 'bold', 'FontSize', 14);
71 hold on;
72 l2=line([ xs(SS(i)) xs(SS(i))], [0 1.2], 'LineWidth', 2); hold off;
73 l2.Color = 'black';
74
75 %%%%%%%%% %%%%%%%%% %%%%%%%%% %%%%%%%%% %%%%%%%%% %%%%%%%%%
76 %Saving parameters
77
78 savename=horzcat('/Users/liyangjiang/Documents/Phys 590 Pyrak
    -Nolte/DICS/', SN, '/', num2str(fnum));
79 saveas(FigH, savename, 'png');
80 close all;
81 %}
82 end
83
84 %
85 x=1:1:fn-1;
86 [hAx, hLine1, hLine2] =plotyy(x, tt, x, ll-min(ll));
87 hLine1.LineWidth = 2;
88 hLine2.LineWidth = 2;
89 title(SN);
90 hLine1.Color = 'black';
91 hLine2.Color = 'red';
92 set(hAx, {'ycolor'}, {'k'; 'r'})
93 xlabel('Time (s)', 'FontSize', 14);
94 ylabel(hAx(2), 'Load (N)', 'FontSize', 16); % left y-axis
95 ylabel(hAx(1), 'Transmission amplitude ratio', 'FontSize', 16) ;
96 ylim(hAx(2), [0 420]);
97 ylim(hAx(1), [0 1.2]);

```

```
98 %}
```

## A.12 Monitor honey coupling of transducers for 24 hours

```
1 N=1052;
2 b1=zeros(1,N);
3 for fnum=1:N
4     filename=horzcat('/Users/liyangjiang/Documents/Phys 590 Pyrak-
        Nolte/data raw/20180604/RD0_D',num2str(fnum));
5     Matrix1=dlmread(filename); %open the file defined above and
        store values
6     b1(1,fnum)=max(abs(Matrix1));
7     clear filename;%clear this for the next time through.
8 end
9 plot(b1);
```

## A.13 Experimental seismic waves (chapter 6)

```
1 RD0_RPP=dlmread('/Users/liyangjiang/Documents/Phys 590 Pyrak-
    Nolte/data raw/20180614/RD0_RPP0');
2 RD0_DPP=dlmread('/Users/liyangjiang/Documents/Phys 590 Pyrak-
    Nolte/data raw/20180614/RD0_DPP0');
3 RD0_EPP=dlmread('/Users/liyangjiang/Documents/Phys 590 Pyrak-
    Nolte/data raw/20170719/S0Mpp30');
4
5 RD0_IPP=dlmread('/Users/liyangjiang/Documents/Phys 590 Pyrak-
    Nolte/data raw/20180614/2/RD0_IPP0');
6 RD0_EIPP=dlmread('/Users/liyangjiang/Documents/Phys 590 Pyrak-
    Nolte/data raw/20170727/S0Ipp1003');
```

```

7
8
9 RD0_RSS=dlmread( '/Users/liyangjiang/Documents/Phys 590 Pyrak-
    Nolte/data raw/20180615/RD0_RSS0' );
10 RD0_DSS=dlmread( '/Users/liyangjiang/Documents/Phys 590 Pyrak-
    Nolte/data raw/20180615/RD0_DSS0' );
11 C0_MSS=dlmread( '/Users/liyangjiang/Documents/Phys 590 Pyrak-Nolte
    /data raw/20180615/C0_MSS0' );
12
13 RD0_ISS=dlmread( '/Users/liyangjiang/Documents/Phys 590 Pyrak-
    Nolte/data raw/20180615/RD0_ISS0' );
14 C0_IPP=dlmread( '/Users/liyangjiang/Documents/Phys 590 Pyrak-Nolte
    /data raw/20180615/C0_ISS0' );
15 R2=max( C0_IPP )/max( RD0_ISS );
16 %R=1.1
17 %{
18 %20180614
19 time=15.01:0.01:50;
20 time=time';
21 plot( time, smooth( RD0_DPP(1:3500) ), 'LineWidth', 1.5 );
22 hold on;
23 plot( time, smooth( RD0_EPP(1:3500)/R ), 'LineWidth', 1.5 );
24 plot( time, smooth( RD0_RPP(1:3500) ), 'LineWidth', 1.5 );
25 xlabel( 'Time (us)' );
26 ylabel( 'Nomalized Amplitude (arb. Units)' );
27 set( gca, 'fontweight', 'bold', 'FontSize', 20 );
28 legend( 'Diamond', 'Ellipse', 'Rectangle' )
29 title( 'P to P Transmission ( \theta=0\circ, experimental ) );
30 xlim( [18 23] );

```



```

31 %}
32
33 %{
34 %20180615
35 time=15.01:0.01:50;
36 time=time';
37 plot(time,smooth(RD0_DSS(1:3500)),'LineWidth',1.5);
38 hold on;
39 plot(time,smooth(C0_MSS(1:3500)/R2),'LineWidth',1.5);
40 plot(time,smooth(RD0_RSS(1:3500)),'LineWidth',1.5);
41 xlabel('Time (us)');
42 ylabel('Nomalized Amplitude (arb. Units)');
43 set(gca,'fontweight','bold','FontSize',20);
44 legend('Diamond','Ellipse','Rectangle')
45 title('S to S Transmission (\theta=0\circ, experimental)');
46 xlim([38 48]);
47 %}

```

#### A.14 Stimulated seismic waves (chapter 6)

```

1
2 M=zeros(60001,6);
3 for i = 1:1:11
4     filename=horzcat('/Users/liyangjiang/Documents/Phys 590 Pyrak
        -Nolte/B/Liyang/outputLccms01/measurementLccms01_source',
        num2str(53+i),'.dat');
5     A=load (filename);M=M+A;
6 end
7 P0_JLY=M/11;clear M A;

```

```

8
9 M=zeros(60001,6);
10 for i = 1:1:11
11     filename=horzcat('/Users/liyangjiang/Documents/Phys 590 Pyrak
        -Nolte/B/Liyang/outputLccms02/measurementLccms02_source',
        num2str(53+i), '.dat');
12     A=load (filename);M=M+A;
13 end
14 S0_JLY=M/11;clear M A;
15
16 M=zeros(60001,6);
17 for i = 1:1:11
18     filename=horzcat('/Users/liyangjiang/Documents/Phys 590 Pyrak
        -Nolte/B/Liyang/outputLccms03/measurementLccms03_source',
        num2str(53+i), '.dat');
19     A=load (filename);M=M+A;
20 end
21 P45_JLY=M/11;clear M A;
22
23 M=zeros(60001,6);
24 for i = 1:1:11
25     filename=horzcat('/Users/liyangjiang/Documents/Phys 590 Pyrak
        -Nolte/B/Liyang/outputLccms04/measurementLccms04_source',
        num2str(53+i), '.dat');
26     A=load (filename);M=M+A;
27 end
28 S45_JLY=M/11;clear M A;
29
30 M=zeros(60001,6);

```

```

31 for i = 1:1:11
32     filename=horzcat( '/Users/liyangjiang/Documents/Phys 590 Pyrak
        -Nolte/B/Liyang/outputLccms05/measurementLccms05_source ',
        num2str(53+i) , '.dat ' );
33     A=load ( filename );M=M+A;
34 end
35 P90_JLY=M/11;clear M A;
36
37 M=zeros (60001,6);
38 for i = 1:1:11
39     filename=horzcat( '/Users/liyangjiang/Documents/Phys 590 Pyrak
        -Nolte/B/Liyang/outputLccms06/measurementLccms06_source ',
        num2str(53+i) , '.dat ' );
40     A=load ( filename );M=M+A;
41 end
42 S90_JLY=M/11;clear M A;
43
44 M=zeros (60001,6);
45 for i = 1:1:11
46     filename=horzcat( '/Users/liyangjiang/Documents/Phys 590 Pyrak
        -Nolte/B/Liyang/outputLccms07/measurementLccms07_source ',
        num2str(53+i) , '.dat ' );
47     A=load ( filename );M=M+A;
48 end
49 PN45_JLY=M/11;clear M A;
50
51 M=zeros (60001,6);
52 for i = 1:1:11

```

```

53     filename=horzcat(' /Users/liyangjiang/Documents/Phys 590 Pyrak
        -Nolte/B/Liyang/outputLccms08/measurementLccms08_source ',
        num2str(53+i), '.dat ');
54     A=load (filename);M=M+A;
55 end
56 SN45_JLY=M/11;clear M A;
57
58 M=zeros(60001,6);
59 for i = 1:1:11
60     filename=horzcat(' /Users/liyangjiang/Documents/Phys 590 Pyrak
        -Nolte/B/Liyang/outputLccms09/measurementLccms09_source ',
        num2str(53+i), '.dat ');
61     A=load (filename);M=M+A;
62 end
63 P15_JLY=M/11;clear M A;
64
65 M=zeros(60001,6);
66 for i = 1:1:11
67     filename=horzcat(' /Users/liyangjiang/Documents/Phys 590 Pyrak
        -Nolte/B/Liyang/outputLccms10/measurementLccms10_source ',
        num2str(53+i), '.dat ');
68     A=load (filename);M=M+A;
69 end
70 S15_JLY=M/11;clear M A;
71
72 M=zeros(60001,6);
73 for i = 1:1:11

```

```

74     filename=horzcat(' /Users/liyangjiang/Documents/Phys 590 Pyrak
        -Nolte/B/Liyang/outputLccms11/measurementLccms11_source ',
        num2str(53+i), '.dat ');
75     A=load (filename);M=M+A;
76 end
77 P30_JLY=M/11;clear M A;
78
79 M=zeros(60001,6);
80 for i = 1:1:11
81     filename=horzcat(' /Users/liyangjiang/Documents/Phys 590 Pyrak
        -Nolte/B/Liyang/outputLccms12/measurementLccms12_source ',
        num2str(53+i), '.dat ');
82     A=load (filename);M=M+A;
83 end
84 S30_JLY=M/11;clear M A;
85
86 M=zeros(60001,6);
87 for i = 1:1:11
88     filename=horzcat(' /Users/liyangjiang/Documents/Phys 590 Pyrak
        -Nolte/B/Liyang/outputLccms13/measurementLccms13_source ',
        num2str(53+i), '.dat ');
89     A=load (filename);M=M+A;
90 end
91 P60_JLY=M/11;clear M A;
92
93 M=zeros(60001,6);
94 for i = 1:1:11

```

```

95     filename=horzcat(' /Users/liyangjiang/Documents/Phys 590 Pyrak
        -Nolte/B/Liyang/outputLccms14/measurementLccms14_source ',
        num2str(53+i), '.dat ');
96     A=load (filename);M=M+A;
97 end
98 S60_JLY=M/11;clear M A;
99
100 M=zeros(60001,6);
101 for i = 1:1:11
102     filename=horzcat(' /Users/liyangjiang/Documents/Phys 590 Pyrak
        -Nolte/B/Liyang/outputLccms15/measurementLccms15_source ',
        num2str(53+i), '.dat ');
103     A=load (filename);M=M+A;
104 end
105 P75_JLY=M/11;clear M A;
106
107 M=zeros(60001,6);
108 for i = 1:1:11
109     filename=horzcat(' /Users/liyangjiang/Documents/Phys 590 Pyrak
        -Nolte/B/Liyang/outputLccms16/measurementLccms16_source ',
        num2str(53+i), '.dat ');
110     A=load (filename);M=M+A;
111 end
112 S75_JLY=M/11;clear M A;
113
114 M=zeros(60001,6);
115 for i = 1:1:11

```

```

116     filename=horzcat( '/Users/liyangjiang/Documents/Phys 590 Pyrak
        -Nolte/B/Liyang/outputLccms00P/measurementLccms00P_source '
        ,num2str(53+i) , '.dat' );
117     A=load ( filename );M=M+A;
118 end
119 IP=M/11;clear M A;
120
121 M=zeros(60001,6);
122 for i = 1:1:11
123     filename=horzcat( '/Users/liyangjiang/Documents/Phys 590 Pyrak
        -Nolte/B/Liyang/outputLccms00S/measurementLccms00S_source '
        ,num2str(53+i) , '.dat' );
124     A=load ( filename );M=M+A;
125 end
126 IS=M/11;clear M A;
127 %%%%%%%%%%%%%%%%%%%%%%%%%%%%%%%%%%%%%%%%%%%%%%%%%%%%%%%%%%%%%%%%%%%%%%%%%
128 %{
129 plot(1e6*P0_JLY(:,1),P0_JLY(:,3),'LineWidth',1.5);
130 hold on;
131 plot(1e6*P15_JLY(:,1),P15_JLY(:,3),'LineWidth',1.5);
132 plot(1e6*P30_JLY(:,1),P30_JLY(:,3),'LineWidth',1.5);
133 plot(1e6*P45_JLY(:,1),P45_JLY(:,3),'LineWidth',1.5);
134 plot(1e6*P60_JLY(:,1),P60_JLY(:,3),'LineWidth',1.5);
135 plot(1e6*P75_JLY(:,1),P75_JLY(:,3),'LineWidth',1.5);
136 plot(1e6*P90_JLY(:,1),P90_JLY(:,3),'LineWidth',1.5);
137 xlabel('Time (us)');
138 ylabel('\sigma_{zz} (P source)');
139 set(gca, 'fontweight','bold','FontSize',20);

```

```

140 legend('0\ circ ', '15\ circ ', '30\ circ ', '45\ circ ', '60\ circ ', '75\ circ
    ', '90\ circ ')
141 title('P to P Transmission ');
142 xlim([20.5 23]);
143 %}
144
145 %{
146 plot(1e6*P0_JLY(:,1),P0_JLY(:,4), 'LineWidth',1.5);
147 hold on;
148 plot(1e6*P15_JLY(:,1),P15_JLY(:,4), 'LineWidth',1.5);
149 plot(1e6*P30_JLY(:,1),P30_JLY(:,4), 'LineWidth',1.5);
150 plot(1e6*P45_JLY(:,1),P45_JLY(:,4), 'LineWidth',1.5);
151 plot(1e6*P60_JLY(:,1),P60_JLY(:,4), 'LineWidth',1.5);
152 plot(1e6*P75_JLY(:,1),P75_JLY(:,4), 'LineWidth',1.5);
153 plot(1e6*P90_JLY(:,1),P90_JLY(:,4), 'LineWidth',1.5);
154 xlabel('Time (us) ');
155 ylabel('\sigma_{zx} (P source) ');
156 set(gca, 'fontweight', 'bold', 'FontSize',20);
157 legend('0\ circ ', '15\ circ ', '30\ circ ', '45\ circ ', '60\ circ ', '75\ circ
    ', '90\ circ ')
158 title('P to S Transmission ');
159 xlim([29 36]);
160 %}
161
162 %{
163 plot(1e6*S0_JLY(:,1),S0_JLY(:,4), 'LineWidth',1.5);
164 hold on;
165 plot(1e6*S15_JLY(:,1),S15_JLY(:,4), 'LineWidth',1.5);
166 plot(1e6*S30_JLY(:,1),S30_JLY(:,4), 'LineWidth',1.5);

```



```

167 plot(1e6*S45_JLY(:,1),S45_JLY(:,4),'LineWidth',1.5);
168 plot(1e6*S60_JLY(:,1),S60_JLY(:,4),'LineWidth',1.5);
169 plot(1e6*S75_JLY(:,1),S75_JLY(:,4),'LineWidth',1.5);
170 plot(1e6*S90_JLY(:,1),S90_JLY(:,4),'LineWidth',1.5);
171 xlabel('Time (us)');
172 ylabel('\sigma_{zx} (S source)(arb. Units)');
173 set(gca,'fontweight','bold','FontSize',20);
174 legend('0\circ','15\circ','30\circ','45\circ','60\circ','75\circ
        ','90\circ')
175 title('S to S Transmission');
176 xlim([39 46]);
177 %}
178
179 %{
180 plot(1e6*S0_JLY(:,1),S0_JLY(:,3),'LineWidth',1.5);
181 hold on;
182 plot(1e6*S15_JLY(:,1),S15_JLY(:,3),'LineWidth',1.5);
183 plot(1e6*S30_JLY(:,1),S30_JLY(:,3),'LineWidth',1.5);
184 plot(1e6*S45_JLY(:,1),S45_JLY(:,3),'LineWidth',1.5);
185 plot(1e6*S60_JLY(:,1),S60_JLY(:,3),'LineWidth',1.5);
186 plot(1e6*S75_JLY(:,1),S75_JLY(:,3),'LineWidth',1.5);
187 plot(1e6*S90_JLY(:,1),S90_JLY(:,3),'LineWidth',1.5);
188 xlabel('Time (us)');
189 ylabel('\sigma_{zz} (S source)(arb. Units)');
190 set(gca,'fontweight','bold','FontSize',20);
191 legend('0\circ','15\circ','30\circ','45\circ','60\circ','75\circ
        ','90\circ')
192 title('S to P Transmission');
193 xlim([29 36]);

```

```

194 %}
195
196 %{
197 plot(1e6*P0_JLY(:,1),P0_JLY(:,4),'LineWidth',1.5);
198 hold on;
199 plot(1e6*P45_JLY(:,1),P45_JLY(:,4),'LineWidth',1.5);
200 plot(1e6*PN45_JLY(:,1),PN45_JLY(:,4),'LineWidth',1.5);
201 plot(1e6*P90_JLY(:,1),P90_JLY(:,4),'LineWidth',1.5);
202 xlabel('Time (us)');
203 ylabel('\sigma_{zx} (arb. Units)');
204 set(gca,'fontweight','bold','FontSize',20);
205 legend('0\circ','45\circ','-45\circ','90\circ')
206 title('P to S Transmission');
207 xlim([29 36]);
208
209 %}
210 ASVSV=zeros(1,7);
211 AASVSV=zeros(1,7);
212 for j=1:1:7
213 m=horzcat('S',num2str(15*(j-1)),'_JLY');
214 MM=eval(m);
215 M=MM(:,4);
216 ASVSV(j)=max(abs(M));
217 AASVSV(j)=max(M)-min(M);
218 end
219
220 APP=zeros(1,7);
221 AAPP=zeros(1,7);
222 for j=1:1:7

```

```

223 m=horzcat('P',num2str(15*(j-1)),'_JLY');
224 MM=eval(m);
225 M=MM(:,3);
226 APP(j)=max(abs(M));
227 AAPP(j)=max(M)-min(M);
228 end
229
230 APS=zeros(1,7);
231 AAPS=zeros(1,7);
232 for j=1:1:7
233 m=horzcat('P',num2str(15*(j-1)),'_JLY');
234 MM=eval(m);
235 M=MM(26000:33000,4);
236 APS(j)=max(abs(M));
237 AAPS(j)=max(M)-min(M);
238 end
239
240 ASP=zeros(1,7);
241 AASP=zeros(1,7);
242 for j=1:1:7
243 m=horzcat('S',num2str(15*(j-1)),'_JLY');
244 MM=eval(m);
245 M=MM(:,3);
246 ASP(j)=max(abs(M));
247 AASP(j)=max(M)-min(M);
248 end
249
250 AIP=max(abs(IP(:,3)));
251 AIS=max(abs(IS(:,4)));

```

```

252
253 %
254 plot(APP/AIP, '-ko', 'MarkerFaceColor', 'k', 'MarkerSize', 10, '
      LineWidth', 2); hold on;
255 plot(ASVSV/AIS, '-ro', 'MarkerFaceColor', 'r', 'MarkerSize', 10, '
      LineWidth', 2);
256 plot(APS/AIP, '-b^', 'MarkerSize', 10, 'LineWidth', 2);
257 plot(ASP/AIS, '-m^', 'MarkerSize', 10, 'LineWidth', 2);
258
259 set(gca, 'fontweight', 'bold', 'XTickLabel', [0 15 30 45 60 75 90],
      'FontSize', 16);
260 xlabel('degrees')
261 ylabel('Ratio of the absolute maximum');
262 title('Transmitted energy through the micro-cracks');
263 lgnd = legend('P-P Transmission (+\theta)', 'S-S Transmission (+\
      theta)', 'P-S Conversion (+\theta)', 'S-P Conversion (+\theta)')
      ;
264 set(lgnd, 'color', 'none');
265 legend boxoff;
266 ylim([0 0.8]);
267 %}

```

### A.15 Wavelet transformation of seismic waves

```

1 function [Integral, Phase]=wvlet(waveform, ti, tf, twi, twf, fmin, fmax
    , ntau, nfreq, Morletfact)
2 % [Integral, Phase]=wvlet(waveform, ti, tf, twi, twf, fmin, fmax, ntau,
    nfreq, Morletfact, i1)
3 %waveform is the original signal

```

```

4 %ti is the initial time of the signal (measured in sec)
5 % tf is the final time of the signal (measured in sec)
6 %twi use same values as ti
7 %twf use same values as tf
8 % fmin is the lowest frequency of the transform (in Hz)
9 % fmax is the highest frequency of the transform (in Hz)
10 % ntau is the number of time points in the transform
11 % nfreq is the number of frequency points in the transform
12 % Morletfact decides what kind of transform it will be:
13 % 0.5*sqrt(sqrt(2)/log(2)) is a traditional choice
14 % 1.0 is the minimal Morlet.
15 % 1/sqrt(2*pi)=0.3989 is the Nolte–Morlet
16 % 0.3 gives a good approximation to the 1–DOG and 2–DOG.
17 % Below approx. 0.3, the normalization falls off.
18 % 0.1 gives limiting 1–DOG and 2–DOG, but sub–unity normalization
    .
19 %delete the il
20 %to plot use pcolor(Integral); shading interp;
21 %%%%%%%%%%%%%%%%%%%%%%%%%%%%%%%%%%%%%%%%%%%%%%%%%%%%%%%%%%%%%%%%%%%%%%%%%%
22 wsize = size(waveform);%Get size of waveform matrix
23 count = wsize(2);%set to size of count
24 y = waveform(1,:);%redefine as variable y.
25 y=y(1:count)–y(1);%Subtract the first element.
26 %%%%%%%%%%%%%%%%%%%%%%%%%%%%%%%%%%%%%%%%%%%%%%%%%%%%%%%%%%%%%%%%%%%%%%%%%%
27 np=count; %The points collected in the sigal
28 np1=np–1; %Define a new counter.
29 dt=(tf–ti)/np1; %Sampling Rate
30 x=ti+(0:count–1)*dt; %Time axis of the signal
31 x=x(1:length(y));

```

```

32  %%%%%%%%%%%%%%%%%%%%%%%%%%%%%%%%%%%%%%%%%%%%%%%%%%%%%%%%%%%%%%%%%%%%%%%%%%
33  minx = min(x); % ti initial time of the signal in seconds
34  maxx = max(x); %tf Final time of the signal in seconds.
35  midx = (maxx-minx)/2.0;%Find the midpoints of the time.
36  delx = (twf-twi)/ntau; % time interval chosen for transformation
37  %%%%%%%%%%%%%%%%%%%%%%%%%%%%%%%%%%%%%%%%%%%%%%%%%%%%%%%%%%%%%%%%%%%%%%%%%%
38  freqmin=fmin;%Define minimum frequency in the transform.
39  freqmax=fmax;%Define the maximum frequency in the transform.
40  %%%%%%%%%%%%%%%%%%%%%%%%%%%%%%%%%%%%%%%%%%%%%%%%%%%%%%%%%%%%%%%%%%%%%%%%%%
41  ralpmin = freqmin/Morletfact;
42  ralpmax = freqmax/Morletfact;
43  delralp = (ralpmax-ralpmin)/nfreq;
44  %%%%%%%%%%%%%%%%%%%%%%%%%%%%%%%%%%%%%%%%%%%%%%%%%%%%%%%%%%%%%%%%%%%%%%%%%%
45  %Create empty matrices of the correct size.
46  IntR = zeros(ntau+1,nfreq+1);
47  IntI = zeros(ntau+1,nfreq+1);
48  Integral = zeros(ntau+1,nfreq+1);
49  Phase = zeros(ntau+1,nfreq+1);
50  freqcount = 0;%Start counter.
51  %%%%%%%%%%%%%%%%%%%%%%%%%%%%%%%%%%%%%%%%%%%%%%%%%%%%%%%%%%%%%%%%%%%%%%%%%%
52  for ralp = ralpmin:delralp:ralpmax;
53  %   disp(freqcount);
54      freqcount = freqcount + 1;%Advance counter.
55      freq(freqcount) = Morletfact*ralp;
56      %tmmm = Morletfact*ralp
57  %%%%%%%%%%%%%%%%%%%%%%%%%%%%%%%%%%%%%%%%%%%%%%%%%%%%%%%%%%%%%%%%%%%%%%%%%%
58  % Calculate wavelet for this alpha
59      ddx=(x(2)-x(1)); % here I think ddx equals to dt
60      nxhalf=fix((maxx-minx)/ddx)+1; % why +1?

```

```

61 x0=ddx*(-nxhalf:nxhalf);
62 DaughterR = morleta((x0).*ralp, Morletfact);
63 DaughterI = HILBERTA(DaughterR);
64 Daughter = sqrt(ralp)*(DaughterR - i*DaughterI);
65 %%%%%%%%%%%%%%%%%%%%%%%%%%%%%%%%%%%%%%%%%%%%%%%%%%%%%%%%%%%%%%%%%%%%%%%%%%
66 taucount = 0;%Set counter
67 for x0 = twi:delx:twf;
68     taucount = taucount + 1;%Advance counter.
69     tau(taucount) = x0;
70
71     ny=size(y,2);
72     ipos=round((taucount-1)*delx/ddx);
73     istart=-ipos+nxhalf+1; iend=-ipos+ny+nxhalf;
74     Product = Daughter(istart:iend).*y;
75     temp = (x(2)-x(1))*sum(Product);
76     Integral(taucount, freqcount) = abs(temp);
77     IntR(taucount, freqcount) = real(temp);
78     IntI(taucount, freqcount) = imag(temp);
79     Phase(taucount, freqcount) = real(temp);
80     %output = [freq(freqcount); x0; abs(temp); real(temp)];
81     %fprintf(fid, '%8.4e %8.4e %8.4e %8.4e\n', output);
82     %max_ampl=max(Integral);
83     %[mx,i]=max(Integral);
84     %[mx,v]=max(Integral);
85     %output2='2P-4P_wvlet_maxampl_B_AC1FRACMAY06_';
86     %outfilename=sprintf('%s%s%s%s%s%s', outputpath, '\', output2,
87         num2str(ind1), '00psi_rep3');
88     %eval(['save ', filename, '.freq max_ampl -ascii'])
89     %save(outfilename, 'max_ampl', '-ascii');

```

```

89     end
90 end
91 %%%%%%%%%%%%%%%%%%%%%%%%%%%%%%%%%%%%%%%%%%%%%%%%%%%%%%%%%%%%%%%%%%%%%%%%%%
92 function y = morleta(x,f);
93 % Usage: Morlet(x,f), where f is related to the number
94 % of oscillations under the gaussian.
95 % jpm
96 % f = 0.5*sqrt(sqrt(2)/ln(2)) is the traditional Morlet
97 % mpj
98 % f = 1 is the minimum Morlet.
99 % f = 1/sqrt(pi) = 0.5642 gives the Nolte-Morlet.
100 % f = 0.3 is close to the 1-DOG.
101
102 y = (pi^(-0.25))*exp(-x.^2/2).*sin(2*pi*f*x);
103
104 return;
105
106 function y = HILBERTA(f);          % f is a vector.
107 % Hilbert.m calculates the Hilbert transform of x
108 % by swaping the symmetric and asymmetric parts of the
109 % inverse Fourier transform that constructs the original function
110 % Usage: Hilbert(f), where f is a row vector, ideally a power of
111 % two long.
112 % Caution: Data must be evenly spaced, and must vanish outside of
113 % the data range.
114 % Orig. 11/2/96
115 D = size(f);

```



```

116 max = D(2);
117 ft = fft(f);
118 Hft = ft;
119 %Switch the symmetric and asymmetric parts
120 Hft(round(max/2):max) = -Hft(round(max/2):max);
121 temp = ifft(Hft);
122 x = 1:max;
123 %plot(x, real(temp), x, -imag(temp));
124 y = -imag(temp);
125 return

```

#### A.16 For Figures 6.17,6.18,6.19

```

1  %{
2  %LSVSV0=dlmread('/Users/liyangjiang/Documents/Phys 590 Pyrak-
    Nolte/data raw/20200609/MPS_NW_3.txt ');
3  %LSVSV0=dlmread('/Users/liyangjiang/Documents/Phys 590 Pyrak-
    Nolte/data raw/20200609/MPS_1000CST_3.txt ');
4  %LSVSV0=dlmread('/Users/liyangjiang/Documents/Phys 590 Pyrak-
    Nolte/data raw/20200728/1_MPSD_100K_200.txt ');
5  %LSVSV0=dlmread('/Users/liyangjiang/Documents/Phys 590 Pyrak-
    Nolte/data raw/20200504/MPS_WF_3.txt ');%water fill
6  LSVSV0=dlmread('/Users/liyangjiang/Documents/Phys 590 Pyrak-Nolte
    /data raw/20200901/MPS_300k_M__3200.txt ');
7
8
9  %LSVSV0=dlmread('/Users/liyangjiang/Documents/Phys 590 Pyrak-
    Nolte/data raw/20200601/MPS_100SCT_2.txt ');
10

```

```

11
12 %
13
14 [FIsvsv0 , PIsvsv0]=wvlet(LSVSV0(2000:3000)
    ',0.000030,0.00004,0.000030,0.00004,0,1500000,400,150,0.398);
15
16 pcolor(FIsvsv0 '); shading interp;
17
18
19
20 xlabel('time (us) ');
21 ylabel('Frequency (MHz) ');
22 set(gca, 'FontSize',16);
23 title('Wavelet Transform of P-S Converted Mode');
24 xticks([1 100 200 300 400]);
25 xticklabels({'30 ','32.5 ','35 ','37.5 ','40 '});
26 yticks([1 50 100 150]);
27 yticklabels({'0 ','0.5 ','1 ','1.5 '});
28
29
30 caxis manual
31 caxis([0 8*10-5]);
32 colorbar;
33 %}
34
35
36 %{
37
38

```

```

39 %LSVSV0=dlmread('/Users/liyangjiang/Documents/Phys 590 Pyrak-
    Nolte/data raw/20200609/MPP_1000CST_2.txt');
40 LSVSV0=dlmread('/Users/liyangjiang/Documents/Phys 590 Pyrak-Nolte
    /data raw/20200728/1_MPP_100K_2.txt');
41 %LSVSV0=dlmread('/Users/liyangjiang/Documents/Phys 590 Pyrak-
    Nolte/data raw/20200728/1_MPP_NW_2.txt');
42 %LSVSV0=dlmread('/Users/liyangjiang/Documents/Phys 590 Pyrak-
    Nolte/data raw/20200609/MPP_WF_2.txt');
43 %LSVSV0=dlmread('/Users/liyangjiang/Documents/Phys 590 Pyrak-
    Nolte/data raw/20200506/MPP_NW_2.txt');
44 %%%%%%%%%pp%%%%%%%%
45
46 [FIsvsv0, PIsvsv0]=wvlet(LSVSV0(1:3000)
    ',0.00000001,0.00004,0.00000001,0.00004,0,1500000,400,150,0.398)
    ;
47
48 pcolor(FIsvsv0'); shading interp;
49
50
51
52 xlabel('time (us)');
53 ylabel('Frequency (MHz)');
54 set(gca, 'FontSize',16);
55 title('Wavelet Transform of P-P Transmission');
56 xticks([1 100 200 300 400]);
57 xticklabels({'10','17.5','25','32.5','40'});
58 yticks([1 50 100 150]);
59 yticklabels({'0','0.5','1','1.5'});
60

```

```

61
62 caxis manual
63 caxis([0 80*10-5]);
64 colorbar;
65 %}
66
67 %
68 %LSVSV0=dlmread('/Users/liyangjiang/Documents/Phys 590 Pyrak-
        Nolte/data raw/20200603/MSS_1000CST_2.txt');
69 LSVSV0=dlmread('/Users/liyangjiang/Documents/Phys 590 Pyrak-Nolte
        /data raw/20200603/MSS_WF_2.txt');
70 %LSVSV0=dlmread('/Users/liyangjiang/Documents/Phys 590 Pyrak-
        Nolte/data raw/20200603/MSS_NW_2.txt');
71 %LSVSV0=dlmread('/Users/liyangjiang/Documents/Phys 590 Pyrak-
        Nolte/data raw/20200831/MSS_300k_2.txt');
72
73
74 [FIsvsv0 , PIsvsv0]=wvlet(LSVSV0(2000:5000)
        ',0.00003,0.00006,0.00003,0.00006,0,1500000,400,150,0.398);
75
76 pcolor(FIsvsv0'); shading interp;
77
78
79
80 xlabel('time (us)');
81 ylabel('Frequency (MHz)');
82 set(gca, 'FontSize',16);
83 title('Wavelet Transform of S-S Transmission');
84 xticks([1 100 200 300 400]);

```

```
85 xticklabels({'30 ','35 ','40 ','45 ','50 '});
86 yticks([1 50 100 150]);
87 yticklabels({'0 ','0.5 ','1 ','1.5 '});
88
89
90 caxis manual
91 caxis([0 20*10-5]);
92 colorbar;
93 %}
```

## VITA

Liyang Jiang was born in Yangzhou, Jiangsu Province, China in 1992. Went to high school in Nanjing and attended the Shanghai Jiaotong University in Shanghai, China. A bachelor degree majored in applied physics and minored in applied mathematics was received in 2014. Liyang came to USA in 2014 to attend Purdue University's PhD program in the department of Physics and Astronomy, where she joined Professor Pyrak-Nolte's group in 2016 and worked together with Prof. Bobet from civil engineering department.